Theoretical Design of Photonic Crystal Devices for Integrated Optical Circuits

by

Attila Mekis

Submitted to the Department of Physics
in partial fulfillment of the requirements for the degree of

Ph.D. in Physics

at the

MASSACHUSETTS INSTITUTE OF TECHNOLOGY

February 2000

Author .....
Department of Physics
November 30, 1999

Certified by .....
John D. Joannopoulos
Francis Wright Davis Professor of Physics
Thesis Supervisor

Accepted by .....
Thomas J. Greytak
Associate Department Head for Education

Theoretical Design of Photonic Crystal Devices for Integrated Optical Circuits

by

Attila Mekis

Submitted to the Department of Physics
on November 30, 1999, in partial fulfillment of the
requirements for the degree of
Ph.D. in Physics

Abstract

In this thesis we investigate novel photonic crystal devices that can be used as building blocks of all-optical circuits. We contrast the behavior of light in photonic crystal systems and in their traditional counterparts. We exhibit that bends in photonic crystals are able to transmit light with over 90% efficiency for large bandwidths and with 100% efficiency for specific frequencies. In contrast to traditional waveguides, bound states in photonic crystal waveguides can also exist in constrictions and above the cutoff frequency. We discuss how to lower reflections encountered when photonic crystal waveguides are terminated, both in an experimental setup as well as in numerical simulations. We show that light can be very efficiently coupled into and out of photonic crystal waveguides using tapered dielectric waveguides. In time-domain simulations of photonic crystal waveguides, spurious reflections from cell edges can be eliminated by terminating the waveguide with a Bragg reflector waveguide. We demonstrate novel lasing action in two-dimensional photonic crystal slabs with gain media, where lasing occurs at saddle points in the band structure, in contrast to one-dimensional photonic crystals. We also design a photonic crystal slab with organic gain media that has a TE-like pseudogap. We demonstrate that such a slab can support a high-Q defect mode, enabling low threshold lasing, and we discuss how the quality factor depends on the design parameters. We also propose to use two-dimensional photonic crystal slabs as directionally efficient free-space couplers. We draft methods to calculate the coupling constant both numerically and analytically, using a finite-difference time-domain method and the volume current method with a Green's function approach, respectively.

Thesis Supervisor: John D. Joannopoulos
Title: Francis Wright Davis Professor of Physics

Acknowledgments

There is a host of people who have given me their time and advice without which this thesis would not have been written. John Joannopoulos, my thesis advisor and mentor has inspired me to have my sight on the clouds and my feet on the ground. He has always been accesible and supplied me with invaluable advice. I thank him for his help in all matters academic and personal.

Among the many people I owe so much at MIT are the members of the 'gang'. Shanhui Fan has been a great support and friend all throughout my Ph.D. candidate years. He has read countless drafts for me and has always put my scribbles on the top of his to-do pile. I thank him for his insights that he shared with me every time I spoke with him. It has been a pleasure to work with Pierre Villeneuve as well whose ready advice and humor have helped me to go forward in my projects. I am also grateful to Steven Johnson who have given me help whenever I needed advice on a computational question, computer problems or photonic crystal issues. Many thanks to Jerry Chen and Ilya Kurland who have helped me start on my first project at MIT, which has become the first chapter of my thesis.

In my electronic band structure period, Kyeongjae Cho has given me a lot of his time and helped me learn to use the band structure code. I give my thanks to David Landau at the University of Georgia as well who was a great host and teacher during the week I spent in Athens. Ickjin Park and Tairan Wang helped me out in times of computer trouble. The same holds for Nikolaj Moll, who has also been an excellent office mate – a very important ingredient to work efficiently.

I extend my gratitude to all the people I have worked with at Bell Labs. Many thanks to Cherry Murray and Richart Slusher who made it possible for me through many difficulties to spend two summers and an IAP at Murray Hill. Ananth Dodabalapur was my mentor at Bell, and has taught me what I know about working in an industrial setting. Vielen Dank to Martin Meier who has spent many evenings fabricating structures and taking measurements, some of which are presented in this thesis. I thank both Ananth and Martin for their companionship and good humor. I

am also grateful members of the fabrication team who helped make my designs come true, among others, John Rogers, Allan Timko and Om Nalamasu. Many thanks to the Smith family in North Plainfield who have put me up and supported me during my stay at Bell, and always made it fun to return back at the end of the day.

Of course none of this would have been even remotely possible had it not been for the other two most important persons in my life. One is Ruth, my beloved wife, who has stood by me through all the difficulties. She has been my inspiration to reach for the stars and she should be acknowledged as a 'co-author' for all her help. Finally, I thank God for revealing Himself to me in my first year at MIT. He has led me through the highest peaks of discovery and inspiration and have been with me through the dark valleys of obstacles and desperation. I give all my thanks to Him for giving me understanding of His amazing Creation.

This work was supported in part by the MRSEC Program of the NSF under Award No. DMR-9400334.

Contents

List of Figures

Chapter 1

Introduction

Electromagnetic waves are becoming the dominant means of transmission in long-distance communications. Due to the larger bandwidth of photons in dielectric materials compared to electrons in metals, information can be sent using light at a much faster rate than it can be done relying on electricity. For this reason, light transmission is expected to dominate all future communications. Presently thousands of miles of optical fibers are being laid down to complete an infrastructure of transmitting and routing wavepackets of light containing large amounts of information. However, integrated circuits that process this information are mostly electronic or hybrid optoelectronic in nature. Even though all-optical circuits could interface naturally with optical fibers, they are not yet available commercially. The challenge is to design efficient, fast, reliable components for such circuits that can be integrated on a small scale. Since the demand for large-scale integration has spawned an industry with well-established nanoscale fabrication methods, all-optical circuits can be fabricated with ease.

Photonic crystals offer novel ways of making integrated optical circuit components. They are materials whose dielectric constant is periodic in space. If the parameters of the photonic crystal are properly chosen, we can create a frequency range where electromagnetic wave propagation is forbidden. Photonic band gap (PBG) materials are extremely useful when designing dielectric devices to manipulate photons. In this thesis we investigate the physics of photonic crystal systems — fundamentally

different from their traditional counterparts — that can become building blocks of all-optical circuits. We utilize the flexibility and control PBG materials enable us with to design devices for use in opto-electronic or all-optical integrated circuits. Some important circuit components under consideration include waveguides, waveguide bends and couplers, free-space couplers and lasers.

In this work we also model and numerically simulate photonic crystal devices. We demonstrate analytial arguments by computationally implementing certain systems to exhibit the novel properties of photonic crystals. We endeavor to design components that are amenable for fabrication in the submicron range with currently available nanofabrication technology. Through a combination of novel theoretical concepts and numerical calculations, we propose optimal designs for optical circuit components based on photonic crystals.

In Chapter 2, we demonstrate highly efficient transmission of light around sharp corners in photonic bandgap waveguides. Numerical simulations reveal *complete* transmission at certain frequencies, and very high transmission (>95%) over wide frequency ranges. High transmission is observed even for 90° bends with zero radius of curvature, with a maximum transmission of 98% as opposed to 30% for analogous conventional dielectric waveguides. We propose a simple one-dimensional scattering theory model with a dynamic frequency-dependent well-depth to describe the transmission properties.

In Chapter 3, we investigate the mechanism for the appearance of bound states in two-dimensional photonic crystal waveguides and contrast it with the corresponding mechanism for conventional guides. It is shown that the periodicity of the photonic crystal can give rise to frequency ranges above cutoff where no guided modes exist in the waveguides. Such mode gaps make possible the creation of bound states in constrictions and in bends. Bound states are found to correspond to analogous cavity modes and it is shown that their appearance strongly depends on the lattice geometry and cannot be described in a one-dimensional framework.

In Chapter 4, we design tapered waveguide junctions for coupling between photonic crystal and traditional dielectric waveguides and evaluate their transmission

efficiency. While the transmission efficiency is only between 20-55% using no taper, the tapered couplers we present have over 90% power transmission. We discuss tapers and inverse tapers for coupling into and out of photonic crystal waveguides.

In Chapter 5, we present a novel numerical scheme for the reduction of spurious reflections in simulations of electromagnetic wave propagation in photonic crystal waveguides. We use a distributed Bragg reflector waveguide termination to reduce reflection from photonic crystal waveguide ends by improving k-matching for photonic crystal waveguided modes. We describe computational procedures and exhibit that a significant reduction in reflection amplitude can be achieved across a large part of the guided mode spectrum. This method enables one to reduce simply and effectively the computational requirements in photonic crystal waveguide simulations.

In Chapter 6, we report an analysis of the operation of a new type of laser resonator with two-dimensional distributed feedback from a photonic crystal. The gain medium consists of an organic host doped with dyes and is deposited on lithographically patterned Si/SiO_2 structures. Bragg reflections caused by the grating diminish the group velocity of photons along some directions of crystallographic symmetry to zero, and the resulting feedback gives rise to laser oscillations. Dispersion relations for photons were calculated analytically and are used to interpret the laser emission spectra.

In Chapter 7, we conduct a comprehensive investigation of the lasing mechanism in a photonic crystal slab laser with a refractive index that is periodic in two dimensions. Experimental spectra of laser structures fabricated with organic gain media are presented. It is found that lasing frequencies can be explained in terms of Van Hove singularities in the density of modes. We also observe lasing spectra that cannot be obtained from structures with one-dimensional periodicity, such as traditional distributed feedback lasers. Lasing frequencies are computed using numerical techniques.

In Chapter 8, we use organic gain media to fabricate a laser based on a defect mode in a photonic crystal slab. We design a photonic crystal slab with an in-plane pseudogap for TE-like modes that can support a defect mode with a Q estimated to

be about 376. The effects of the design parameters on the gap size and the defect quality factor are investigated. The mechanism for energy loss from the lasing mode and details of the computation of the defect quality factor are also discussed.

In Chapter 9, we propose the use of two-dimensional photonic crystal slabs to improve the directionality of output coupling from planar waveguides and distributed feedback lasers. We present a theory underlying the operation of such structures and design criteria for emission in desired directions. As an example, we demonstrate a vertical coupler integrated with an organic distributed feedback laser, use computer simulations to find its coupling constant and efficiency and then discuss its feasibility.

In Chapter 10, we calculate in a perturbation approach the coupling constants for in-plane and out-of-plane coupling of guided modes due to a two-dimensionally periodic refractive index variation in a dielectric slab. We rely on the volume current method and employ the far-field form of the slab Green's functions to obtain expressions for the constants. Finally, we discuss extending the Green's function approach to calculate transmission through an arbitrary photonic crystal slab.

Chapter 2

High transmission through sharp bends in photonic crystal waveguides

2.1 Introduction

Photonic crystals have inspired great interest recently because of their potential ability to control the propagation of light. They can modify and even eliminate the density of electromagnetic states inside the crystal [1, 2]. Such periodic dielectric structures with complete band gaps can find many applications, including the fabrication of lossless dielectric mirrors and resonant cavities for optical light [3]. In this chapter, we demonstrate a novel method for guiding light around sharp corners, using photonic crystal waveguides.

Two main designs are commonly employed to guide electromagnetic waves along a line: metallic pipe waveguides which provide lossless transmission only for microwaves, and dielectric guides for infrared and visible light. Although metallic waveguides can be used to steer light around tight corners, the operation of conventional dielectric guides, based on the principle of total internal reflection, is restricted by radiation losses to moderate curvature bends. In fact, when light is steered around

a corner in such a guide, the radius of curvature must well exceed the wavelength of the light even for high dielectric contrasts to avoid large losses at the corners [4]. In a recent article, Meade *et al.* showed that a linear defect in a photonic bandgap (PBG) material can support a linearly localized mode when the mode frequency falls inside the gap [5]. Such a defect can act as a waveguide for EM waves, without relying on total internal reflection. In this letter we further show that a PBG waveguide can efficiently guide light around corners. The losses are very low for a wide range of frequencies, and vanish for specific frequencies, even if the radius of curvature of the bend is on the order of one wavelength.

2.2 Results of numerical simulations

For simplicity, we select to study a 2D photonic crystal of dielectric rods in air on a square array with lattice constant a. Choosing the refractive index of the rods to be 3.4 (which corresponds to GaAs at the canonical wavelength of $1.55\,\mu$m) and their radius to be $0.18a$, we find that the crystal has a TM[1] gap which extends from frequency $\omega = 0.302\ 2\pi c/a$ to $\omega = 0.443\ 2\pi c/a$. One can create a single non-degenerate guided TM mode inside the gap by removing a row of rods. Since the waveguide has translational symmetry, a mode can be characterized by its reciprocal space wavevector k along the direction of the guide. The band appears at a frequency $\omega = 0.312\ 2\pi c/a$ when $k = 0$ and reaches the top of the gap when $k = 0.38\ 2\pi/a$. Since the characteristics of a PBG material remain unchanged under rescaling, we can easily assure that the guided light will be in the infrared or visible region. For example, if we choose a lattice constant a of $0.58\,\mu$m, the wavelength corresponding to the midgap frequency will be $1.55\,\mu$m.

If a bend is introduced into such a waveguide, no power will be radiated out of the guide as light travels around the bend, since there are no extended modes into which the propagating mode can couple. Light will either be transmitted or reflected;

[1]TM modes are defined as the modes for which the magnetic field is transverse to the normal direction of the plane of translational symmetry; or equally, TM modes are the modes for which the electric field is parallel to the axis of the dielectric columns.

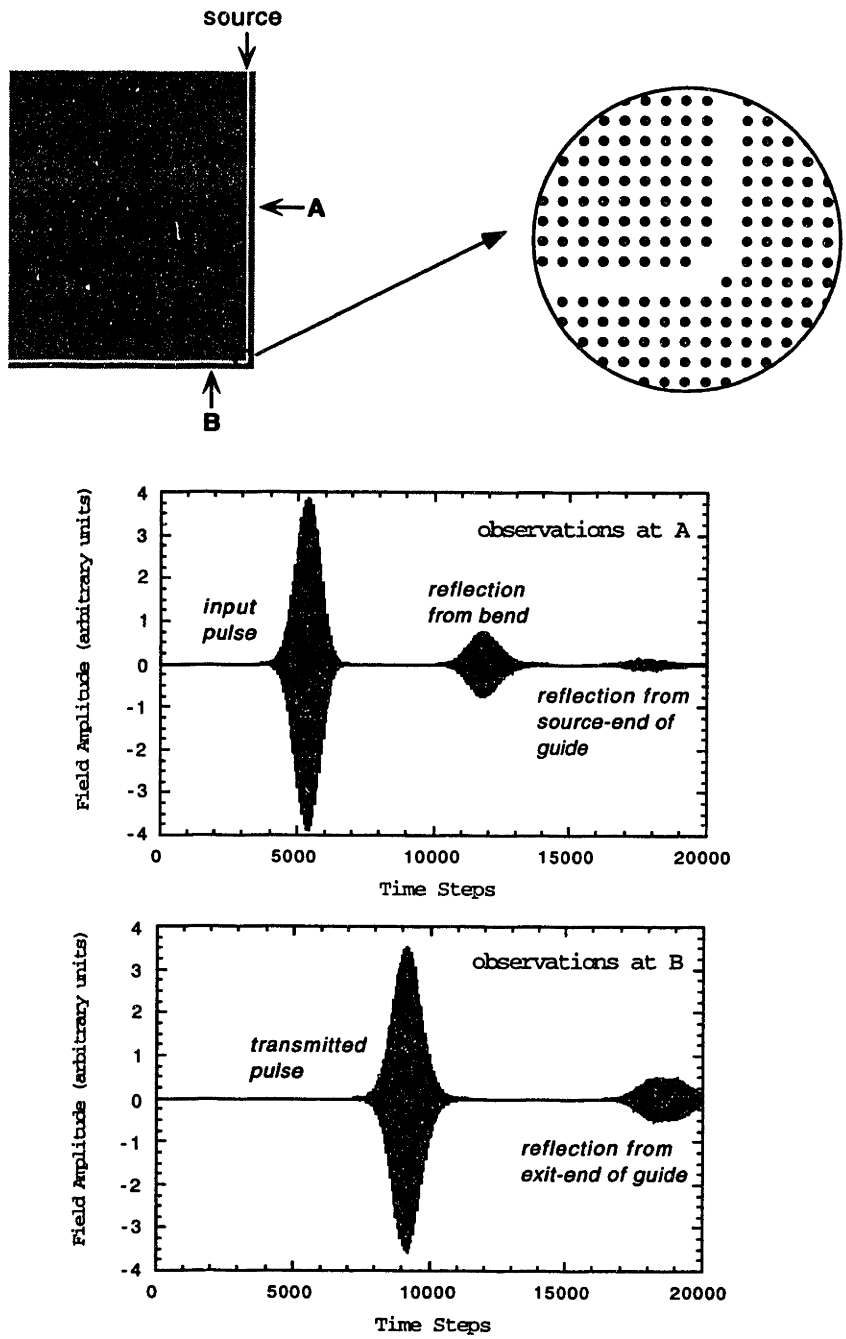

Figure 2-1: Top Panel: Schematic view of the $100a$ x $120a$ computational cell. The field amplitude is monitored at points A and B. The guide is located five lattice constants from the edge of the cell. Bottom Panel: Field amplitude recorded at points A and B, as a function of time. The pulses reflected by and transmitted through the bend, as well as the pulses reflected from the edges of the cell, are easily discernible.

only back reflection will hinder perfect transmission. We study the transmission and reflection properties of waveguide bends using a vector finite-difference time-domain program with quartic perfectly matched layer boundaries [6]. In our simulation, a dipole located at the entrance of the waveguide creates a pulse with a Gaussian envelope in time. The field amplitude is monitored inside the guide at two points, one before the bend (point A) and one after (point B) as indicated in the top panel of Fig.2-1. Although most of the light that reaches the edge of the computational cell is absorbed by the boundaries, some light gets reflected back from the ends of the waveguide. By using a sizable computational cell of 100 x 120 lattice constants and by positioning each monitor point appropriately, we can distinguish and separate all the different pulses propagating in the cell; the useful pulses, such as the input pulse and the pulses reflected by and transmitted through the bend, and the parasite pulses which are reflected from the edges of the cell. These pulses are clearly shown in the bottom panel of Fig.2-1.

In the specific case shown in Fig.2-1, six pulses are sent down the guide, covering different ranges of frequencies. It would be possible, in principle, to use only one pulse with a spectrum covering the entire gap to determine the transmission properties of the bend. However, the spatial width of such a pulse — initially small — would increase rapidly in time, resulting in an overlap between the useful and parasite pulses propagating in the computational cell. The pulses measured at points A and B are Fourier transformed to obtain the reflection and the transmission coefficients for each frequency. The results are shown in the two panels on the top of Fig.2-2. The excellent agreement between the transmission and reflection coefficients obtained from the different pulses demonstrates the consistency of our approach. The transmission and reflection coefficients do add up to unity for every frequency in the gap, which confirms that there is no observable radiation loss, in spite of the close proximity of the waveguide to the edge of the computational cell. It is somewhat difficult to determine the reflection and transmission coefficients near the cutoff frequency $\omega = 0.312\ 2\pi c/a$. At these frequencies, the pulse comprises long-wavelength components and spreads out as it propagates inside the guide. This widening results in overlaps among the

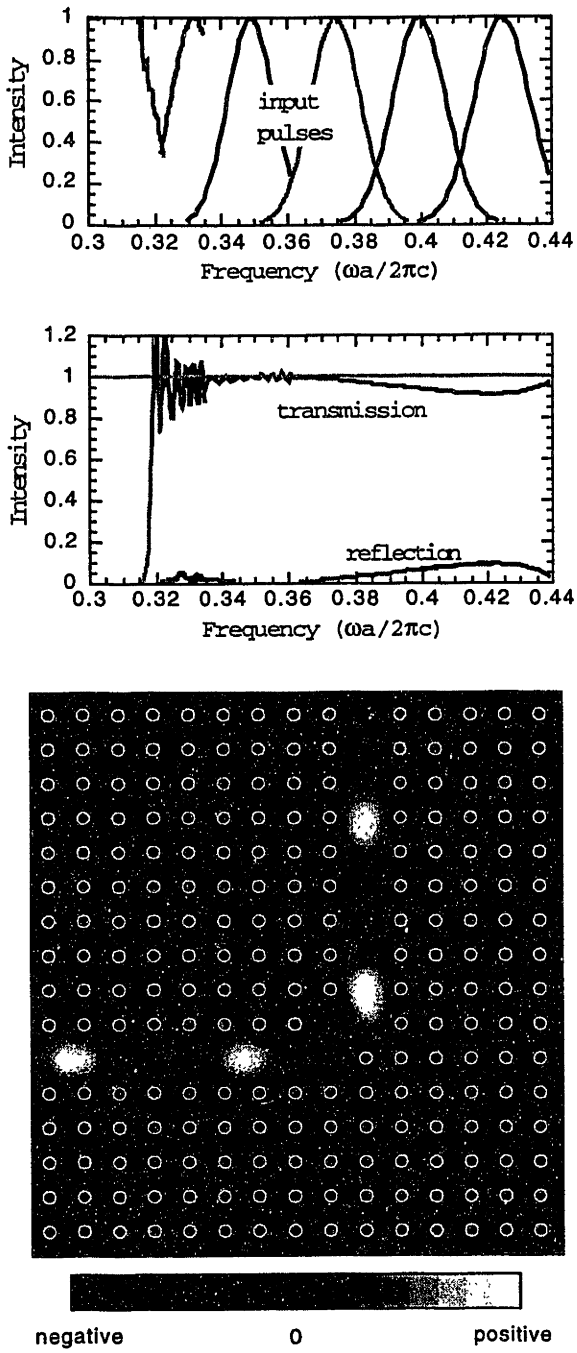

Figure 2-2: Top Panel: Spectral profile of six input pulses. Center Panel: Computed transmission and reflection coefficients for each input pulse. The fast oscillations in transmission at low frequencies are unphysical. Bottom Panel: Electric field pattern in the vicinity of the bend for frequency $\omega = 0.353\ 2\pi c/a$. The electric field is polarized along the axis of the dielectric columns. White circles indicate the dielectric posts.

useful and the parasite pulses. The separation of the overlapping pulses introduces Gibbs oscillations.

The transmission drops sharply to zero below the cutoff frequency of the guided mode. The transmission for frequencies $\omega < 0.392\ 2\pi c/a$ is larger than 95%, and reaches 100% when $\omega = 0.353\ 2\pi c/a$. The field pattern of the propagating mode can be observed by a CW excitation of the guided mode. We show in the bottom panel of Fig.2-2 the electric field pattern for the case where $\omega = 0.353\ 2\pi c/a$. The mode is completely confined inside the guide, and the light wave travels smoothly around the sharp bend, even though the radius of curvature of the bend is on the order of the wavelength of the light. For comparison purposes, we have calculated the transmission through a traditional rib dielectric waveguide of refractive index 3.5 with a similar radius of curvature. The radius of curvature R was taken to be equal to the width of the guide and the transmission was measured for a wide range of frequencies centered around $\omega = 0.143\ 2\pi c/R$. The power transmission was found not to exceed 80%.

2.3 Theoretical analysis of reflection spectra

We now propose a simple model to explain both the high transmission through the bends and the oscillatory behavior of the transmission spectrum. Our PBG waveguide structure can be viewed as separate waveguide sections, one in the (01) direction and one in the (10) direction, connected by a short waveguide section in the (11) direction. For any given frequency ω, there is a single wavevector $k(\omega)$ for the guided modes in any particular waveguide section. We label these wavevectors $k_1(\omega)$ for propagation along the (01) or (10) direction, and $k_2(\omega)$ for the (11) direction. These wavevectors are given by the dispersion relations shown in Fig.2-3. The dispersion relations are determined using a frequency-domain band-structure computation code [7]. From this figure, we can define a frequency-dependent effective refractive index $n(\omega) = c\,k(\omega)/\omega$ governing the wave propagation in each of the waveguide sections.

We model the transmission through the bend as a simple one-dimensional scat-

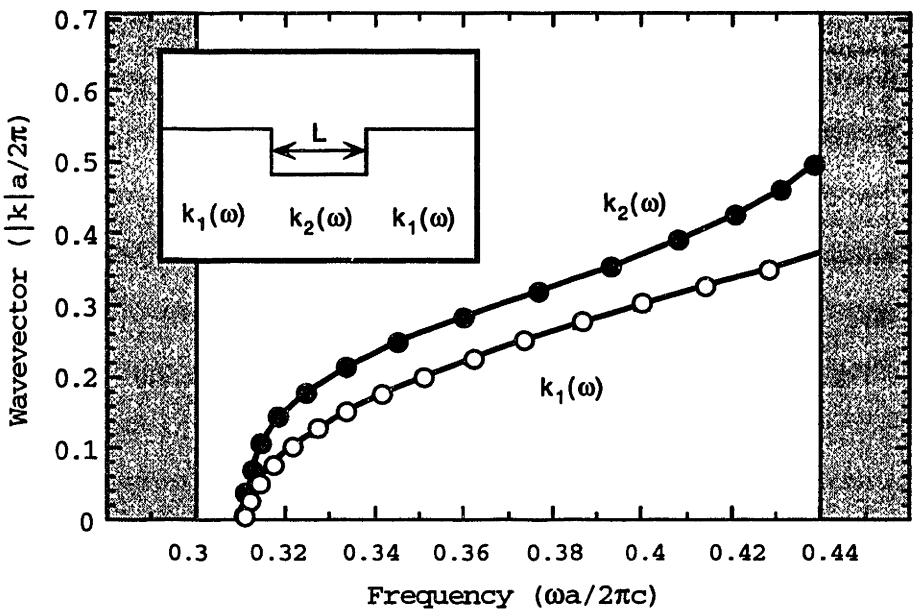

Figure 2-3: Dispersion relation $k_1(\omega)$ for propagation along the (01) or (10) direction, and $k_2(\omega)$ for the (11) direction. The gray regions correspond to the edges of the bandgap. The "potential" associated with the bend is shown in the inset.

tering process in which the mode propagating with wavevector k_1 is scattered into the mode with wavevector k_2, then back into the mode with wavevector k_1. At the interface, we require continuity of the field and of its derivative, as we would in the case of a plane EM wave normally incident on a boundary between materials with different refractive indices. By complete analogy with the one-dimensional Schrödinger equation, we can map this problem onto that of a wave propagating in a "dielectric potential". This potential consists of three constant pieces, corresponding to the (01), (11), and (10) propagation directions, respectively, as shown in the inset of Fig.2-3. Our model differs from the usual one-dimensional scattering problem in that the depth of the well, determined by the difference $k_1^2(\omega) - k_2^2(\omega)$, now depends on the frequency of the travelling wave.

The reflection coefficient is then given by

$$R(\omega) = \left[1 + \left(\frac{2\,k_1(\omega)\,k_2(\omega)}{[k_1^2(\omega) - k_2^2(\omega)]\sin[k_2(\omega)L]}\right)^2\right]^{-1}. \qquad (2.1)$$

The sole parameter in equation (2.1) is the length L of the well (or of the bend). To set this parameter, we select a single point from the computational results shown in Fig.2-2. We choose the point at $\omega = 0.353\ 2\pi c/a$, where the reflection coefficient is zero. Our choice of solution is $L = 1.33\sqrt{2}a$, which is the one closest to the physical length of the (11) portion of the waveguide.

To test the validity of this model, we vary the length of the (11) waveguide section and compare the reflection coefficients computed from the numerical simulations to those obtained from equation (2.1). The value $L = 1.33\sqrt{2}a$ found above is used to set the parameter L in each case. As we vary the bend length by integer multiples of $\sqrt{2}a$, the effective length L should also change by the same amount, giving $L = 0.33\sqrt{2}a$, $1.33\sqrt{2}a$, $2.33\sqrt{2}a$ and $3.33\sqrt{2}a$ for the four bends shown in Fig.2-4. The reflection coefficients are plotted in Fig.2-4. We find good agreement between the one-dimensional scattering model (solid line) and the numerical simulations (diamonds). Our model correctly predicts the frequencies where the reflection coefficient vanishes, as well as the general quantitative features of the transmission spectrum.

We note that the 90° bend with zero radius of curvature, as shown in the top panel of Fig.2-4, is not described in this model by a uniformly constant potential, but by the potential shown in the inset of Fig.2-3 with an effective length $L = 0.33\sqrt{2}a$. This length is extrapolated from the bends with longer (11) sections. Our model accurately predicts the existence of reflection from the bend, with transmission exceeding 95% for guided modes below $\omega = 0.403\ 2\pi c/a$. This behavior is in marked contrast to that of a conventional dielectric waveguide with a sharp 90° bend. Power transmission reaches at most 30% even for a guide with a refractive index contrast of 3.5 to 1 with its surroundings, due to large radiation losses at the corner.

The one-dimensional scattering analysis presented above relies on the existence of a band gap along every direction in the plane of the 2D crystal. Therefore, our analysis should also hold for 3D photonic crystals with complete omnidirectional band gaps. By adjusting the length of the bend section, we should be able to achieve 100% transmission through sharp bends for several frequencies. Furthermore, transmission should remain high as long as the dispersion relations in the two different waveguides

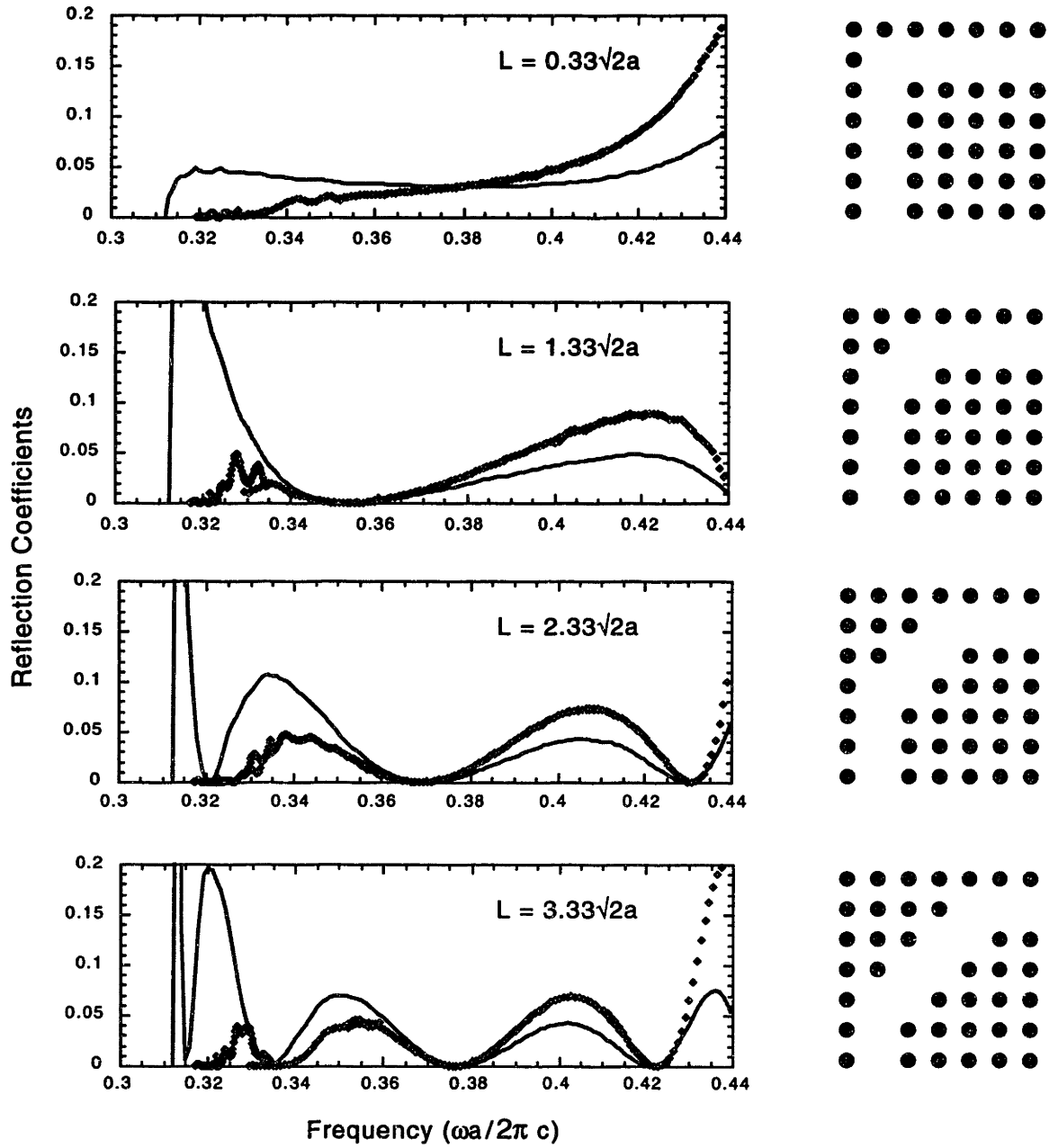

Figure 2-4: Reflection coefficients computed from numerical simulations (diamonds) and from one-dimensional scattering theory (solid line), for four different bend geometries.

making up the bend do not differ considerably, that is, as long as the depth of the "dielectric potential well" remains small.

Finally, a natural question to pose about these photonic crystal waveguides concerns the possible existence of bound states localized in the vicinity of the corner. These bound states are known to exist in other similar structures such as quantum wires [8, 9]. In the case of photonic crystals, bound states may appear in a frequency range where guided modes exist inside the bend section while being forbidden in the other sections of the guide. Although this particular condition does not hold in the waveguide structures investigated above, it is possible to alter the waveguide geometry in order to change the dispersion relations, thereby creating a configuration which would support bound states.

Chapter 3

Bound states in photonic crystal waveguides and waveguide bends

3.1 Introduction

Bound states in waveguides, and especially in waveguide bends, have recently been the subject of widespread theoretical and experimental investigation. Jaffe and Goldstone proved [8] that bends, which behave like local bulges in the guide, always support bound states in constant cross-section quantum waveguides under the condition that the wavefunction vanishes on the boundary. Papers by Carini *et al.* [10, 11, 12] deal with calculating energies of single and multiple bound states in bent quantum waveguides and comparing them to results from microwave experiments. Much effort has also been spent on finding new and calculationally efficient approaches for determining bound state energies in waveguide bends [13, 9]. Such research was ultimately prompted by an interest in semiconductor device minituarization. Since electronic transport properties through such quantum wires are influenced by the existence of localized states [14, 15], having a good understanding of bound states in bends is relevant to building small scale integrated circuits.

There is also considerable current interest in designing integrated optoelectronic or all-optical circuits. A set of essential components in these circuits are electromagnetic waveguides. Traditionally, two main types of guides are used in controlling the

linear propagation of EM waves: metallic guides for microwaves and dielectric guides for optical light. In two-dimensional structures, planar symmetry implies that the waveguide modes can have either TM or TE polarizations.[1] One can then reformulate the problem for metallic waveguides in terms of a single scalar field. On the boundary the field amplitude is zero for TM modes and the field derivative vanishes for TE modes. The results of [8] thus carry over to electromagnetic waves with TM polarization in 2-D metallic waveguides as well: any bulge or bend will generate a bound state. We note that in the case of a dielectric waveguide with a high dielectric contrast, the fields are similar to that of a metallic guide, so we expect that bulges and bends in these waveguides will also generate localized states in a similar manner. However, since these states can couple to free space modes, they will be decaying resonances and not bound states.

As an alternative to conventional (metallic or dielectric) components, photonic band gap (PBG) materials are well suited as building blocks of devices comprising all-optical circuits [16, 17, 18, 5, 19]. PBG waveguides—linear defects in PBG materials—are capable of guiding light at optical wavelengths without appreciable losses [5]. Furthermore, it has also been demonstrated that such guides can transmit EM waves efficiently through sharp corners [19]. The question of whether bound states exist in PBG waveguide bends arises naturally. In this paper, we study the conditions and the mechanism for the appearance of bound states in such guides. For simplicity, we consider only two-dimensional photonic crystals. However, the analysis presented here applies also to three-dimensional crystals. We present general arguments on PBG waveguide band structures, mode gaps and bound states and illustrate the arguments with specific examples. We find that PBG waveguides, unlike conventional ones, can possess mode gaps. These gaps make it possible for bound states to exist in bends and in constrictions even above the cutoff frequency for guided modes. It is also shown that the appearance of bound states in bends cannot be described in a purely one-dimensional framework and that these states are closely related to cavity modes.

[1]Here TM modes are defined so that the magnetic field lies in the 2-D plane, with the electric field normal to the plane.

The outline of the paper is as follows. In Sec.2, the methods of calculation are presented, and in Sec.3 PBG waveguides are studied. In Sec.4, we investigate bound states in photonic crystal waveguides both in straight and bent waveguides.

3.2 Methods of calculation

The dispersion relations for the PBG waveguides in this paper are calculated by solving Maxwell's equations in the frequency domain for given dielectric configurations [7]. A supercell with periodic boundary conditions is taken as the computational domain. The length of the cell corresponds to the periodicity of the dielectric in the direction of the guide, whereas the width was taken to be several (usually twelve) lattice constants. The photonic crystal simulated in this way contains parallel, evenly spaced waveguides. We increased the distance between the guides by taking wider and wider unit cells until the frequencies obtained for the eigenmodes no longer depended on the cell size. In this way we ensure that the distance between the guides is sufficient so that modes localized in the guides do not appreciably couple to each other through the bulk. Therefore we obtain the correct frequencies for the localized modes associated with an individual waveguide at each wavevector.

The bound states in various PBG waveguide configurations are studied by solving Maxwell's equations in the time domain. The computational domain used is rectangular, and is bounded by a perfectly matching layer material [20] to minimize back reflections. Modes with a wide range of frequencies are excited by a dipole source with a Gaussian temporal profile. The modes that remain after transient ones decay are either bound states or slowly decaying resonances; they both show up as peaks on the time Fourier transform of the field measured inside the waveguide. The resonances can easily be distinguished from bound states by noting that bound states have an essentially infinite quality factor when a large enough supercell is used. Also, in waveguide configurations, resonances occur at frequencies corresponding to zero group velocity in the waveguide or in the frequency range corresponding to guided modes, whereas bound states exist inside the mode gaps. The frequencies of all the

bound states can be identified by using a pulse short in time. Each bound state can be studied individually by using a long excitation pulse whose Fourier spectrum is peaked at the bound state frequency. The electric field configurations shown in this chapter are snapshots taken after a long time once every transient mode has decayed, leaving only a single mode.

3.3 Guided modes in photonic crystal waveguides

Just as the regular arrangement of atoms in a crystal gives rise to band gaps, the periodicity of the spatial dielectric distribution in a photonic crystal may prevent electromagnetic waves of certain frequencies from propagating inside the bulk. Because of the periodicity, the modes of the electromagnetic waves in the crystal can be expanded in Bloch functions defined by their wavevectors $\mathbf{k}$. While in the photonic band gap there are no solutions to Maxwell's equations for an infinite crystal for any real $\mathbf{k}$, one does obtain solutions with complex $\mathbf{k}$'s. These solutions will only become physical if the periodicity of the crystal is broken by introducing a defect.

We consider a square array of parallel, infinitely long high dielectric rods in air. The removal of a row of rods breaks the periodicity in one spatial direction. If the parameters of the crystal are such that there is a complete band gap for wavevectors perpendicular to the rods, then this defect can introduce modes that decay exponentially away from the defect but can still be described by a wavevector pointing along the missing row of rods. Such a defect acts like a waveguide: waves of the right frequencies can propagate down the guide [3].

For definiteness, we assume GaAs rods of circular cross-section, with an index of refraction of 3.4, appropriate at optical wavelengths. From now on, we restrict our analysis to TM modes. A large TM band gap (38%) occurs when the rods have a radius $r = 0.18a$, where a is the distance between two neighboring rods [3]. The gap is centered at frequency $\omega = 0.37\ 2\pi c/a$, which corresponds to the canonical free-space wavelength for light of 1.55 μm when $a = 0.57$ μm.

We determine the TM band structures for two different PBG waveguides in order

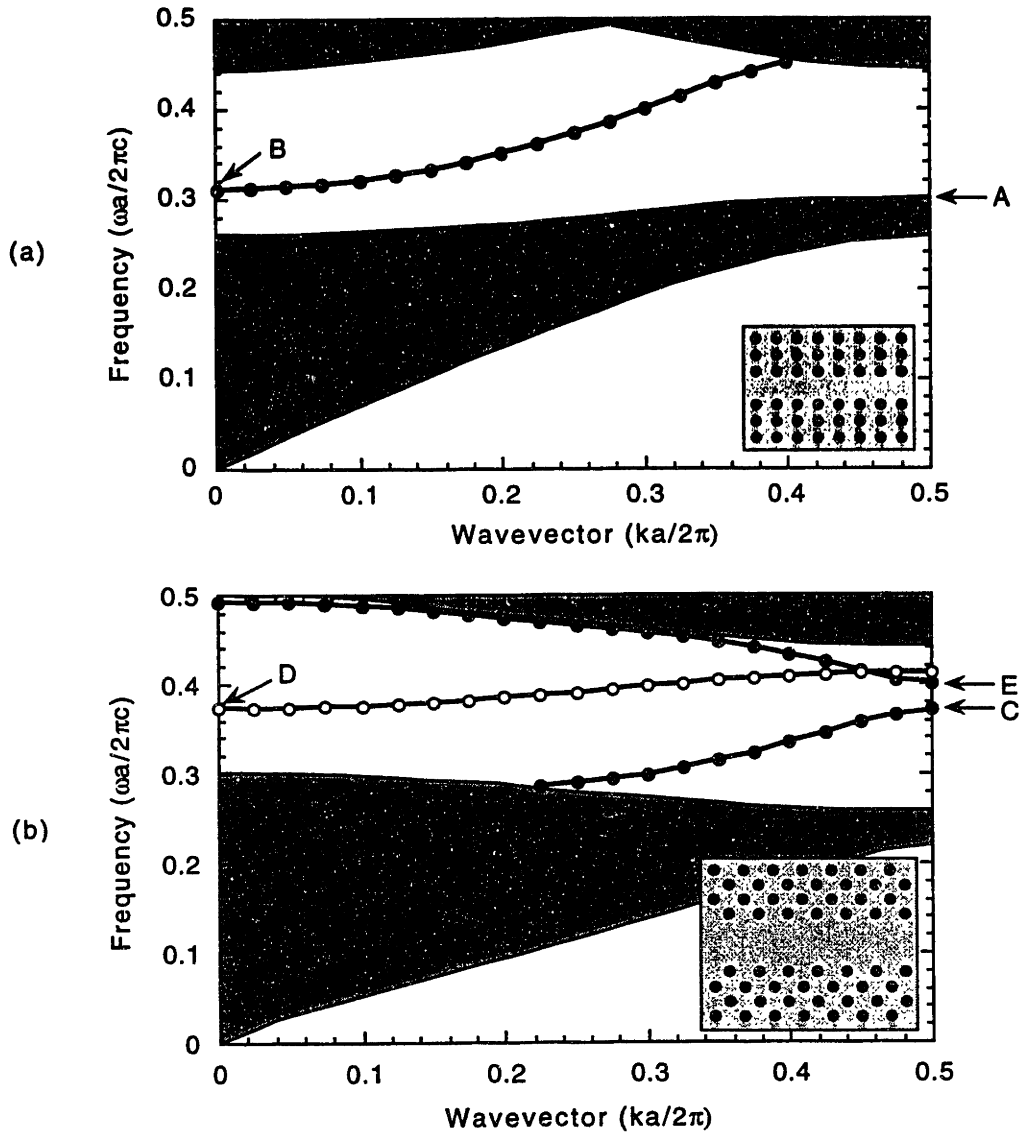

Figure 3-1: Dispersion relations for the two photonic crystal waveguides. The geometry of the waveguides is shown in the insets. The gray areas are the projected band structure of the perfect crystal. The filled circles correspond to even modes and the open circles correspond to odd modes.

to illustrate their features that are different from those in conventional waveguides. The results are shown in Fig.3-1. The horizontal axis is the wavevector in the direction of the guide, and we show the band structure in the reduced Brillouin zone scheme. The gray areas are the projections in the direction perpendicular to the guide of every mode in the band structure of the perfect crystal: these are extended modes in the crystal bulk. The modes inside the gap are localized to the row of missing rods.

In Fig.3-1.a we show the band structure for the guide created by removing a row of rods in the (10) direction of the crystal, as shown in the inset. We find a single guided mode inside the band gap. The electric field of the mode has even symmetry with respect to the mirror plane along the guide axis. The mode itself bears close resemblance to the fundamental mode of a conventional dielectric waveguide: it has a sinusoidal profile inside the guide and decays exponentially outside.

In Fig.3-1.b, the waveguide is made by removing three rows of rods in the (11) direction of the crystal (see inset). There are now three guided modes inside the gap which can again be classified according to their symmetry with respect to the mirror plane along the guide axis. The first and the third modes are even, whereas the second mode is odd.

It is generally true that the number of bands inside the band gap equals the number of rows of rods removed when creating the guide. This can be understood from a simple counting of the states in the crystal. If we decrease the dielectric constant of a single rod in a perfect crystal, we pull up one defect state from the dielectric band[2] [3, 21]. If we repeat this for a whole row of rods, we pull up N localized states in an $N \times N$ crystal: one state at each k-point for $\mathbf{k}$ along the guide. Analogously, when M rows of rods are removed, we pull up M guided modes at each $\mathbf{k}$ from the dielectric band. Nevertheless, at some $\mathbf{k}$'s the modes may have frequencies outside the band gap, and the entire band may not be contained in the gap, as is the case for instance for the lowest guided mode band in Fig.3-1.b.

[2]The dielectric/air bands is the photonic crystal analogue of the valence/conduction bands in a regular crystal. For a PBG structure, it is the band below the first band gap. Decreasing the dielectric constant of one rod is equivalent to replacing a crystal atom with an acceptor atom in an atomic crystal.

For small k, the dispersion relations behave like conventional guided modes in a metallic waveguide with a cutoff: $(\omega - \omega_{cutoff}) \propto |\mathbf{k}|^2$. For these wavevectors, the wavelength of the light is much larger then the variation in the dielectric function, so the light only "sees" an average uniform dielectric in the direction of the guide. However, close to the boundary of the Brillouin zone the bands level off. Because of the discrete translational symmetry of the crystal, the dispersion relations are repeated outside the first Brillouin zone, consequently each band is restricted to a certain frequency range. The frequencies of the modes do not grow indefinitely with increasing $|\mathbf{k}|$, as in the case of conventional dielectric and metallic waveguides. This means that there may arise situations where a complete frequency gap will exist between the guided modes themselves. We term this frequency range a *mode gap.*

Such mode gaps do exist for the waveguide in Fig.3-1.b: a small complete gap between the first and second guided mode bands, between points C and D. A larger gap for even symmetry modes can be seen between points C and E. In the case shown in Fig.3-1.a, there is also a frequency range, below the cutoff, with no guided modes or extended modes, between points A and B.

In the Appendix, we present a group theoretical analysis on the origins and on the presence and absence of mode gaps in PBG waveguides. The arguments presented can facilitate the design of waveguide configurations with suitable mode gaps.

3.4 Bound states in photonic crystal waveguides

In this section we investigate how the existence of mode gaps affect the bound state spectrum. As in conventional waveguides, one can try to create a bound state in a PBG waveguide in two different ways: by altering either the width or the curvature of the guide. First we consider what happens if only the guide width changes.

3.4.1 Bound states in straight guides

In a metallic waveguide, a wavepacket trapped in a constriction has a larger transverse momentum than any guided mode, so its frequency will be higher than the cutoff

frequency (if a cutoff exists). Such a state would decay into open channels in the guide. Therefore to create a bound state in a metal guide, one has to put a bulge into the guide, because bound states can only exist below the cutoff frequency for guided modes. If we view the guide with a bulge as three waveguide sections: two semi-infinite sections and one of finite length, the above requirement translates in terms of the dispersion relations for the two types of waveguide sections as follows: the existence of bound states requires the existence of guided modes for the finite guide section within the frequency range where no guided modes exist in the semi-infinite section.

As in conventional guides, it is possible to find bound states in photonic crystal waveguides with a bulge as well, except that we have the additional restriction that the state lie inside the band gap. If the bottom of the first guided mode is higher in frequency than the lowest frequency of the band gap, bound states can be created by increasing the width of the guide by, for instance, removing another row of rods in one section of the guide. However, in PBG waveguides, one also has an unconventional choice: we can look for a state in the gaps *between* the guided modes. As long as a part or all of a guided mode for the finite section falls into the mode gap, there is a possibility that bound states can exist within that frequency range. We illustrate this point in the following.

A guide with a mode gap for the rectangular array of rods can be formed by taking out four rows of rods in the (11) direction of the lattice. The band structure for the guide is shown in Fig.3-2.a. We find four guided modes inside the gap. Because of the symmetry of the dielectric function of the guide, the modes can again be classified as even or odd with respect to a glide plane operation consisting of a translation by $a/\sqrt{2}$ parallel to the guide axis and of a reflection across the axis. The filled circles in the figure correspond to even modes, and the open circles to odd modes. The upper two bands, having different symmetries, do cross. The two odd modes repel each other, creating a mode gap from $\omega = 0.390\ 2\pi c/a$ to $\omega = 0.417\ 2\pi c/a$.

In order to emphasize the contrast between PBG and conventional waveguides, we use a narrow constriction as the finite section to form a bound state: the guide in

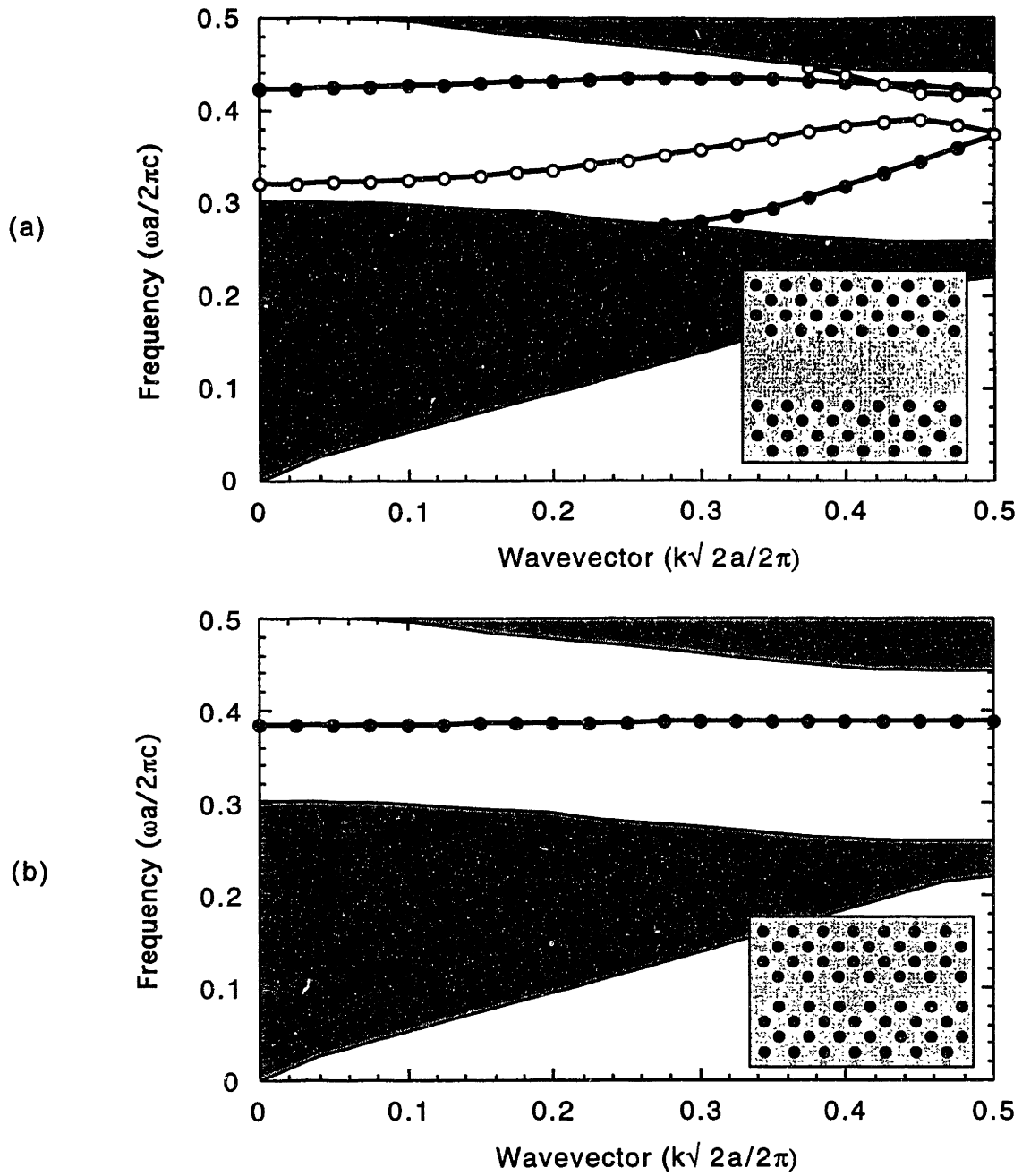

Figure 3-2: Dispersion relations for the two PBG waveguides shown in the insets. The gray areas are the projected band structure of the perfect crystal. The filled circles correspond to even modes and the open circles correspond to odd modes.

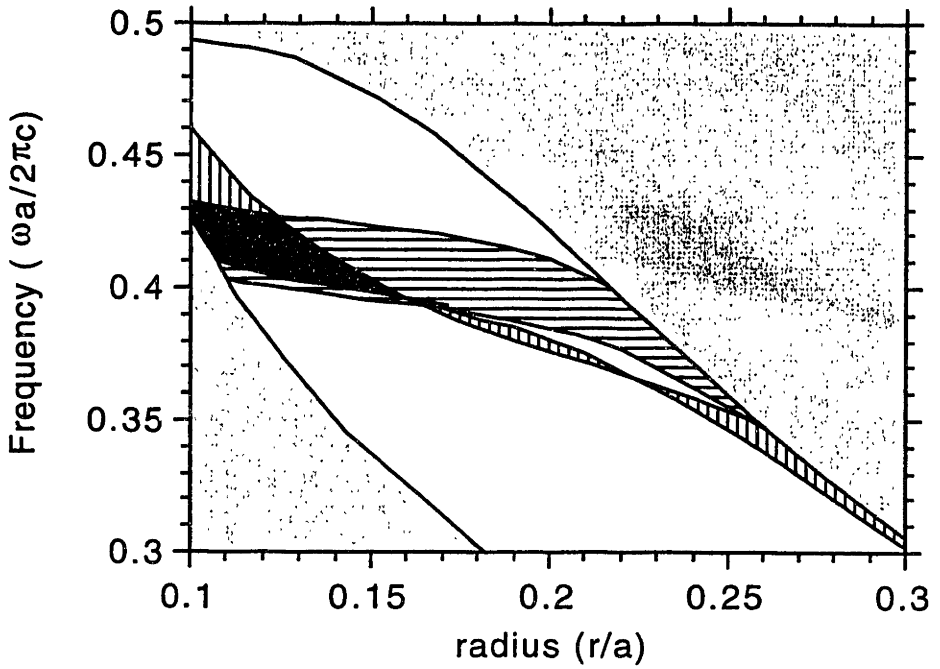

Figure 3-3: Optimizing the radius of the rods for the emergence of bound states. Horizontally hatched area: frequency range of the mode gap for the guide in Fig.3-2.a. Vertically hatched area: frequency range covered by the guided mode of the guide in Fig.3-2.b. Black shaded area: overlap of the two frequency ranges. The gray areas are the projected band structure of the perfect crystal.

the (11) direction consisting of only one missing row of rods. Fig.3-2.b displays the band structure of this guide. The single mode in the gap is even with respect to the mirror plane, and covers a frequency range from $\omega = 0.384\ 2\pi c/a$ to $\omega = 0.388\ 2\pi c/a$.

For the rod radius used so far ($r = 0.18a$) the mode gap and the guided mode do not overlap. However, we can tune r so that the guided mode of the narrow guide falls inside the mode gap of the wide guide. Fig.3-3 shows the frequency range of the mode gap (horizontal hatch) and that of the guided mode (vertical hatch) as a function of the radius of the rods. In the black shaded area the two frequency ranges overlap. The optimal radius is found to be $r = 0.12a$ for the creation of bound states. Fig.3-4 shows the two band structures at this value of r superimposed on one another. The entire guided mode band of the guide chosen as the constriction falls inside the mode gap, thereby enabling the creation of a bound state in the constriction.

By choosing a configuration such that the constriction has length $3\sqrt{2}a$, we indeed

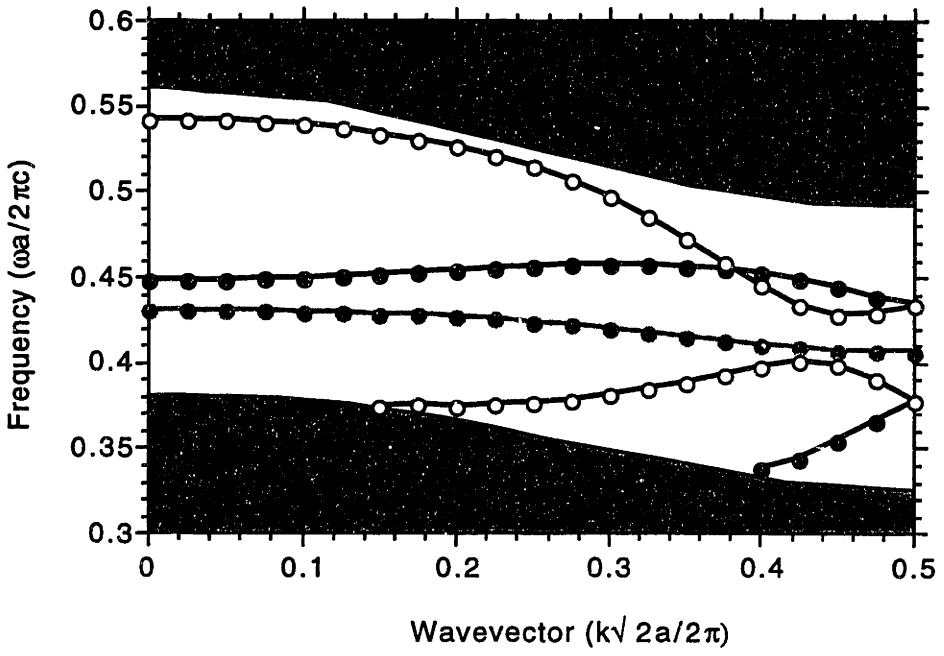

Figure 3-4: Overlap of the dispersion relations for the two guides in Fig.3-3 when the radius of the rods is $r = 0.12a$. Black line: guided modes for the wider guide. Gray line: guided mode for the narrow guide. Filled circles: even modes, open circles: odd modes. The gray areas are the projected band structure of the perfect crystal.

find a bound state at $\omega = 0.411\ 2\pi c/a$. The electric field of the mode is displayed in Fig.3-5. We note that, in general, a dielectric defect in a metallic waveguide gives rise to a completely different field distribution for the defect mode. In that case, most of the field lies inside the high dielectric region, whereas in our case most of the field is confined to the inside of the narrow guide section. Since the mode is close in frequency to the mode gap edge, the decay constant κ is small ($\kappa \simeq 0.27/a$), [3] and the electric field decays slowly in the semi-infinite section. Nevertheless, it is a *bona fide* bound state whose counterpart would be impossible to obtain in conventional waveguides.

[3]We can estimate the value of κ by analytic continuation of the function $\omega(\mathbf{k})$ to imaginary $\mathbf{k}$. If close to mode gap edge, $\omega(\mathbf{k}) \simeq \omega_0 - \alpha|\mathbf{k}|^2$, then at the bound state frequency ω_1, $\kappa \simeq \sqrt{(\omega_1 - \omega_0)/\alpha}$.

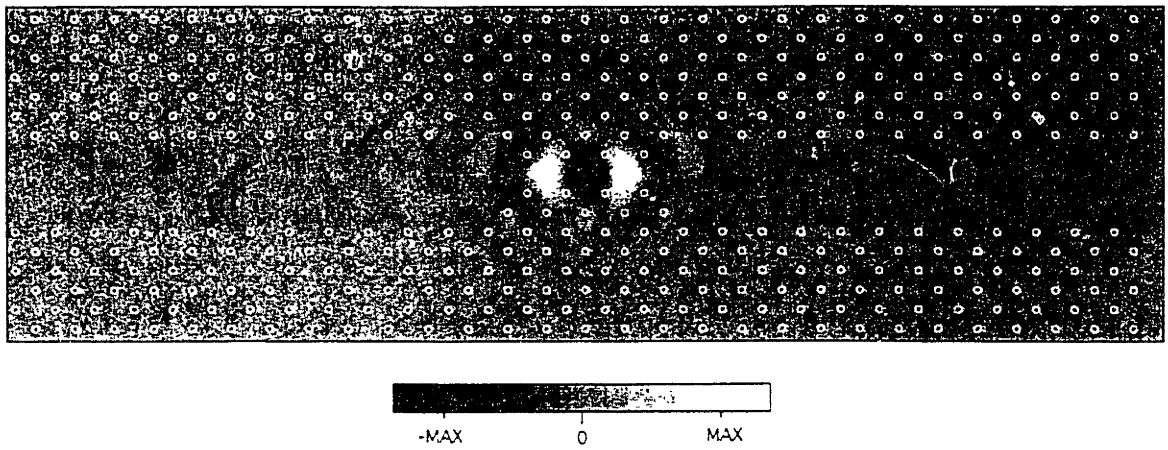

Figure 3-5: Electric field for the bound state at $\omega = 0.411\ 2\pi c/a$ in a constriction of length $3a$. Most of the field power is concentrated in the constriction itself. White circles indicate the dielectric rods.

3.4.2 Bends in waveguides

Let us now turn our attention to bends in photonic crystal waveguides. Like straight waveguides with a bulge, bent waveguides can also be viewed as one finite and two semi-infinite waveguide sections of different wavevectors and dispersion relations joined together. [19]. By analogy to the straight waveguide, we can create a bound state in a bend by joining three sections, the two semi-infinite section having a mode gap and the finite section having a guided mode in that mode gap. As an example, we show a 180° bend in Fig.3-6, where each of the three sections are identical to the three sections in Fig.3-5. We indeed find a bound state in the waveguide bend, at $\omega = 0.411\ 2\pi c/a$. Note that the localized electric field of this mode is nearly the same as that in Fig.3-5.

We again emphasize that in a metallic waveguide with this bend configuration a state inside such a narrow bend section would have a higher transverse momentum than the lowest guided mode of the semi-infinite section. This state then would decay by coupling into guided modes. This does not happen in the PBG case, even though the finite section is roughly two and a half times narrower than the semi-infinite sections. The bound state also lies closer to the guided modes than to the bulk modes in frequency, so the decay constant for the state is smaller in the guide that

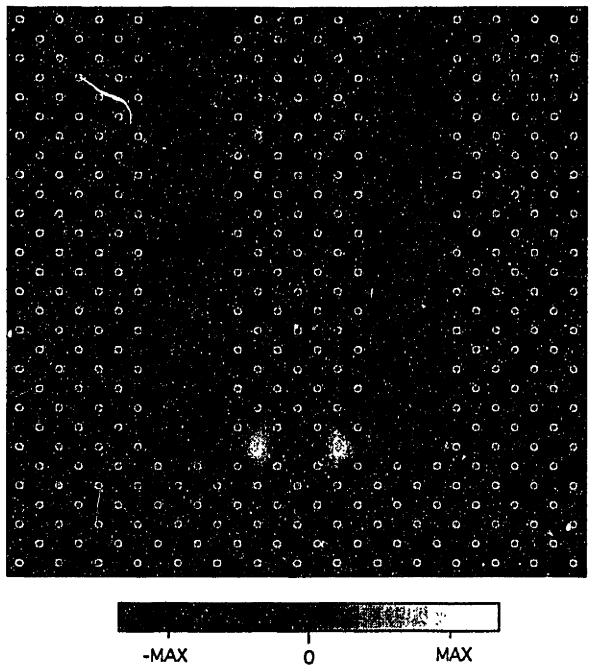

Figure 3-6: Electric field for the bound state at $\omega = 0.411\ 2\pi c/a$ in the 180° bend. White circles indicate the dielectric rods.

in the bulk. This implies that, from an experimental point of view, coupling into this bound state would be easier through the guide than through the bulk.

In order to investigate further the mechanism for the appearance of bound states in bends, we need a configuration that allows for a number of bound states to exist. Such a configuration preferably would consist of a finite section, whose guided mode covers most of the bulk gap, and of two semi-infinite sections, each possessing a guided mode band with a narrow bandwidth. We create one such configuration by removing one row of rods from the square array in the (10) and the (11) directions, respectively. The guides and their band structures at $r = 0.18a$ are shown on Fig.3-7 superimposed on one another. The dispersion relations indeed satisfy our requirements.

As the length L (indicated by the arrow in the inset) of the bend section is changed, we observe bound states of different frequencies. When $L = 3a$, we find three bound states, two even and one odd mode with respect to the mirror plane. The dielectric function and the electric field for these states is shown on the left panels of Fig.3-8. We note that the highest frequency mode is above the upper cutoff frequency of the

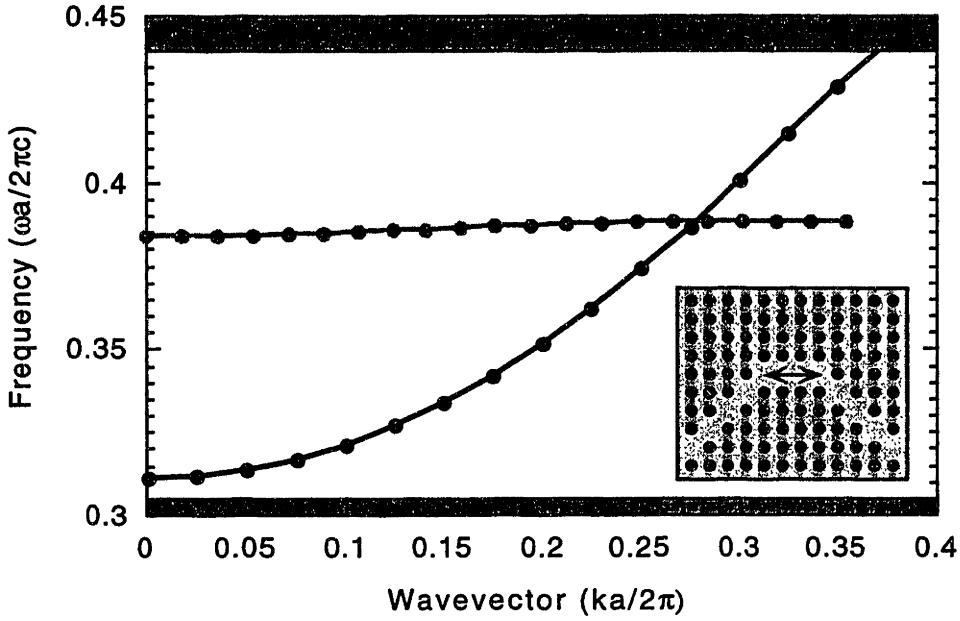

Figure 3-7: Overlap of two band structures inside the photonic band gap. Black line: guided mode for the guide in the (1,0) direction with one row of rods removed. Gray line: guided mode for the guide in the (1,1) direction with one row of rods removed. Gray area: extended modes in the crystal.

guided mode of the infinite guide section. Such a mode would not exist in analogous conventional waveguide structures, where there can only be a lower cutoff.

These bound states resemble cavity modes. Indeed, after removing the semi-infinite guide sections on both sides of the bend, we obtain similar eigenmodes at frequencies almost identical to the bound state frequencies. These modes are shown on the right panels of Fig.3-8.

We present two arguments to explain the close correspondence between bound states in PBG guides and cavity modes. In a metallic waveguide the boundary conditions for a TM bound state are $\mathbf{E} = 0$ at the guide boundaries. The bound state frequencies are determined by matching the decaying solution outside the bend to the field inside the bend. By closing off the bend section, we require that the field be zero at the ends of the bend section, so the frequencies of the cavity modes may differ considerably from those of bound states. In the case of photonic crystals, zero boundary conditions are not required at the guide edges, because there are exponen-

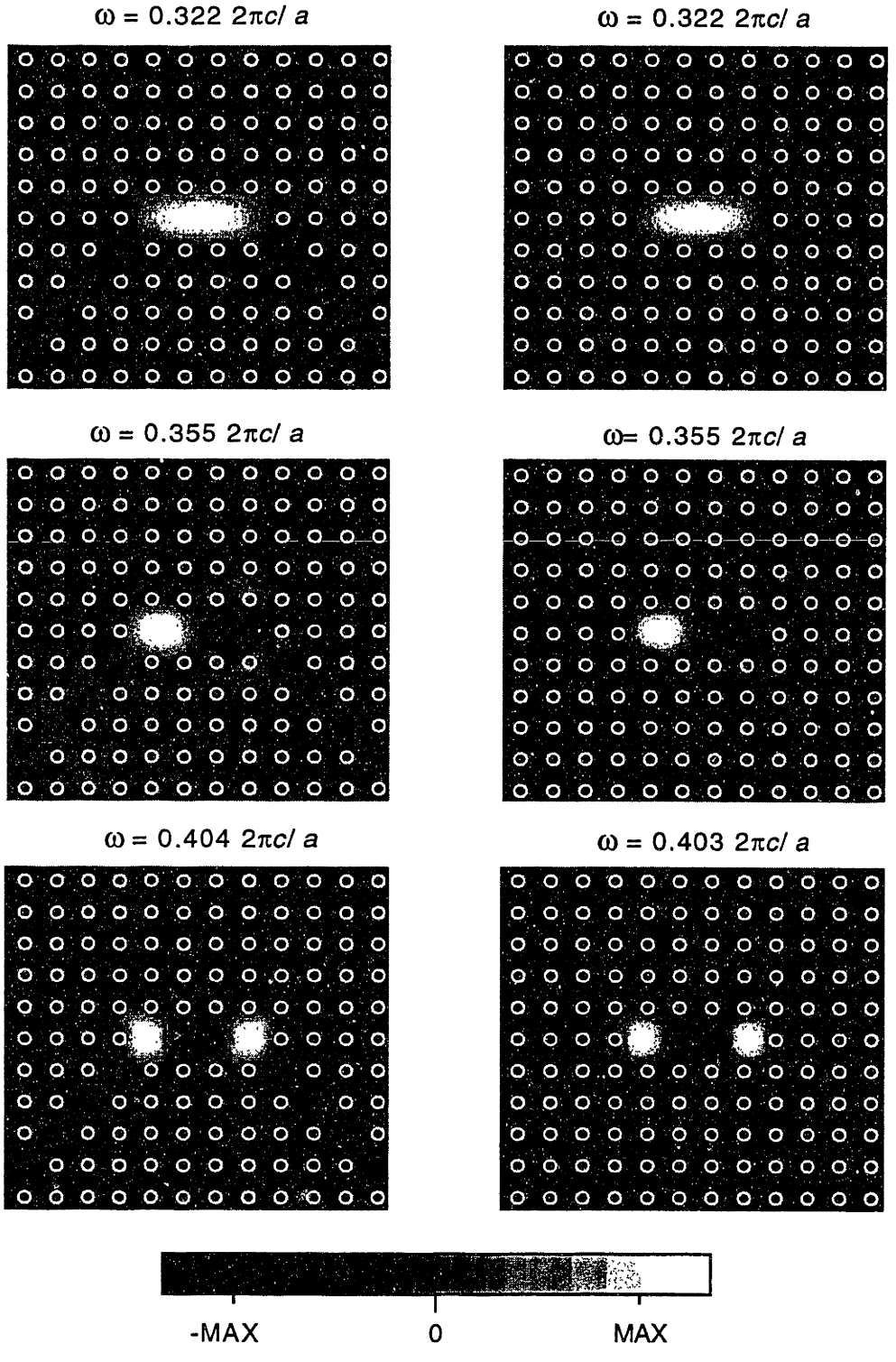

Figure 3-8: Left panels: electric fields and frequencies of the three bound states inside the gap for the bend with length of the bend section $L = 3a$. Right panels: electric fields and frequencies of the corresponding cavity modes.

tially decaying solutions in the crystal bulk. Thus the mode-matching requirement at the ends of the open bend (decaying field into the guide) does not differ greatly from the boundary condition for a cavity mode (decaying field into the bulk).

Another reason for the small shift in the frequencies when the waveguide is closed off is the following. To calculate the TM modes of a 2D photonic crystal structure with dielectric function $\epsilon(\mathbf{r})$, one can solve the following eigenvalue equation for the scalar electric field $E(\mathbf{r})$:

$$-\left(\frac{\partial^2}{\partial x^2}+\frac{\partial^2}{\partial y^2}\right)E(\mathbf{r})=\frac{\omega^2}{c^2}\epsilon(\mathbf{r})E(\mathbf{r}) \tag{3.1}$$

by minimizing the energy functional:

$$\frac{\int \frac{1}{\epsilon(\mathbf{r})}E^*(\mathbf{r})\left(\frac{\partial^2}{\partial x^2}+\frac{\partial^2}{\partial y^2}\right)E(\mathbf{r})\,dr}{2\int E(\mathbf{r})^2\,dr} \tag{3.2}$$

If the waveguides are open, the solution $E(\mathbf{r})$ is small outside the bend section since the bound states decay exponentially into the guide. Changing $\epsilon(\mathbf{r})$ in that part of the guide by closing off the bend section then causes only a small perturbation in the quantity in the numerator, so the frequencies change only minimally.

For shorter bend sections, we find the following bound states: for $L = 2a$, $\omega = 0.330\ 2\pi c/a$ (even), $\omega = 0.379\ 2\pi c/a$ (odd); for $L = a$, $\omega = 0.344\ 2\pi c/a$ (even), all corresponding to cavity modes (the fields are not shown). By analogy, we might expect the 90° bend ($L = 0$) to have one bound state, in the bend corner, corresponding to the cavity mode for one missing rod in an otherwise perfect crystal. Yet, instead we find two bound states, neither of which is localized in the corner. One of the states is even and the other one is odd with respect to the mirror plane, as shown on the left panels of Fig.3-9. Both states are localized at the two vacancy sites $\sqrt{2}a$ away from the corner.

This anomalous behavior is due to the fact that the frequency of the mode for the single rod cavity is $\omega = 0.385\ 2\pi c/a$, which falls in the guided range of the semi-infinite sections of the guide. (This is reasonable, because this cavity mode locally

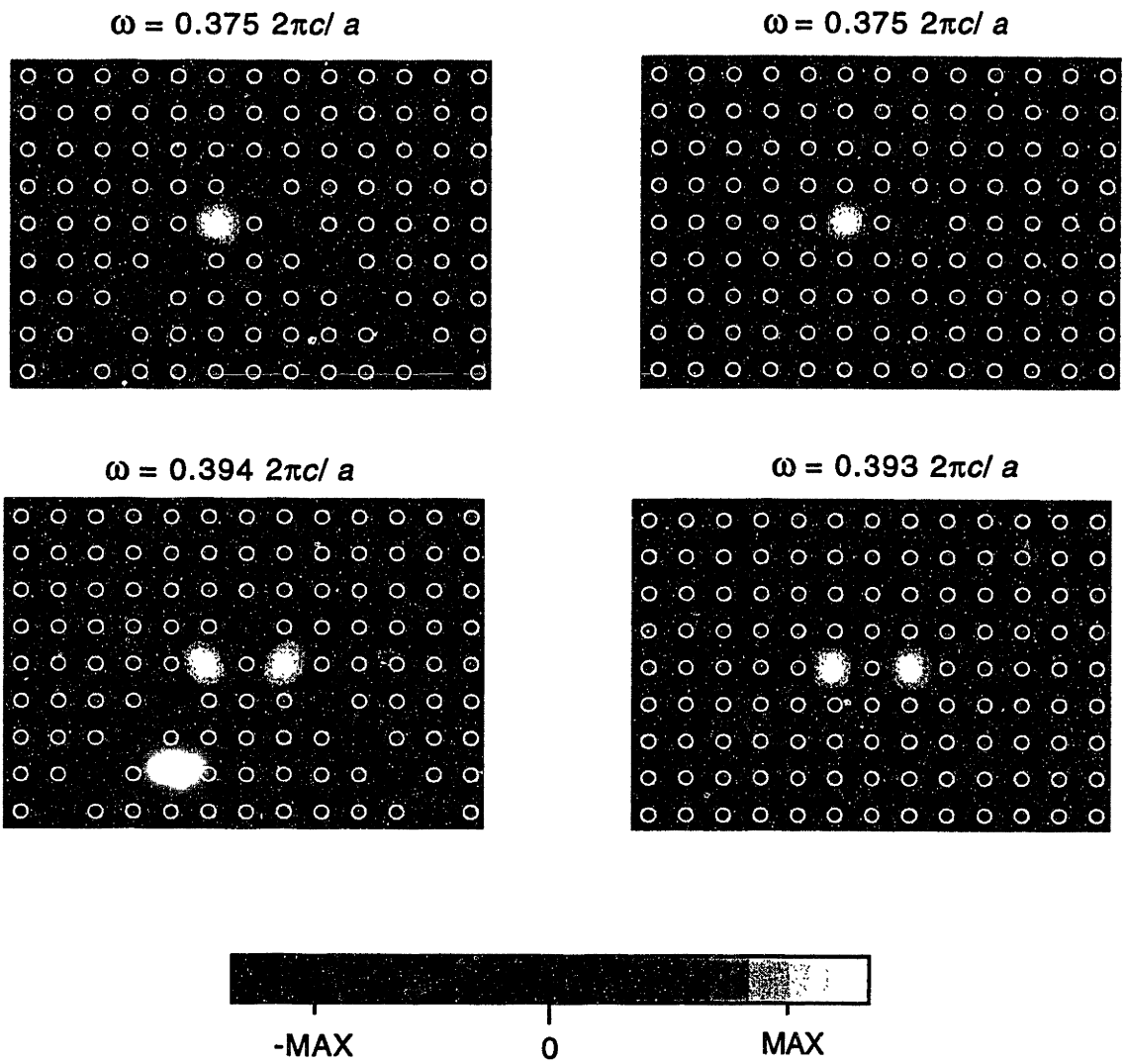

Figure 3-9: Left panels: electric fields and frequencies of the two bound states inside the gap for the 90 bend. Right panels: electric fields and frequencies of the corresponding cavity modes.

is similar to the guided mode for wavelength $\lambda = 2\sqrt{2}a$, or, for $k = \pi/\sqrt{2}a$.) This cavity mode couples with the guided modes, and it shows up as a resonance in the bend corner.

The two bound states instead correspond to the coupled cavity modes shown on the right panels of Fig.3-9. The cavity is composed of two vacancies, with their centers separated by two lattice constants. As pointed out earlier, each vacancy by itself supports a cavity mode at $\omega = 0.385\ 2\pi c/a$, which would lie in the guided range of the infinite sections of the guide. However, since the vacancies are in close proximity with each other, there is a finite coupling between them, which in turn split the otherwise degenerate levels into an odd and an even bound state, with frequencies that respectively fall just below and just above the guided mode frequency range. Such unconventional bound states demonstrate that bound state creation in PBG waveguide bends cannot always be described in a one-dimensional framework, and they can strongly depend on dielectric function.

3.5 Summary

We have shown that the periodicity of the photonic crystal waveguide gives rise to mode gaps between different guided modes. Such mode gaps make it possible to create bound states in a waveguide with a constriction and in bends. Bound states in PBG bends closely correspond to cavity modes. We have also observed that the existence of certain bound states can critically depend on the geometry of the bend in question and cannot always be predicted using arguments based on one-dimensional models.

3.6 Appendix

In this part of the chapter, we demonstrate how it is possible to give a simple explanation of the main qualitative and quantitative characteristics of the PBG waveguide dispersion relations, including the appearance of mode gaps. We show that the differ-

ent types of mode gaps in band structures seen earlier arise from simple symmetries of the dielectric function. The following group theoretical analysis allows one to design waveguides with suitable mode gaps easily.

As we have seen, photonic crystal guided mode fields resemble modes in conventional waveguides. So, in order to find the band structure for PBG guides, we start out with the exactly solvable case of TM modes in a straight hollow two-dimensional metallic waveguide. First we consider a metallic waveguide of width b, on which we have imposed an artificial periodicity d. For TM modes, Maxwell's equations for the electric field $\mathbf{E} = E(x,y)e^{i\omega t}$ yield:

$$\left(\frac{\partial^2}{\partial x^2} + \frac{\partial^2}{\partial y^2}\right) E(x,y) = \frac{\omega^2}{c^2} E(x,y) \tag{3.3}$$

with boundary conditions $E(x,y) = 0$ at $y = \pm b/2$. Because of the periodicity in the x-direction, we can classify the modes by their wavevector $\mathbf{k} = (2\pi/d)\tilde{k}\hat{x}$. One possible set of basis functions for this $\mathbf{k}$ is $\{e^{2(l+\tilde{k})\pi i x/d} \sin[m\pi(y/b + 1/2)]\}$, with $l = 0, \pm 1, \pm 2, \ldots$ and $m = 1, 2, 3, \ldots$. Each function in the set corresponds to an eigenvalue with $\omega = (2\pi c/d)\sqrt{(l+\tilde{k})^2 + m^2/4v^2}$, where $v = b/d$ is the relative width of the waveguide.

The dispersion relations for the metallic waveguide are altered in two ways in PBG guides. Firstly, the bands that are outside the first Brillouin zone fold back because the periodicity is no longer artificial. Secondly, bands crossing may repel each other when continuous translational symmetry is lost as the metallic boundaries are replaced by the PBG material. Yet, discrete translational symmetry is always retained, as well as symmetry under a certain point group G, which depends on the dielectric function of the guide.

First, let us consider guides that are invariant under $G = \{E, \sigma_x, \sigma_y, I\}$. E here is the identity operator, σ_x and σ_y are reflections across the x- and the y-axes, respectively, and I is inversion through the origin. (Such are the guides in Fig.3-1) Since the periodicity is only in the x-direction, the irreducible Brillouin zone is a line from Γ ($\tilde{k} = 0$) through Δ ($0 < \tilde{k} < 1/2$) to X ($\tilde{k} = 1/2$). For Δ, the point group is

$\{E, \sigma_y\}$, so the guided modes can be divided into ones that are even or odd under σ_y. At both of the high symmetry points Γ and X the point group is just G, which has four irreducible one dimensional representations.

Keeping the symmetry under σ_x in mind, we choose the unit cell such that the centers of the rods at the guide edge are at $x = 0$. In vacuum, a pair of degenerate modes at X consists of an even and an odd mode under σ_x. They always have the same symmetry under σ_y. The odd mode has a node at $x = 0$ whereas the even one has a maximum there. Since in the PBG guide the even mode has a higher fill factor[4] than the odd one, it must have a lower frequency. In this way the degeneracy of the modes at X is removed, and the level splitting creates mode gaps at the Brillouin zone edge.

The left panels of Fig.3-10 show the band structures calculated from symmetrizing the basis function set, with the actual dispersion relations for three PBG guides to the right of each plot.

The periodicity d and the relative width v used in the three calculations are inidicated on the plots. The black lines denote even modes, and the gray lines denote odd ones. Having taken into account the fact that degenerate modes repel each other, a remarkable similarity can be seen between the corresponding band structures in the frequency range of the band gap.

In this work, we also investigated another type of guide, shown in Fig.3-3.a. This guide is invariant under a different group of symmetry operations
$G = \{E, \{\sigma_x|\mathbf{f}\}, \{\sigma_y|\mathbf{f}\}, I\}$, where $\mathbf{f}$ is the fractional translation equal to $d/2\ \hat{x}$. Because the group is now non-symmorphic, the point group size doubles at X, and we obtain five irreducible representations. The degenerate pairs of the basis functions at X always belong to the same two-dimensional irreducible representation. This representation is compatible with the sum of an even and an odd representation along Δ. The essential degeneracy at X is due to the non-symmorphicity of the symmetry group and is not influenced by the specific features of the dielectric function, therefore

[4]The fill factor is defined as the ratio $I_{\text{high dielectric}}/I_{\text{crystal}}$, where $I_V = \int_V E(\mathbf{r})D(\mathbf{r})d\mathbf{r}$. High fill factor means that a lot of field is in the high dielectric, so the frequency of the mode is low.

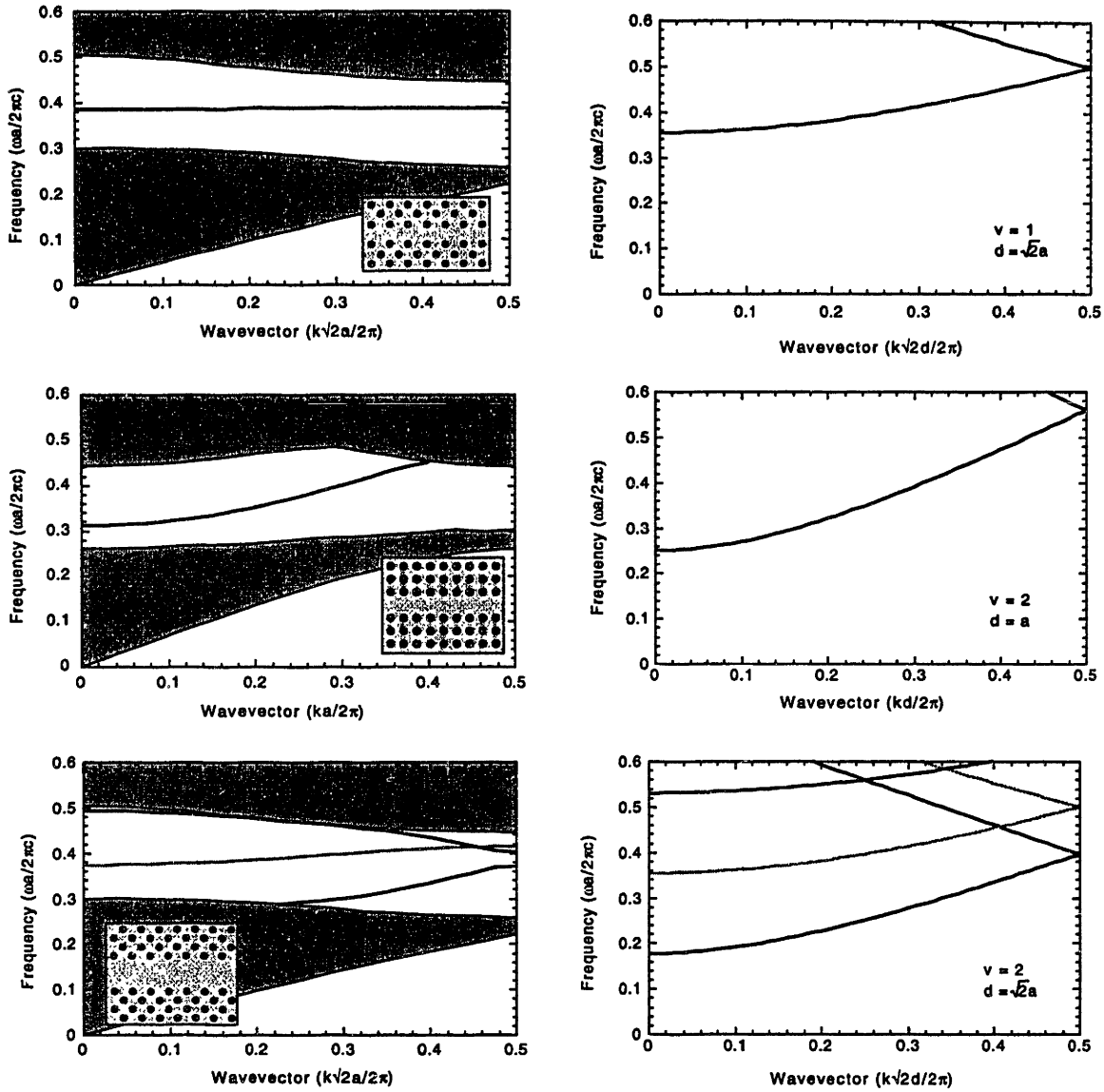

Figure 3-10: Left panels: Dispersion relations calculated from symmetrizing a set of basis functions for the symmetry group G. The relative widths are taken to be $v = 1$, $v = 2$, and $v = 2$, respectively. Right panels: band structures for the PBG waveguides displayed in the insets. The gray areas are the projected band structure of the perfect crystal. Black lines: even modes, gray lines: odd modes.

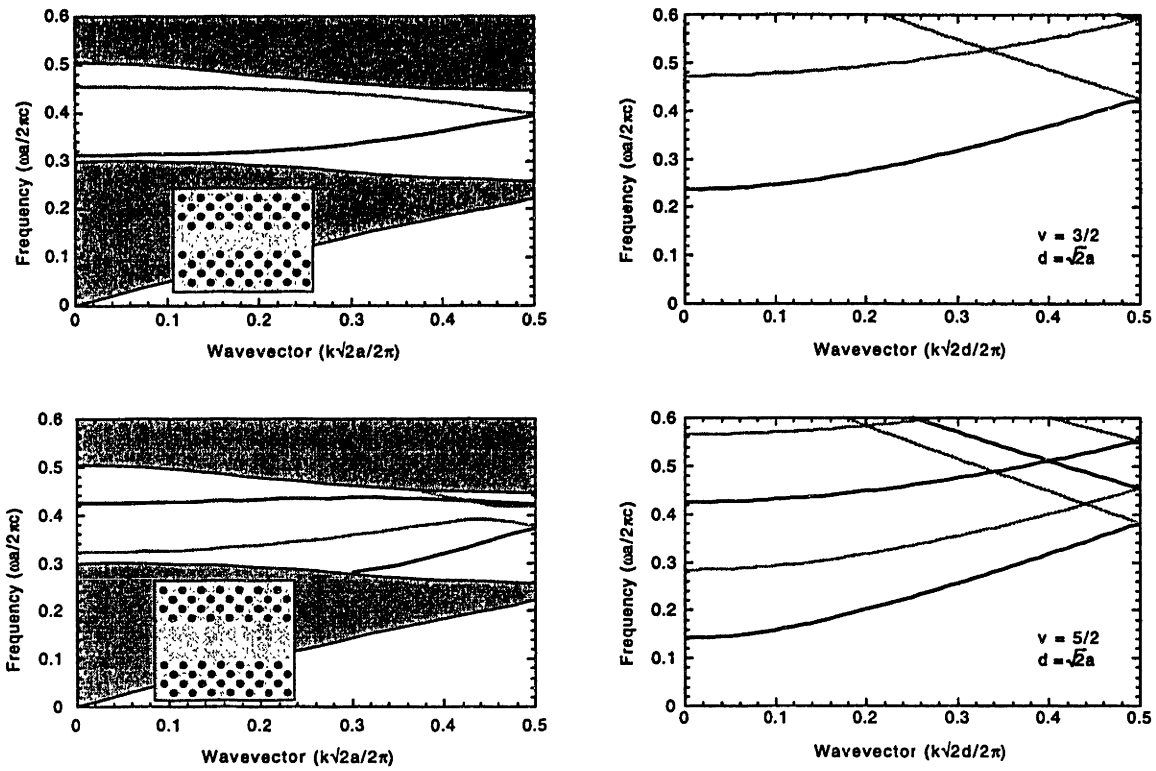

Figure 3-11: Left panels: Dispersion relations calculated from symmetrizing a set of basis functions for the non-symmorphic group G'. The relative widths are taken to be $v = 1.5$, and $v = 2.5$, respectively. Right panels: band structures for the PBG waveguides displayed in the insets. The gray areas are the projected band structure of the perfect crystal. Black lines: even modes, gray lines: odd modes.

no mode gaps open up at the Brillouin zone edge. However, because the symmetries of individual bands have also changed, some bands that were allowed to cross in the case of the symmorphic group will now repel, and this effect produces new mode gaps.

We compare two PBG guide band structures with the dispersion relations calculated from symmetrizing the basis function set in Fig.3-11. The two guides examined are ones created by removing two and four rows of rods in the (11) crystal direction, respectively, as shown on the insets. The periodicity d and the relative width v used are indicated on the plots. As expected, mode gaps open up solely when bands of the same symmetry repel.

Chapter 4

Tapered couplers for efficient interfacing between dielectric and photonic crystal waveguides

4.1 Introduction

Photonic band gap (PBG) guiding is a mechanism for light guidance that has no parallel in traditional dielectric waveguides. Line defects made of air in photonic crystals (PCs) can guide optical light in air, above the light line $\omega = ck$, because they do not rely on traditional index guiding. Photonic band gap guiding was first proposed theoretically [5, 3] and has been demonstrated experimentally as well [22, 23]. In part because of the absence of radiation modes, PC waveguides can be bent very sharply, on the order of the guided light wavelength, while maintaining almost perfect transmission through the bend [19, 24].

Nevertheless, to use PC waveguides in integrated optical circuits, light must be efficiently coupled from traditional dielectric waveguides and fibers into and out of the air defects in photonic band gap materials. Because of the different underlying physics of traditional index guiding and PBG guiding, coupling light into and out of photonic crystal waveguides is not a trivial problem. Results from microwave

experiments with alumina PCs demonstrate that there are large insertion losses when electromagnetic waves are coupled into and out of PC waveguides [24]. This results in substantial reflection and scattering from PC waveguide ends, which adversely affects the outcome of transmission measurements. To overcome this limitation, we need an efficient waveguide junction design.

One way to achieve coupling is to use a resonant mode to couple the modes in the two types of waveguides. By judiciously choosing the coupling coefficients of the guided modes to the resonance, in principle very high transmission can be achieved. However, limits are set on the useful bandwidth by the resonance width. In this chapter we investigate a non-resonant way of coupling between the two types of waveguides to achieve high transmission for a large frequency range. Specifically, we consider tapered waveguide terminations for dielectric waveguides.

4.2 Model system and simulation methods

We restrict our attention to waveguide junctions for two-dimensional waveguides, as this has been the focus of recent theoretical and experimental investigation. In Fig.4-1 the dispersion relations for the two types of waveguides considered in this chapter are plotted. The PC we use is composed of a square array of dielectric rods of lattice constant a. The rods have a circular cross-section of radius $0.2a$ and a refractive index $n = 3.4$, appropriate for silicon at 1.55 μm wavelength. The PC has a large band gap for TM polarized modes. The waveguide is a simple line defect in the crystal, created by removing a line of rods, as shown in the inset on Fig.4-1.a. The solid line in Fig.4-1.a shows the dispersion relation for the guided modes. Its cutoff is at frequency $\omega = 0.304\ 2\pi c/a$ and it is single-mode in the band gap above cutoff. The dispersion relations for a dielectric waveguide of width w are plotted in Fig.4-1.b. Filled/open circles stand for even/odd modes with respect to the line along the guide center. As the width of the waveguide increases, so does the number of modes present at a certain frequency.

We calculate the transmission through PC/dielectric waveguide junctions by nu-

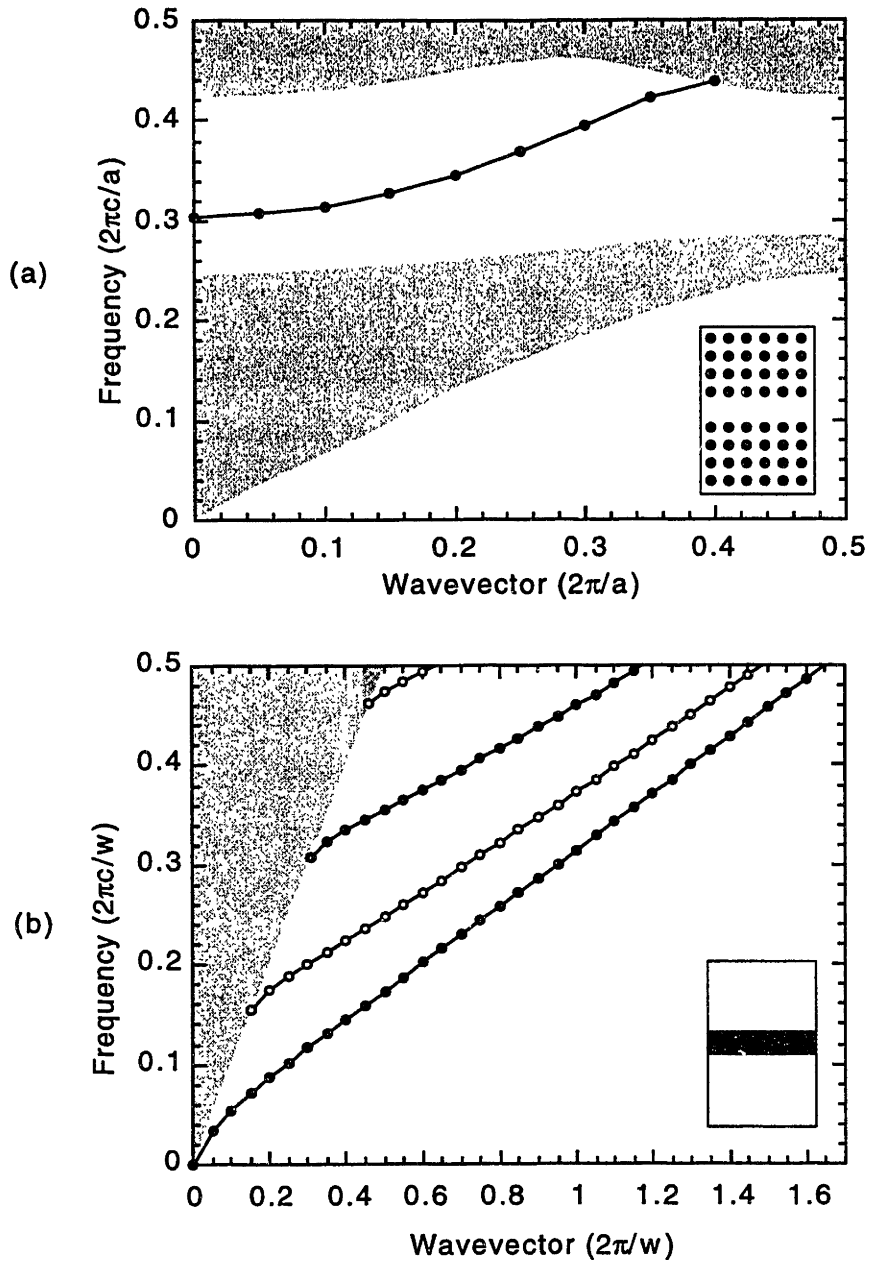

Figure 4-1: a) The band structure of the photonic crystal waveguide shown in the inset (solid line). The gray areas stand for extended modes in the bulk photonic crystal. b) Dispersion relations for a dielectric waveguide of width a shown in the inset. Filled/empty cirles represent even/odd modes, and the gray area stands for radiation modes above the light line.

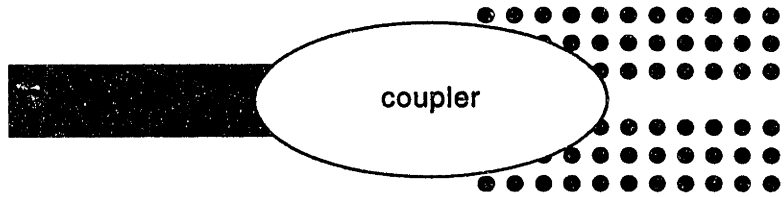

Figure 4-2: Schematic of a junction between a photonic crystal and a traditional dielectric waveguide used in the numerical simulations.

merically simulating pulse propagation. The electromagnetic fields are found by solving Maxwell's equations in a finite-difference scheme in the time domain [25]. We use perfectly matching layer absorbing boundary conditions at the computational cell edges [20, 6]. The cell contains both waveguides, aligned with their axes coinciding, and an arbitrarily shaped coupler. An example of the computational cell is shown schematically on Fig.4-3.a for output coupling. The fundamental mode is excited at the end of the input waveguide by a row of dipoles that have TM polarization and the appropriate mode profile. The pulse generated has a Gaussian shape in time, a center frequency $\omega_0 = 0.36\ 2\pi c/a$ and covers a frequency range of about $0.04\ 2\pi c/a$.

The pulse propagates along the input waveguide. As it traverses the coupler, part of the power is transmitted into the output coupler, some of it is reflected, and the rest is lost to radiation modes. Since we do not rely on resonant coupling, we expect that the efficiency of the coupler will not vary greatly within the frequency range covered by the pulse. So to determine the transmission and reflection coefficients, we measure the total flux as a function of time along a line perpendicular to the guide in both the input and the output waveguides. In the example in Fig.4-3.a, the input and reflection is measured at A in the PC waveguide and the transmission at B in the dielectric waveguide.

As an example, we calculate transmission for a junction created by placing a flatly terminated dielectric waveguide at the exit end of the PC waveguide, The flux as a function of time is plotted in Fig.4-3.b, and the coupler configuration is shown in the inset. At point A, the signal consists of two peaks, the first peak is the incident pulse and the second one is the reflected pulse. By choosing a long enough waveguide, the

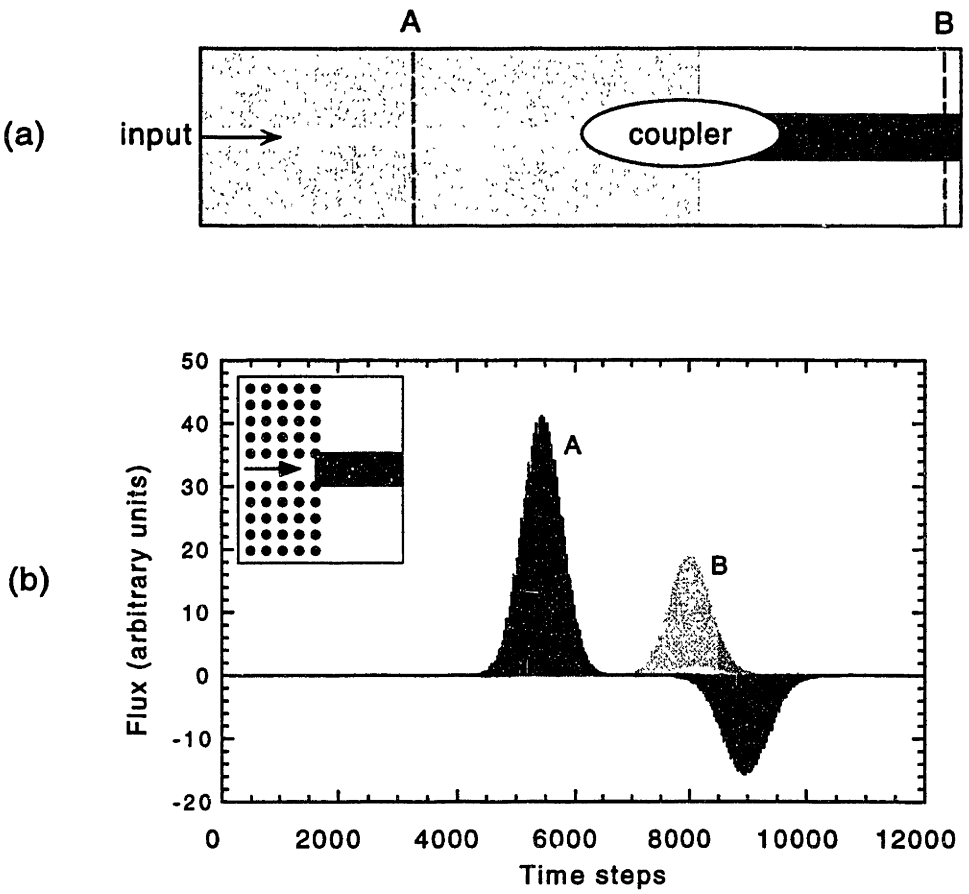

Figure 4-3: a) Schematic of the computational cell used. The input source is denote by the arrow. The flux is measured along the dashed lines at A and B. b) Flux measured at A (black line) and at B (gray line) as a function of time for the coupler configuration shown in the inset. The arrow indicates the propagation direction of the input pulse.

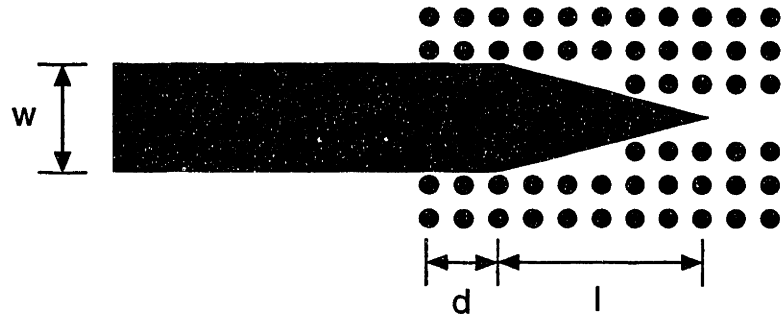

Figure 4-4: Tapered coupler for coupling into a photonic crystal waveguide.

two pulses become separated in time.[1] At point B the transmission peak is clearly distinguishable. The fluxes are integrated in time to find the transmission through the junction, which is 55% in this case.

4.3 Coupling into a photonic crystal waveguide

Dielectric waveguides in integrated circuits as well as optical fibers have sizes on the order of a few microns. The PC that we use in our simulations must have a lattice constant of about $a = 600$ nm so light is guided at the standard optical communication wavelength of 1.55 μm. If we simply terminate a wide dielectric waveguide flat and place it next to a PC waveguide, which has width of about 1 micron, coupling is very inefficient. We calculate transmission for a waveguide of width $6a$ that ends a distance a before the PC. We find that in the vicinity of the frequency ω_0, only 22% of the power is coupled into the PC waveguide. One of the reasons for this is the poor mode profile-matching between the fundamental modes of the wide dielectric and of the much narrower PC waveguide.

A taper can reduce the dielectric waveguide cross-section adiabatically in a relatively short distance while still retaining almost perfect throughput. For instance, with a taper of length $10a$ one can join a waveguide of width $7a$ to one with width $2a$ with 100% transmission within numerical accuracy of our calculations. So we can

[1]Since there is reflection at the the photonic crystal waveguide end at the computational cell edges, the cell must be chosen long enough so the useful and the parasite pulses can be distinguished [19].

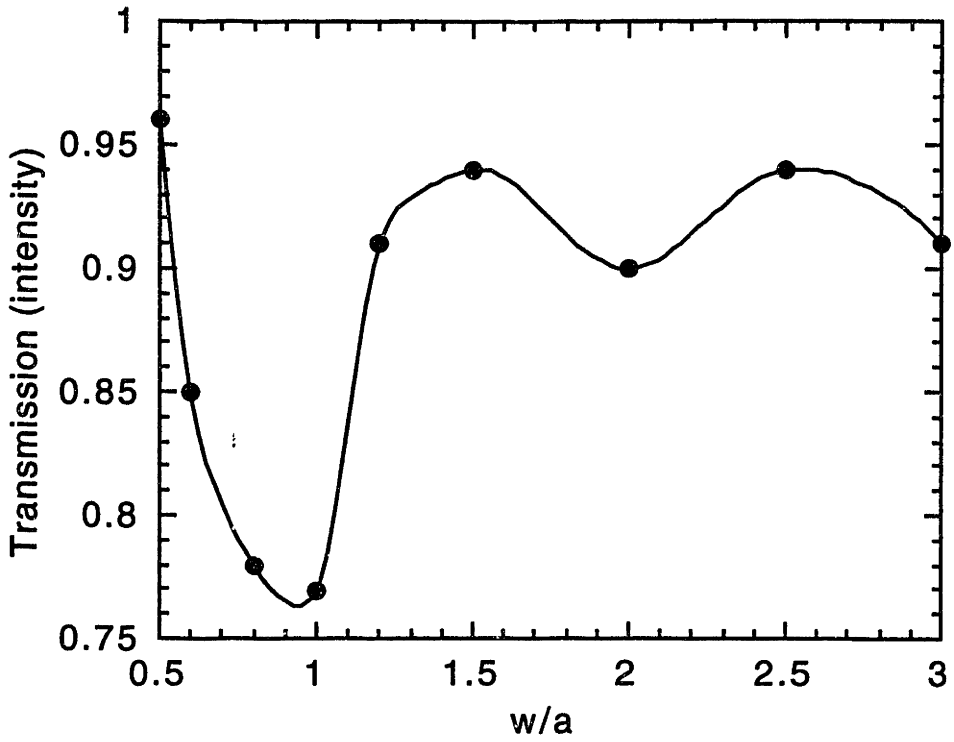

Figure 4-5: Transmission efficiency as a function of the input waveguide width for coupling into a photonic crystal waveguide. The circles are calculated values and the solid line is an interpolated curve.

focus our attention on input couling from dielectric waveguides with a width that is on the order of the lattice constant. The tapered coupler investigated is shown in Fig.4-4. The width of the dielectric waveguide is w, the taper length is l and the taper begins at distance d from the line defined by the centers of the posts comprising the photonic crystal edge. Since the taper intrudes into the PC itself, some posts comprising the crystal may touch the dielectric guide coupler, adding roughness to the taper. In general, the measured transmission values improved by only about 1% when the posts were removed. The results given in this section were obtained without these posts, as it is done in Fig.4-4.

In Fig.4-5 we plot the transmission as a function of the guide width w for the fixed values $d = 5a$ and $l = 10a$. There is a major improvement in the transmission, it is greater than 90% and reaches 96% at $w = a/2$. In the vicinity of $w = a$, however, transmission becomes as low as 77%. To explain the large dip in the transmission, let

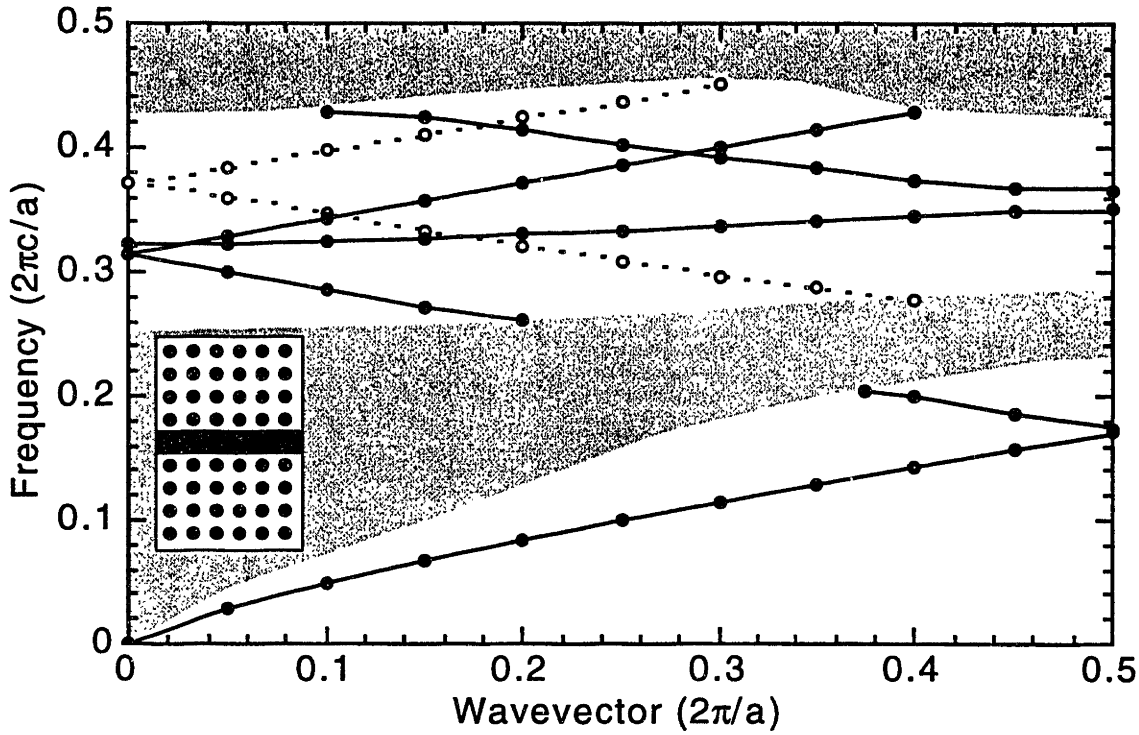

Figure 4-6: Band structure for a dielectric waveguide of width a placed inside a photonic crystal waveguide as shown in the inset. Dashed/solid lines (and full/empty circles) represent even/odd modes, and the gray area stands for photonic crystal bulk modes.

us first consider what happens to the dispersion relation of the dielectric waveguide if it is placed inside a photonic crystal. The continuous translational symmetry of the waveguide is broken and is replaced by a discrete translational symmetry. The guide mode bands shown in Fig.4-2.b are folded back into the first Brillouin zone, and Bragg reflections can open up band gaps at the zone edges. We compute the band structure for a waveguide of width $w = a$ inside the PC waveguide, shown in Fig.4-6. The bands corresponding to even/odd modes are denoted by solid/dashed lines. We observe a *mode gap* [26] at the Brillouin zone edge at around ω_0, between frequencies $\omega = 0.351$ and $0.365\ 2\pi c/a$. It is the the third band in the dispersion relation of the waveguide without the PC (Fig.4-1.b) that is split at the Brillouin zone edge. Indeed, we can read off Fig.4-1.b that this band has wavevector $k = \pi/a$ at the pulse frequency ω_0.

As the pulse launched into the waveguide arrives at the PC edge, the fundamental mode of the dielectric waveguide is coupled to the modes correponding to the even modes around the pulse frequency. The incoming mode does not only couple to the folded back lowest order mode but also to the bands obtained by folding back the third order mode in Fig.4-1.b, because the fundamental mode profile changes due to the influence of the PC. This mode conversion can be quite efficient if w is not close to a, as can be seen from the high transmission efficiency in Fig.4-5. However, if $w \approx a$, then one of the modes in the frequency range of the mode gap acquires an exponentially decaying profile towards the inside of the PC, and the power coupled into this mode is reflected from the junction. To demonstrate this, we calculated the efficiency of coupling of modes in the dielectric waveguide ($w = a$) in air to the same guide inside the PC by launching a pulse with frequency ω_0 into the dielectric waveguide in air. We find that only 57% of the incident power reaches a distance $35a$ in the guide inside the PC, the rest is Bragg reflected.

However, transmission through the tapered junction is still greater than 57%. The reason for this is that the mode gap is small and thus the decay constant for the field in the mode gap is fairly large, greater than $\kappa \approx 1/4a$. [2] Therefore, in our setup, coupling to the PC waveguide mode is still possible through the mode with the decaying profile as the taper is begins at a distance away from the PC edge that is comparable to the decay length $1/\kappa$. Nevertheless, the coupling efficiency is still affected, causing the dip in the transmission at around $w = a$. A similar but smaller dip can be seen at $w = 2a$ as well. One can check that this is due to the opening up of another mode gap: when $w = 1.87a$, the fifth order mode in Fig.4-2.b has wavevector $k = \pi/a$ at the pulse frequency.

We choose $w = 1.5a$ to continue our investigation of the effect of the taper parameters on the transmission efficiency. In Fig.4-7 we plot transmission as a function of the taper length l. The transmission increases with l, and flattens out at about

[2]The decay constant is the smallest in the gap center and there it can be estimated by $\kappa = v_g \omega_{gap}/\sqrt{2}$ where v_g is the group velocity of the mode in the dielectric waveguide in air and ω_{gap} is the gap size.

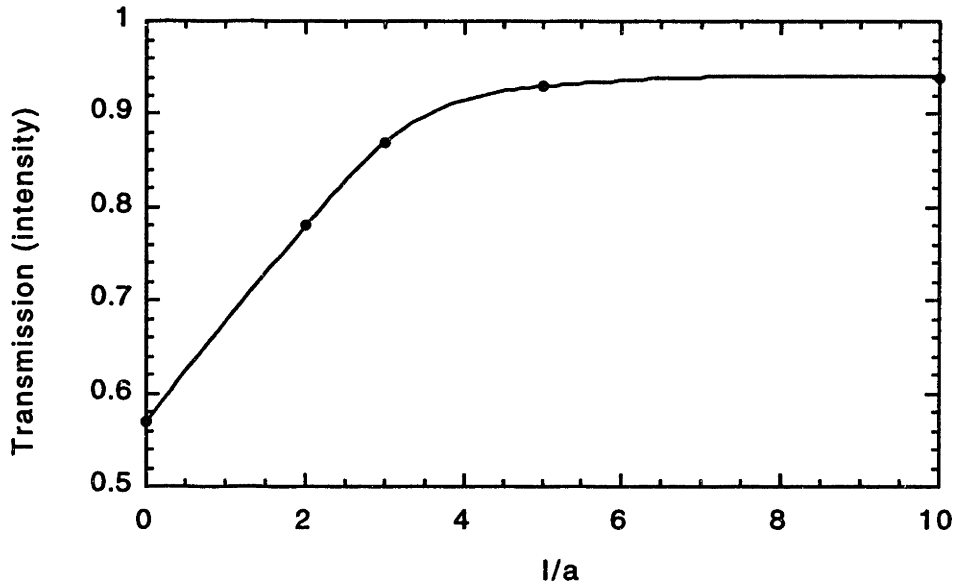

Figure 4-7: Transmission efficiency as a function of the taper length for coupling into a photonic crystal waveguide.

$l = 4a$. The cross-over happens at l approximately equal to the wavelength of the light in air. This underscores that the taper works efficiently because it changes the width of the dielectric waveguide to zero cross-section adiabatically, that is, on a length-scale larger than the light wavelength. Fig.4-8 shows the electric field in the junction for a dielectric waveguide of width $w = 0.5a$ and taper length $l = 10a$ as the pulse propagates through it. Note that the light wavelength changes gradually as the pulse propagates from the dielectric into the air.

The parameter d denotes the distance of the beginning of the taper from the PC edge. According to our calculations, the efficiency of the coupler is not a strong function of d, however, for $d \approx 0$ there can be radiation losses to free space modes. As it can be seen in Fig.4-8, it is the last section of the taper where most of the coupling action occurs, so as long as d is such that this last section is inside the PC, no radiation losses are suffered and transmission remains high.

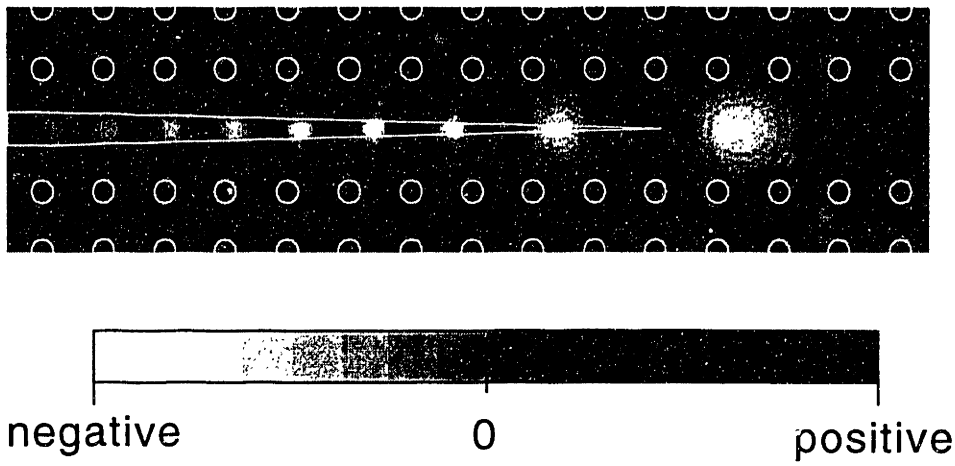

Figure 4-8: Electric field in the taper section in a grayscale scheme for a pulse propagating from the dielectric waveguide into the photonic crystal waveguide. The white circles indicate te photonic crystal and the white line the taper.

4.4 Coupling out of a photonic crystal waveguide

In this section, we calculate the efficiency for coupling PC waveguides modes to dielectric waveguides. For a benchmark value, we calculate throughput from a PC waveguide to a dielectric waveguide that is terminated flat. The measured transmission is the same, 55%, for two different dielectric waveguide widths $w = 2a$ and $w = 6a$. This result agrees with what we expect from a k-matching argument. Transmission through an interface between two different dielectric materials for normal incidence can be given in terms of the propagation constants k and $\bar{k}$ on the two sides of the interface as

$$T = \frac{4k\bar{k}}{(k+\bar{k})^2} \tag{4.1}$$

At the pulse frequency ω_0, the wavevector in the PC guide is $k = 0.23\ 2\pi/a$ and in the dielectric waveguide with $w = 2a$ it is $\bar{k} = 1.20\ 2\pi/a$. The simple model yields $T = 0.54$, very close to the value obtained from the numerical simulations. The width w of the guide does not change the transmission greatly even when $w = 6a$, because for waveguide widths $w \gg \lambda/2n$ the fundamental mode wavevector k is roughly $k \approx \omega_0 n/c = 1.224\ 2\pi/a$, where $n = 3.4$ is the dielectric constant of the waveguide.

We expect the efficiency of the tapered coupler described in the former section

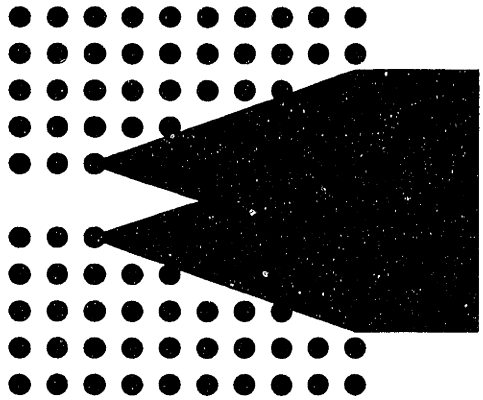

Figure 4-9: Coupler with an outer and an inverse inner taper to couple light out of a photonic crystal waveguide.

to remain fairly high even for coupling out of the PC waveguide because of the time-reversibility of Maxwell's equations. Radiation losses in our simulations are usually under 1%. Nevertheless, since the dielectric waveguides we used are mostly multimode, we do not expect exactly the same transmission efficiency. We measure transmission to a tapered waveguide shown in Fig.4-4 with parameters $w = 6a$, $d = 0$ and $l = 11a$ to be 85%. However, one can improve on this number by using an inverse taper, that is the taper with $l < 0$. This equivalent to "tapering" the air PC waveguide. For the same waveguide width and $d = 7a$, and $l = -10a$, transmission increases to 89%. A smoother type of inverse taper with both an outer and inner taper is shown in Fig.4-9, for which transmission is 94%.

The width of the waveguide w still remains an important parameter. As w decreases, our calculations show that the coupling efficiency drops as well. If we decrease the width of the waveguide in Fig.4-9 to $w = 2a$, ending up with an inverse taper with $l = -4a$, transmission is only 83%. As the output waveguide width decreases, so does the number of modes in the waveguide at the pulse frequency. Since the number of available channels that the mode in the PC waveguide can couple into falls, transmission efficiency decreases as well. In contrast, in the case of coupling into the PC waveguide, a very wide dielectric waveguide has a low efficiency, because in this case there are many channels to which a *reflected* wave from the junction can couple. For example, for a waveguide of width $w = 7a$ the transmission we measure is only

64% even with a large taper length $l = 10a$.

4.5 Summary

In this chapter, we designed tapered couplers for efficient light coupling into and out of photonic crystal waveguides. In the case of coupling into the PC waveguide, we achieved 96% efficiency with a tapered coupler as opposed to 22% for a wide waveguide terminated flat. Coupling light out of the photonic crystal waveguide is best done with an inverse taper. We measured transmission efficiency of 94% compared to 55% with a flat waveguide ending. We also reasoned based on the results of numerical simulations that wide waveguides are better suited for output that input coupling.

Chapter 5

Absorbing boundary conditions for FDTD simulations of photonic crystal waveguides

5.1 Introduction

Photonic crystals, also known as photonic band gap (PBG) materials, can mold the flow of light in a controlled fashion. They are periodic arrays of dielectric materials that open up band gaps for electromagnetic (EM) waves, that is, frequency ranges where photon propagation is forbidden. It has been demonstrated both theoretically [3] and experimentally [24] that line defects introduced into a photonic crystal can guide light within the band gap. PBG waveguides have many advantages over traditional dielectric waveguides. For instance, they can guide light in air [3], not only in dielectric, thus decreasing material losses at optical frequencies. Bends in photonic crystal waveguides can also carry EM waves around sharp bends with high efficiency [19]. Novel optical devices, such as high performance PBG waveguide based channel drop filters have also been designed [18]. The potential use of these materials in integrated photonic circuits has also aroused interest in such waveguides [16].

The finite-difference time-domain (FDTD) method [25] has been widely used to

study EM properties of arbitrary dielectric structures. In this method, one simulates a space of theoretically infinite extent with a finite computational cell. To accomplish this, a number of boundary conditions, such as Berenger's perfectly matched layer (PML) [20], have been proposed that absorb outgoing waves at the computational cell boundaries. Applications of the FDTD method to simulate photonic crystal waveguides, however, poses unique difficulties. While reflection from a PML boundary is minute for a traditional dielectric waveguide, substantial reflection from the boundary is observed if a PBG waveguide is terminated so, on the order of 20-30 % in amplitude [19]. Such reflection introduces unphysical reflected (parasite) pulses which may significantly compromise the accuracy of the simulated response. Reflected waves introduce interference and result in large errors in transmission measurements.

One approach to eliminate errors due to reflected pulses has been to increase the cell size such that the useful and the parasite pulses can be separated [19]. This approach, however, significantly increases the computational cost in terms of memory and time. Special care must be taken to separate well the pulses since due to interference the error is proportional to the amplitude, and not to the power, of the reflected pulse. In addition, in the case of steady state simulations, or when a high-Q resonance is involved, it becomes impractical or even impossible to separate the reflected signal amplitude from the useful one. In this chapter, we demonstrate that it is possible to reduce the reflection amplitude from photonic crystal waveguide ends to a few percent by using a k-matched distributed Bragg reflector (DBR) waveguide.

5.2 Computation of the reflection amplitude

For concreteness, we consider a PBG material that is a two-dimensional photonic crystal, consisting of a square lattice of parallel infinite dielectric rods in air. The lattice constant is a and the rods are assumed to have a circular cross-section of radius $r = 0.2a$. The dielectric is chosen to have refractive index $n = 3.4$, appropriate for Si at the optical communication wavelength $\lambda = 1.55$ μm. This crystal has a complete band gap for TM polarization between frequencies 0.283 and 0.424 $2\pi c/a$. A PBG

waveguide is created by removing one row of dielectric rods from the perfect crystal. The resulting structure remains periodic in the direction of the guide axis. There is a single guided mode inside the band gap above $\omega = 0.305\ 2\pi c/a$ [3].

In order to quantify reflection properties when conventional PML boundary is applied to a PBG waveguide, we carry out numerical simulations of pulse propagation in the PBG waveguide by solving Maxwell's equations in the time domain in a finite-difference scheme. The waveguide is terminated with a PML, which acts as a homogenous absorbing medium, simulating a semi-infinite vacuum (see Fig.5-1). Our computational cell is $52a$ long and $14a$ wide. The waveguide runs along the middle of the cell, at a distance of $6a$ from the edges. Due to the exponential decay of the guided mode, the fields are very small at the cell boundaries parallel to the guide. At one end of the waveguide, a dipole source with a Gaussian time-profile creates a TM polarized pulse that propagates down the guide and undergoes reflection when it reaches the opposite cell boundary. We measure the fields in the middle of the waveguide. The guide is designed long enough that at the cell center there is virtually no overlap between the original pulse and the pulse reflected from the guide end. Fourier transforming the incoming and the reflected pulses, we obtain the reflection amplitude from the waveguide end as a function of frequency. The pulse has a center frequency $\omega = 0.368\ 2\pi c/a$ and covers the frequency range $0.335 - 0.4\ 2\pi c/a$.

The measured reflection coefficient $R(\omega)$ is shown as a function of frequency in Fig.5-2 when the guide is terminated at the boundary with a PML (solid line). Over 20% of the light is reflected from the waveguide end in the frequency range considered. In order to understand the physical origin of this reflection, we estimate $R(\omega)$ in a simple one-dimensional scattering model. We consider reflection from a homogenous planar surface, on one side of which the wavector $k(\omega)$ is given by the dispersion relation of the PBG waveguide, and on the other side the free space dispersion relation holds: $\bar{k}(\omega) = \omega/c$. The reflection amplitude for normal incidence is simply given by:

$$R(\omega) = \frac{\bar{k}(\omega) - k(\omega)}{\bar{k}(\omega) + k(\omega)} \tag{5.1}$$

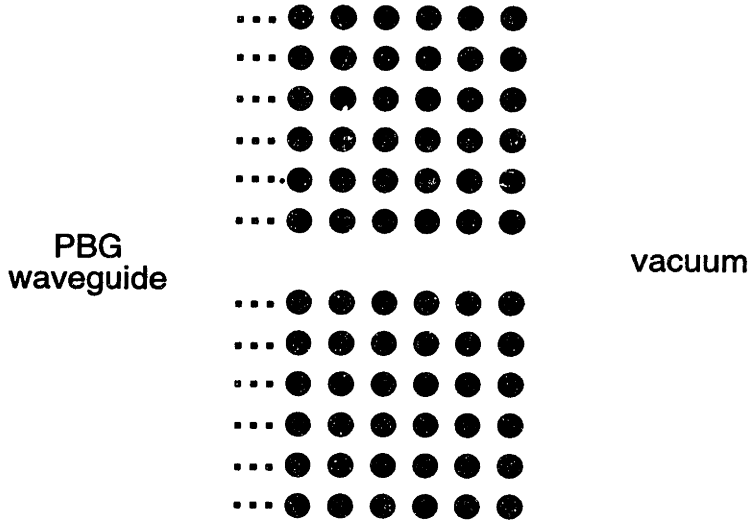

Figure 5-1: A PBG waveguide structure terminated by vacuum.

This is shown by the dashed line on Fig.5-2. There is a good agreement between the model and the numerical experiment, suggesting that the k-mismatch between the PBG waveguide and the surrounding medium plays a crucial role in strong reflection from the guide end. At frequencies below 0.34 $2\pi c/a$, the spreading of the pulse is great and the group velocity is small, so a very long cell would be needed to extract $R(\omega)$. The plot also shows that the agreement between the model and the calculated reflection increases with decreasing k. This is due to the fact that at large wavelengths the details of the photonic crystal are less important.

5.3 Reflection amplitude with new boundary conditions

Since k-mismatch seems to be an important mechanism for reflection, we try to reduce backscattering in the following way. Instead of terminating the PBG waveguide with a PML boundary directly, we terminate it by another waveguide that is k-matched to it, but in which a mode experiences almost no reflection at a PML boundary. A waveguide with a continuous, rather than a discrete, translational symmetry along

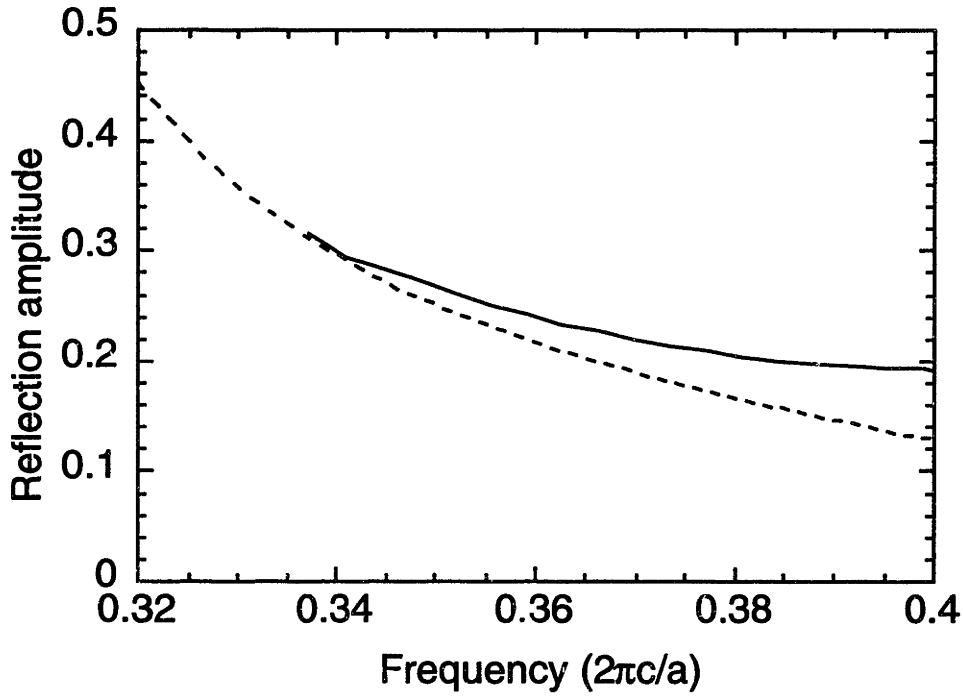

Figure 5-2: The solid line represents reflection from the PBG waveguide end calculated from numerical simulation. The result from the 1D model is shown by the dashed line.

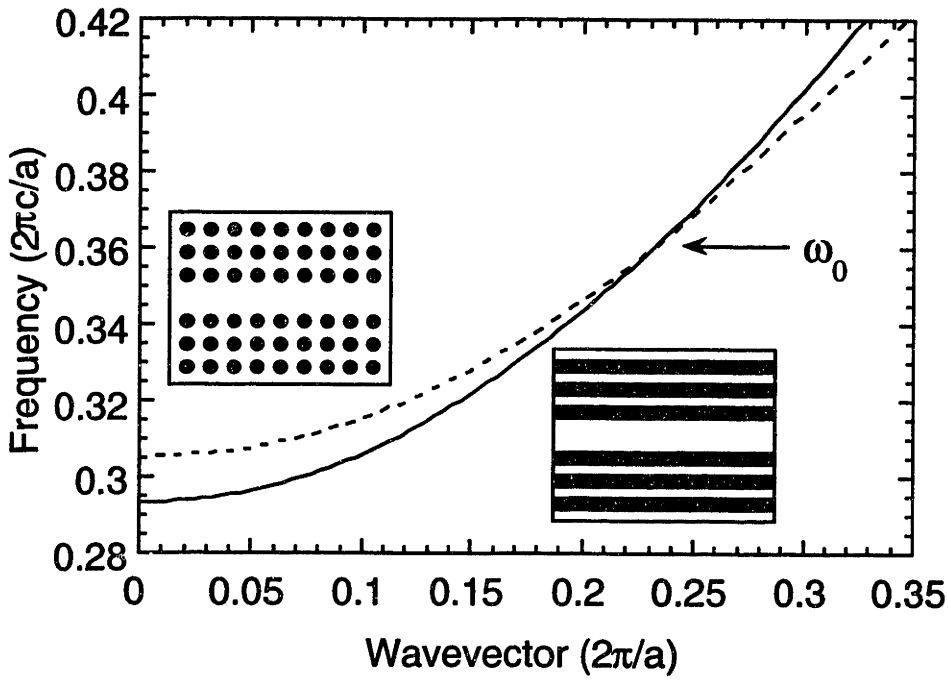

Figure 5-3: Dispersion relations for the DBR waveguide (solid line) and the PBG waveguide (dashed line).

the guide direction satisfies the latter requirement. We also want to attain good profile matching, so we need to preserve the broken periodicity in the perpendicular direction. The simplest such structure is a DBR waveguide comprising two materials. It consists of a periodic array of alternating parallel slabs, with one defect: a single slab with a different thickness. A 2D cross section of a DBR guide is shown on the inset in Fig.5-3. Our numerical simulations show that the reflection amplitude is less than -50 dB across the guided mode spectrum in a DBR waveguide from a PML boundary. In the PBG guide most of the power of the guided mode is concentrated in the air, therefore we consider a DBR guide comprising two materials: air and a dielectric. In our DBR structure, the guide itself is air, so we create the defect in the periodic DBR by increasing the distance between two dielectric slabs.

Next we match the dispersion relations of the two types of waveguides at some frequency ω_0 at which one needs to carry out the simulations. Two parameters, the thickness and the dielectric constant of the dielectric slab, are varied to achieve this. Assuming for concreteness $\omega_0 = 0.36\ 2\pi c/a$, we choose $\epsilon = 10.2$ and $d = 0.25a$,

since both guided modes have the same wavevector at this frequency. The dispersion relations for the two waveguides are shown in Fig.5-3. The guides themselves can be seen on the insets in Fig.5-4, next to the dispersion relation for the PBG waveguide (solid line) and the DBR guide (dashed line).

The inset in Fig.5-4 shows the relative placement of the two types of waveguides. We denote the distance between the beginning of the DBR waveguide and the line defined by the centers of the last row of rods comprising the PBG material by d. This parameter provides us with an extra degree of freedom in our attempt to reduce reflection. The calculated reflection amplitude from a PBG waveguide end terminated by a DBR guide described above is shown in Fig.5-4 for four different values of d. The lowest reflection across the part of the guided mode spectrum shown is when $d = a/2$. In this frequency range there is a large improvement (between three- and fifteenfold reduction) over the reflection from the guide end without the DBR guide, which is also plotted in Fig.5-4 (dashed line).

For comparison purposes, we plot the reflection amplitude calculated from the 1D scattering model for the DBR/PBG waveguide system as the thick solid line in Fig.5-4, using the dispersion relation of the DBR waveguide for $\bar{k}(\omega)$ in equation (5.1). Even though from a k-matching argument we expect that reflection be eliminated at ω_0, it is still about 3% there. This demonstrates that k-matching is important up to a certain extent, but when reflection is on the order of a few percent, other mechanisms become dominant. The residual reflection may be due profile mismatch between the waveguides or to other local phenomena, such as low-Q resonant states at the interface. Because of this, matching curves exactly for all wavevectors is not necessary.

5.4 Summary

In summary, we have designed a flexible way to reduce reflection from PBG waveguide ends to under a few percent. We used a k-matched DBR waveguide to terminate the PBG guide and used the freedom in designing and placing the DBR waveguide to

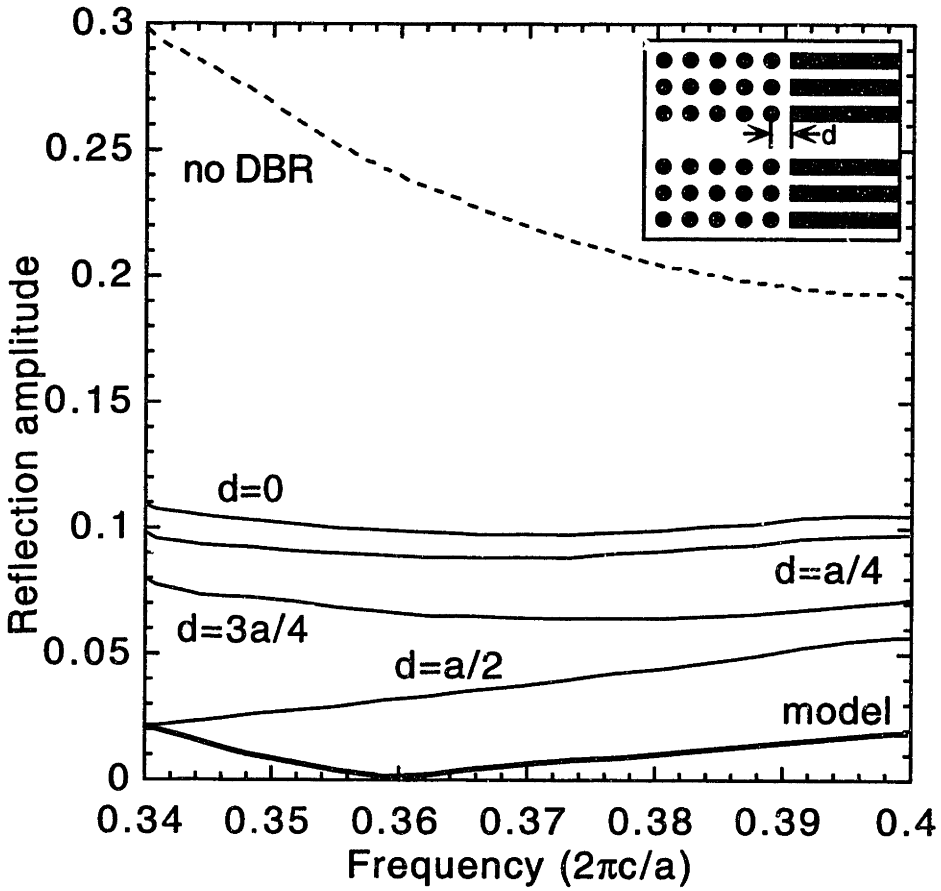

Figure 5-4: Thin solid lines represent the reflection amplitude calculated from the numerical simulation for four different values of the parameter d. The dashed line stands for reflection without the DBR guide, and the results from the 1D model is shown by the thick solid line

reduce reflection. This provides a simple way in reducing the computational costs associated with simulating PBG waveguides.

Chapter 6

Laser action from two-dimensional distributed feedback in photonic crystals

6.1 Introduction

Organic gain media have been very useful in investigating the properties of several classes of laser resonators [27, 28, 29, 30, 31, 32, 3, 33, 34, 35]. The principal reason for this is that, in many cases, it is relatively easy to fabricate lasers with solid-state organic gain media. Thus, organic and polymeric lasers have been used with advantage in pioneering studies of distributed feedback (DFB) [27], distributed Bragg reflector (DBR) [28], whispering-gallery mode [29, 30], and planar microcavity lasers [31]. We have sought to use solid-state organic gain media in the investigation of lasers based upon one- and two-dimensional photonic crystals and microcavities created from such structures. Berggren et al. have reported on the experimental characteristics of organic lasers based on planar resonators formed by a rhomboid lattice of shallow holes [32] In this chapter, we examine the lasing properties of resonators formed by a triangular lattice of shallow holes. We also calculate the dispersion relation for photons in such a structure and compare the measured lasing wavelengths with expected values

based upon the calculations. The structures we employ in this study, while being two dimensional, do not possess a complete two-dimensional band gap. [3] The characteristics of lasers formed with such resonators are, however, important prerequisites for studying the characteristics of lasers formed with a complete two-dimensional band gap.

6.2 Experimental laser spectra

The structure of the lasers we examine in this chapter is illustrated schematically in Fig.6-1. A coating of photoresist on thermally oxidized silicon is patterned to form a triangular lattice of holes. The photolithography was performed with a 248 nm light source and involved advanced techniques to obtain feature sizes below the exposure wavelength. The periodicity of the pattern is 400 nm, and the typical radius of the holes is 100 nm. Shallow holes of typical depth 20-40 nm are etched in the SiO_2 by reactive ion etching through the photoresist mask. The holes are defined in the form of a triangular lattice (Fig.6-1.b to facilitate analysis. The photoresist is then removed and a film of 2-(4-biphenylyl)-5-(4-tertbutylphenyl)-1,3,4-oxadiazole (PBD) doped with about 1% by weight of coumarin 490 and DCM is deposited over the entire structure by spin coating. The thickness of this doped organic layer (150 nm) is such that the planar waveguide that is formed with the organic as the core layer and air and SiO_2 as the cladding layers supports only the lowest order transverse electric (TE) and transverse magnetic (TM) modes.

The structure described above was photoexcited with 337 nm light from a pulsed nitrogen laser (pulse width 52 ns) and the emission spectra measured with a charge coupled device (CCD) detector/spectrometer. The PBD molecules absorb the pump and funnel the excitation to DCM dye molecules through a process called cascade Förster transfer. The gain medium can be approximated by a four-level system [33, 34]. Above a threshold pump power of $\approx 50 kW/cm^2$, laser emission is observed in the wavelength range 580-600 nm and typical spectra are shown in Fig.6-2. For convenience, the spectra are taken away from the plane of the waveguide (i.e., from the

(a)

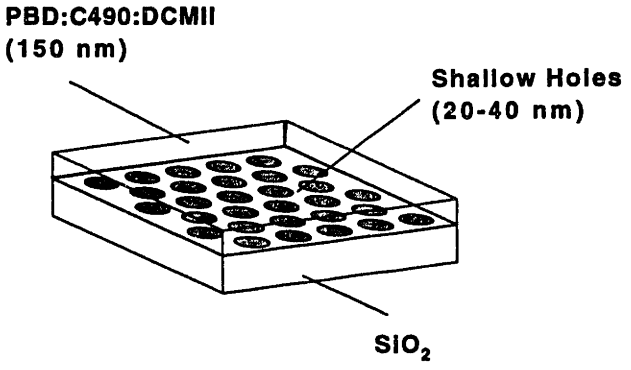

(b)

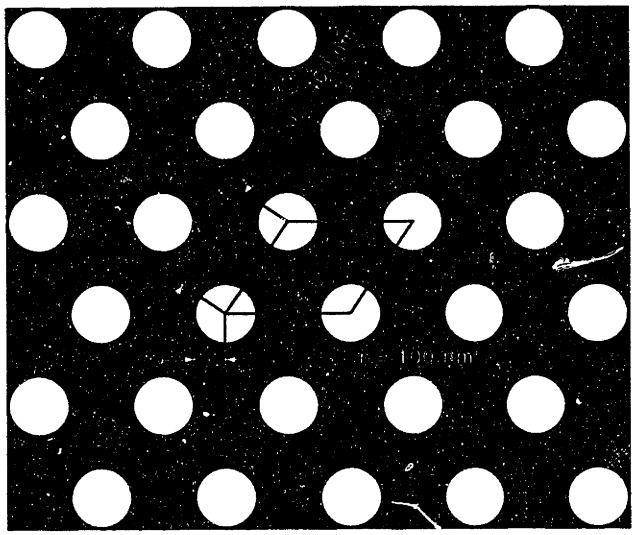

Figure 6-1: a) Schematic layer structure of the lasers employed in the study. b) Details of the two-dimensional triangular lattice.

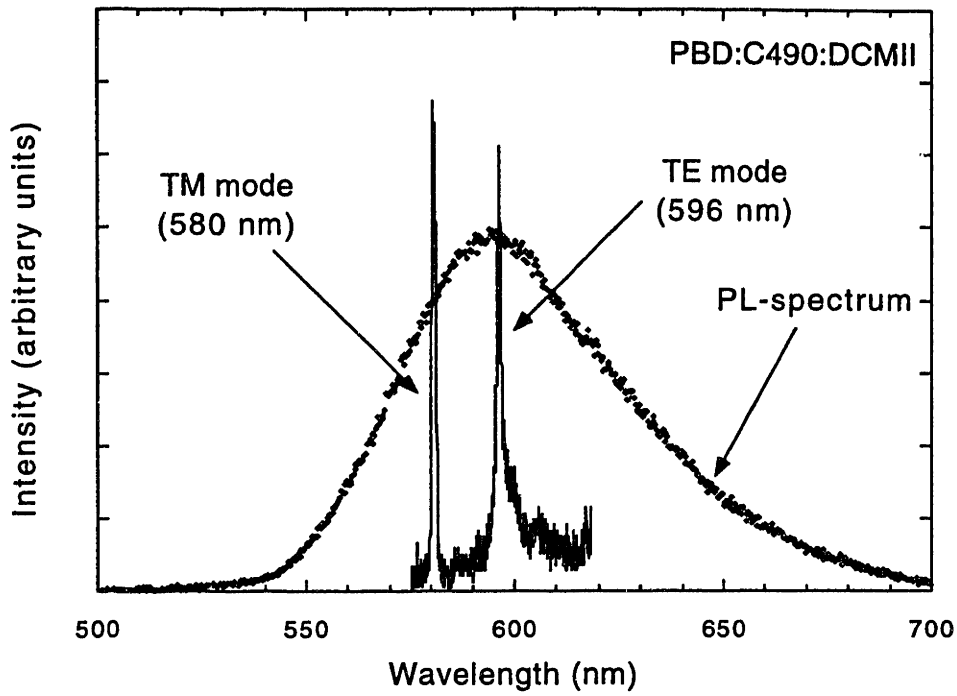

Figure 6-2: Lasers emission spectra from the device shown in Fig.6-1. The two peaks have different polarizations as shown. The spontaneous emission spectrum of the gain medium is also shown with a dashed line.

laser emission diffracted by the grating). The peak at 596 nm has a TE polarization, and the peak at 580 nm has a TM polarization. The threshold pump power for observing laser oscillation is significantly higher than the $\approx$ 1kW/cm^2 reported by us for third order DBR lasers with the same gain medium [33]. This is attributed to the lack of a complete gap, which results in a coupling between the lasing mode and other modes localized in the organic.

6.3 Theoretical analysis of lasing mechanism

In order to attain a deeper understanding of the nature of laser action, we calculate the dispersion relations for the quasi-two-dimensional structure illustrated in Fig.6-1 with the aid of a simple model. In the first approximation, the shallow holes are neglected and we consider a layer of gain medium on top of the unetched SiO_2 substrate. Let the thickness of the gain medium be d, and the dielectric constant of

air, gain and substrate be ϵ_0, ϵ_1, ϵ_2, respectively. We focus our attention on modes that are localized in the middle layer (evanescent both in air and in the substrate) and possess an in-plane wavevector of magnitude k. Matching boundary conditions at the interfaces yields a transcendental equation determining the dispersion relations $\omega(k)$ for the localized modes [35]. The modes can be classified according to their polarization. For TE modes we obtain

$$\tan(d\sqrt{\epsilon_1\omega^2 - k^2}) = \frac{\sqrt{\epsilon_1\omega^2 - k^2}(\sqrt{k^2 - \epsilon_0\omega^2} + \sqrt{k^2 - \epsilon_2\omega^2})}{\epsilon_1\omega^2 - k^2 - \sqrt{k^2 - \epsilon_0\omega^2}\sqrt{k^2 - \epsilon_2\omega^2}} \tag{6.1}$$

and for TM modes:

$$\tan(d\sqrt{\epsilon_1\omega^2 - k^2}) = \frac{\epsilon_1\sqrt{\epsilon_1\omega^2 - k^2}(\epsilon_2\sqrt{k^2 - \epsilon_0\omega^2} + \epsilon_0\sqrt{k^2 - \epsilon_2\omega^2})}{\epsilon_0\epsilon_2(\epsilon_1\omega^2 - k^2) - \epsilon_1^2\sqrt{k^2 - \epsilon_0\omega^2}\sqrt{k^2 - \epsilon_2\omega^2}} \tag{6.2}$$

These equations can be solved numerically. The first order modes have frequency cutoffs, below which no localized modes exist.

We treat the effect of shallow holes on this system as a perturbation. The two-dimensional grating imposes a periodicity on the system, so the bands may be represented in a reduced zone scheme. The resulting photonic band structure is shown in Fig.6-2.a for a triangular lattice with a lattice constant of $a = 400$ nm, $d = 140$ nm, $\epsilon_0 = 1$ for air, $\epsilon_1 = 2.89$ for the organic, and $\epsilon_2 = 2.13$ for the substrate [28]. The reciprocal lattice (which is also triangular) and the first Brillouin zone are shown in Fig.6-3.b. The refractive index variation created by etching shallow holes opens up small band gaps at k points where bands of the same symmetry are degenerate. These gaps are not indicated in Fig.6-3. As a result of coupling between bands, the group velocity of photons may become zero at high symmetry points in the Brillouin zone. At these wave vectors, standing waves form which provide ample feedback necessary for lasing action.

In order to identify the wave vector responsible for laser action in our structure, we look for degenerate bands at high symmetry points in the range of observed lasing wavelengths. This corresponds to the frequency $\omega = 0.666\ 2\pi c/a$, which selects the lowest two bands at the M point. Here both the TE and TM bands have zero gradient

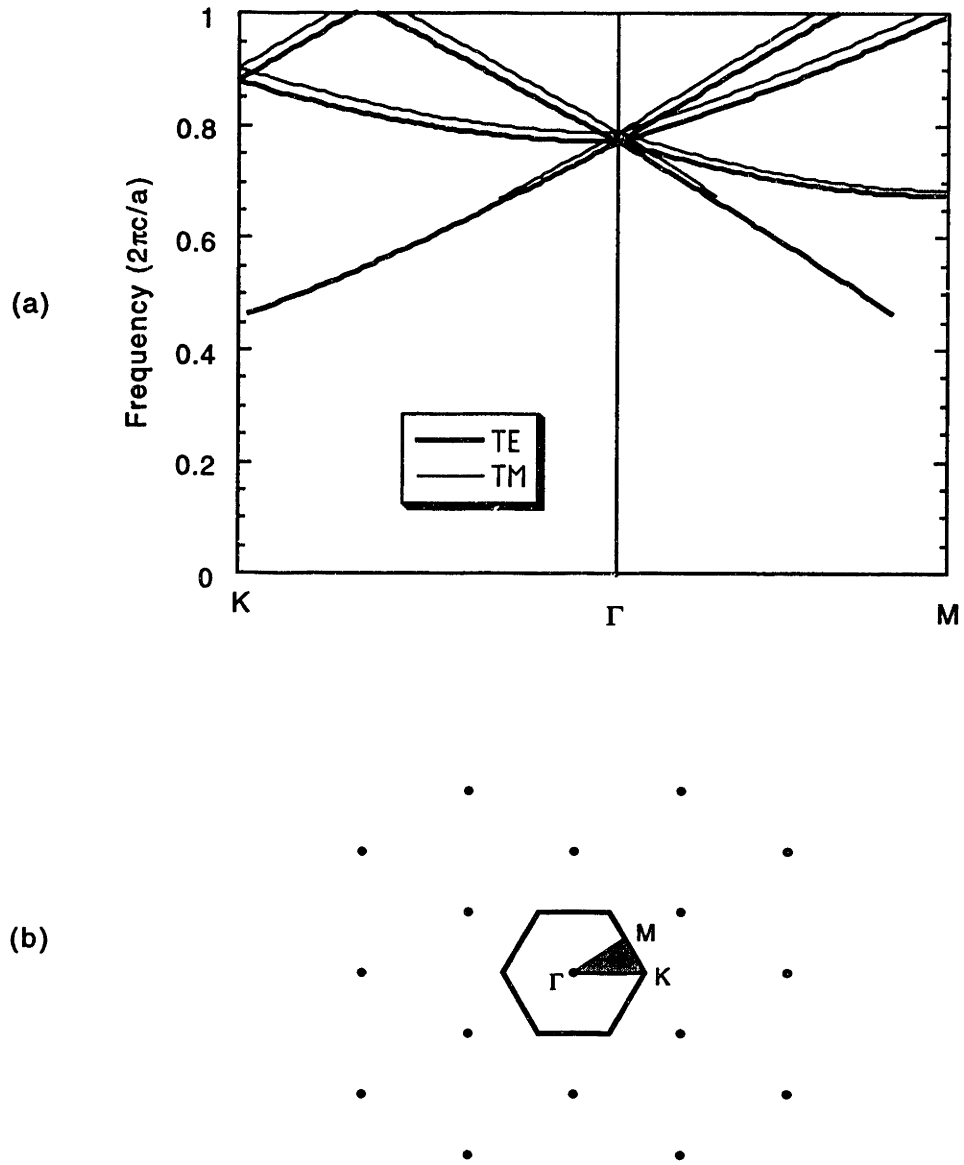

Figure 6-3: (a) Calculated photonic band structure of the device shown in Fig.6-1 for TE and TM polarizations. For TE polarization, the electric field vector is in the plane of the waveguide. (b) The reciprocal lattice and the Brillouin zone showing the high-symmetry points.

when holes are taken into account. We solve equations (6.1) and (6.2) for this wave vector ($k = 2\pi/a$) to obtain wavelengths 584 nm for the TM mode and 594 nm for the TE mode. These are almost exactly the wavelengths in Fig.6-2 where laser action is observed. The small discrepancy is due to the uncertainty in measuring ϵ_1 and d as well as to the frequency shift caused by introducing the shallow holes. The latter effect is relatively small and is estimated to account for no more than a shift of 1–2 nanometers in the lasing wavelength observed.

The basic device structure possesses the potential to be modified to allow for some very interesting technological possibilities. One such modification is the creation of a complete two-dimensional photonic band gap for at least one of the polarizations. Laser action from two-dimensional photonic crystals with a complete band gap has never been reported by any group. Organic gain media, in combination with advanced Si nanofabrication technology, should make this possible as suggested by our theoretical calculations.

6.4 Summary

In summary, we have reported the characteristics of novel lasers with organic thin-film gain media. Laser action arises from two-dimensional distributed feedback from a triangular photonic crystal. The structures reported above do not possess a complete two-dimensional photonic band gap. However, the zero group velocity of photons along some directions of symmetry gives rise to laser oscillations. Dispersion relations for photons were calculated analytically and were used to interpret the laser emission spectra. The calculations predict two peaks of different polarizations at wavelengths in close agreement with experimental data. Our studies also indicate that such structures can be modified to possess a complete two-dimensional band gap.

Chapter 7

Lasing mechanism in two-dimensional photonic crystal lasers

7.1 Introduction

The use of photonic crystals as laser resonators has been advocated because photonic band gap (PBG) materials are able to modify the density of electromagnetic modes and thus enhance or suppress spontaneous emission. The traditional distributed feedback (DFB) laser falls in this category, being characterized by a dielectric constant that is periodic in one dimension (1D) [36, 37]. The feedback necessary for laser action is provided in one spatial direction by the grating. While DFB lasers have low thresholds, an improvement seems possible if spontaneous emission were controlled over the entire plane. This can be achieved by modulating the refractive index in two dimensions (2D). There have been recent reports of laser action from this novel type of laser [38, 39]. However, the small size of the refractive index variation, resulting in a small band gap, did not allow for a comprehensive analysis of the lasing mechanism.

In this chapter we present laser action from a new photonic crystal structure with a larger refractive index variation, which even has the potential of opening a

complete in-plane band gap for optical wavelengths.[1] First, we discuss some aspects of a general theory for laser emission in periodic structures and show that lasing in 2D photonic crystals occurs at saddle points. Next we describe the fabrication procedure for the lasers and present experimental results. Finally we compare our theoretical and computational results with the observed lasing spectra.

7.2 Spontaneous emission in 2D periodic structures

DFB lasers take advantage of optical feedback that is distributed throughout the resonator structure and the gain medium. This feedback is a result of Bragg scattering from a periodic index or gain variation [27]. The operation of 1D DFB lasers can be described in terms of coupled-wave theory [36, 40]. A grating of periodicity a induces coupling between forward and backward propagating waves at Bragg frequencies $\omega_B = N\pi c/a$ (N an integer), which in turn opens up band gaps around ω_B. It can be shown analytically that for small gains, the modes at the band gap edges have the smallest gain threshold for lasing. An intuitive explanation often given is that since modes near the band edge have small group velocities v_g, and can acquire a large gain in a single pass through the laser plane. In fact, in 1D, the gain is proportional to $1/v_g$ [36]. However, in the following we will show that while in a 2D PBG structure the existence of small group velocity modes is still necessary for lasing, it is no longer a sufficient condition.

We now present an argument for 1D periodic structures that can easily be extended to 2D. If the gain medium is not in a free space environment, its spontaneous emission rate and spectral shape will be modified by a factor proportional to the local density of modes [41]. A sharp peak in the density of electromagnetic modes enhances spontaneous emission. This in turn increases gain for modes at that frequency and induces lasing if the gain threshold is reached. In an infinite 1D periodic structure,

[1] Results will be presented elsewhere.

the density of modes $D(\omega)$ has a characteristic Van Hove singularity at band extrema: $D(\omega) \propto [\pm(\omega - \omega_g)]^{-1/2}$, where ω_g is the band gap edge frequency. In a finite structure, this singularity becomes a sharp peak that enhances spontaneous emission by a large factor and allows for low threshold lasing to start. These singularities are directly related to the group velocity as follows:

$$D(\omega) \propto \int dk\, \delta(\omega - \omega(k)) = \left|\frac{d\omega}{dk(\omega)}\right|^{-1} = \frac{1}{v_g(\omega)} \tag{7.1}$$

Nevertheless, in general, the existence of zero group velocity modes does not always imply a peak in the density of states. It is well known that in a 2D periodic structure, $D(\omega)$ does not diverge at the band maxima or minima. At these points the singularity takes the form of a discontinuity. Unlike in 1D, spontaneous emission is not enhanced at band extrema even though the group velocity is zero. In 2D, however, there can be other frequencies where $\nabla\omega(\mathbf{k}) = 0$ but $\omega(\mathbf{k})$ has no extremum: a saddle point. Near a saddle point of frequency ω_s, one finds a logarithmic divergence $D(\omega) \propto -\ln|\omega - \omega_s|$. For a finite structure, this singularity again will show up as a peak in the mode density, facilitating laser action at ω_s. Naturally, whether lasing will occur at a saddle point also depends on the presence of other modes and on the fraction of the spontaneous emission coupling to the lasing mode.

This argument also demonstrates that, contrary to expectations, the lasing threshold will not necessarily be lowered when the refractive index modulation is extended to the entire plane. $D(\omega)$ diverges faster in 1D than in 2D, implying a larger gain margin[2], which generally means a lower lasing threshold.

7.3 Experimental results

In our experiment, a coating of photoresist on thermally oxidized silicon is patterned to form a lattice of holes in all our samples. The photolithography is performed with

[2]Gain margin is the difference in gain of the lasing mode over the gain of the closest non-lasing mode.

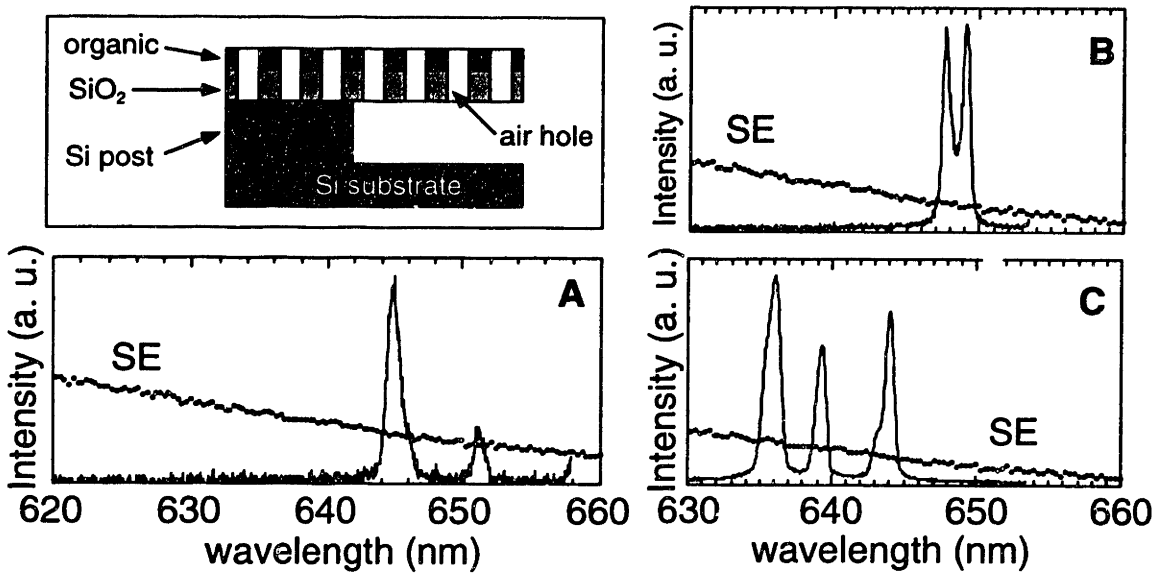

Figure 7-1: Upper left panel: vertical cross section of the laser. Graphs: Observed spectra for structures A, B and C. The circles indicate to the spontaneous emission spectrum of the gain medium.

a 248 nm light source. Holes are etched all the way through the SiO_2 to reach the Si substrate by reactive ion etching through the photoresist mask. The photoresist is then removed and some of the Si substrate is etched away, leaving only a square lattice of posts to support the SiO_2 slab. The supporting posts have a height of 0.8-1.0 μm, radii of 15 μm and they are spaced about 100 μm apart. Next a film of 8-(hydroxyquinolinato) aluminum (Alq) doped with about 1% by weight of DCM (a commercially available dye) is deposited over the entire structure by sublimation. The doped organic layer and the SiO_2 form the core layers of a planar waveguide (see Fig.7-1). The air cladding layers provide good mode confinement.

This structure is photoexcited with 337 nm light from a pulsed nitrogen laser with a pulse width of 2 ns and the emission spectra measured with a CCD detector/spectrometer. The Alq molecules absorb the pump and funnel the excitation to DCM dye molecules through a process of Förster transfer [43]. Above a threshold pump power of ≈ 50 kW/cm^2, laser emission is observed. The linewidth of the emission spectrum narrows from 80-100 nm to about 1 nm and emission becomes highly directional. The threshold is higher than the 5-10 kW/cm^2 for the same gain medium

in 1D DFB lasers of similar sizes using the same excitation methods, as it can be expected from our argument on thresholds. For convenience, the spectra are taken from the laser emission diffracted by the grating away from the plane of the waveguide. In Fig.7-1, we show lasing spectra obtained from three structures labeled A, B, and C. In all of them the thickness of the SiO_2 is 680 nm, and the thickness of the sublimed organic is 250-300 nm. Structures A and B have holes in a triangular lattice, and structure C in a honeycomb lattice. The lattice constants a and the hole radii r are $a_A = 470$ nm, $r_A = 130$ nm, $a_B = 670$ nm, $r_B = 130$ nm, $a_C = 800$ nm and $r_C = 120$ nm. Two peaks of different polarizations are observed for A and B. Spectra for C show three peaks; however, the shoulder in the line at 644 nm indicates two lasing modes that cannot be resolved at our spectral measurement resolution.

7.4 Theoretical prediction of lasing wavelengths

In the following we calculate the lasing frequencies for the above structures. We assume that the posts do not have an influence on lasing. They effectively act as sinks for modes localized in the slab near them, due to the high index of silicon. The lasing modes must be contained in regions away from the posts, where the structure just consists of a slab made of SiO_2 (thickness d_1, refractive index n_1) and the doped organic (thickness d_2, index n_2). The slab has holes through it in a periodic manner and the structure is surrounded by air on either side. In our calculations we took $n_1 = 1.46$, $n_2 = 1.7$, $d_1 = 680$ nm, and $d_2 = 270$ nm.

We compute the lasing mode frequencies for this slab structure using the plane-wave expansion method [7]. However, to gain a good physical understanding of the origin of the bands as well as to reduce computational requirements, we do not conduct a full band structure calculation for the 3D system. Our approach is to use a 2D calculation to find the k-points at which saddle points occur, then do a 3D calculation only for those k-points. This approach is justified by results of our computations of slab localized modes. They reveal that these modes have an in-plane field distribution like the corresponding modes in a 2D photonic crystal that is infinite and uniform in

the z-direction. The 3D modes in addition have vertical profiles like modes in a 1D uniform slab without holes. This suggests a method for estimating the position of saddle points in (ω, k)-space by combining the results of the 1D and the 2D calculation as follows. The qualitative features of the bands are obtained from calculating a 2D PBG band structure. This allows us to determine the saddle point positions in k-space. Furthermore, we can obtain quantitative estimates for the mode frequencies using a 1D uniform slab model for the structure [38]. Finally, having identified the lasing modes in this way, we determine their frequencies exactly in a 3D calculation.

First we compute the band structure of a 2D photonic crystal consisting of air holes in a dielectric with an index n_0. This index is chosen to be $n_0 = 1.5$, close to the average index for our structures. The exact value of n_0 is not important, because we only use these results for qualitative purposes. The band structure for a triangular lattice is shown in Fig.7-2. We can easily identify saddle points at the point M. Because the index contrast is still relatively small, the bands resemble the free space mode $\omega = ck/n_{av}$ folded back into the first Brillouin zone, where $n_{av} = n_0 - 2\pi(n_0 - 1)(r/a)^2/\sqrt{3}$ is the average index of the crystal. Of course, in the 3D band structure, it is the uniform slab modes that are folded back and this is what we consider next.

We calculate dispersion relations for a slab with no holes. We take the average index approximation to both the SiO_2 and the organic slab sections separately to obtain the average dielectric constants ϵ_1 and ϵ_2. In this system, modes can be classified according to their polarization. Matching boundary conditions at interfaces yields the equations that determine the dispersion relations of TE and TM polarized waveguided modes:

$$\frac{k_1^2 - \kappa_0^2}{2k_1\kappa_0}\tan(k_1 d_1) + \frac{k_2^2 - \kappa_0^2}{2k_2\kappa_0}\tan(k_2 d_2) = 1 - \frac{k_1^2 + k_2^2}{2k_1 k_2}\tan(k_1 d_1)\tan(k_2 d_2) \tag{7.2}$$

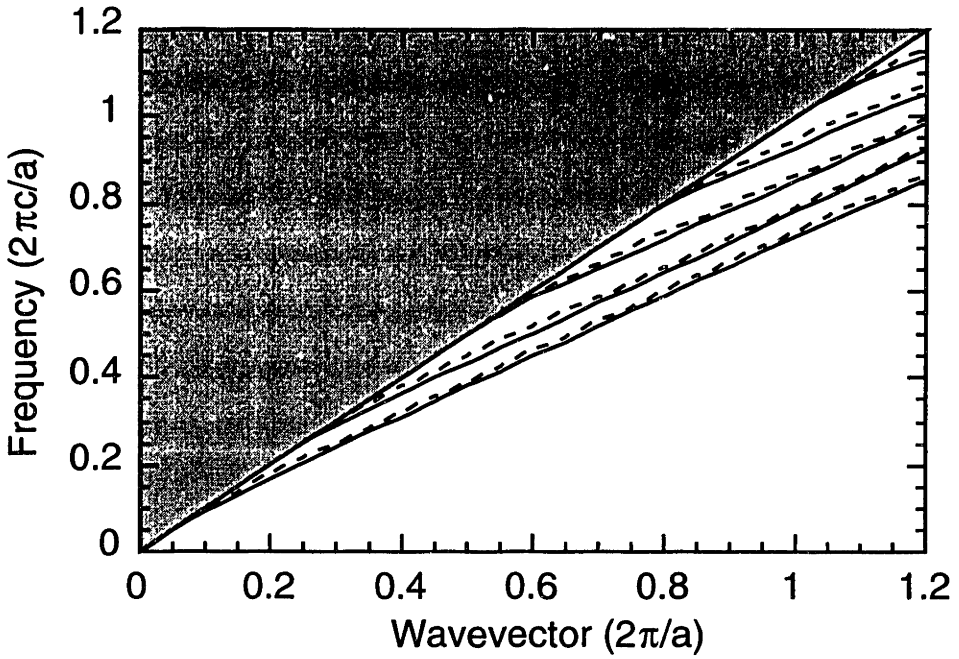

Figure 7-2: Band structure for a 2D triangular lattice of air holes in dielectric of index $n_0 = 1.5$. The lattice constant is a and the radius of the holes is $r_A = 0.277a$. Solid/dashed lines correspond to TE/TM polarized modes.

$$\frac{\epsilon_0^2 k_1^2 - \epsilon_1^2 \kappa_0^2}{2\epsilon_0 \epsilon_1 k_1 \kappa_0} \tan(k_1 d_1) + \frac{\epsilon_0^2 k_2^2 - \epsilon_2^2 \kappa_0^2}{2\epsilon_0 \epsilon_2 k_2 \kappa_0} \tan(k_2 d_2) = 1 - \frac{\epsilon_2^2 k_1^2 + \epsilon_1^2 k_2^2}{2\epsilon_1 \epsilon_2 k_1 k_2} \tan(k_1 d_1) \tan(k_2 d_2) \tag{7.3}$$

where $\kappa_0 = \sqrt{k^2 - \omega^2}$, $k_1 = \sqrt{\epsilon_1 \omega^2 - k^2}$ and $k_2 = \sqrt{\epsilon_2 \omega^2 - k^2}$. These transcendental equations are solved numerically. Dispersion relations obtained for structure A are shown in Fig.7-3. The gray area is the light cone for air, and the solid/dashed lines correspond to TE/TM modes. Bands for one polarization represent modes with different number of nodes in the vertical direction. The refractive index contrast created by the holes folds each of these bands back into the first Brillouin zone and they split in the same manner as the bands in Fig.7-2. Modes can no longer be classified exactly according to their polarization, but they do retain their TE/TM-like characters. In interpreting the 3D band structure, one must also recall that all modes that fall above the light line $\omega = ck$ are not true localized modes but high-Q resonances since they can couple to free space modes [42].

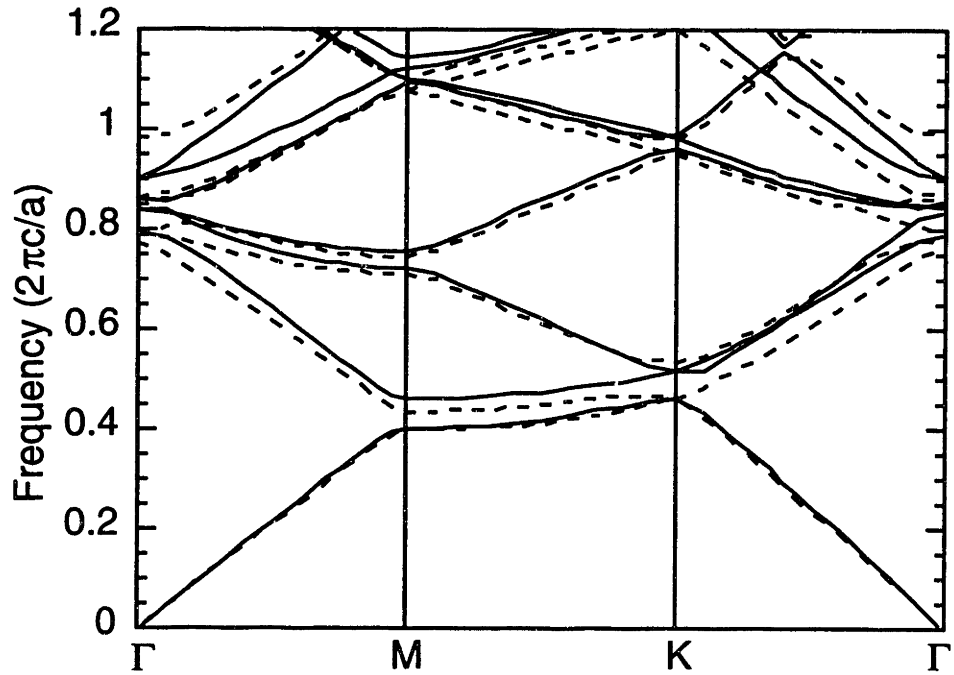

Figure 7-3: Dispersion relations for a slab waveguide of SiO_2 and organic gain medium, with air cladding layers. Thicknesses and average indices correspond to structure A. In the gray shaded area no guided modes exist. Solid/dashed lines correspond to TE/TM polarized modes.

To identify lasing frequencies for structure A, we begin with the results of the 1D calculation. The frequency where lasing is observed corresponds to $\omega \approx 0.73\ 2\pi c/a$ in Fig.7-3. This selects the lowest TE and TM bands at wavevector $k = 2\pi/a$. This wavevector in turn corresponds to the third and fourth bands at the M point in Fig.7-2. The third band has a saddle point at M, as expected. Hence a full three-dimensional calculation of bands is only necessary for a single k-point (M) to obtain the exact lasing frequencies.

Numerical results for structure A substantiate our argument that lasing occurs at saddle points. Saddle point wavelengths are calculated to be 659/654 nm for TE/TM-like polarizations, in good agreement with measured wavelengths (651/645 nm). The positions of the band minima are 626/623 nm. Even though free space spontaneous emission is greater at band minima, lasing is induced at saddle points. The difference between calculated and observed frequencies is due to the uncertainty in measuring

the thickness and the refractive index of the organic medium, and to the inaccuracy of the numerical calculation. (These effects amount to a few percent.) The relative position of the two peaks also gives evidence that lasing occurs at the saddle points.

Structure B lasing frequencies correspond to $k = \sqrt{7/3}\, 2\pi/a$, or, the fifth through eighth bands in Fig.7-2. For each polarization we find two almost degenerate saddle points (sixth and seventh bands). Calculated wavelengths are (646,647)/(644,644) for TE/TM in good agreement with observations (649/648 nm). We fail to observe two lines for each polarization either because they cannot be resolved or because one mode has a much lower gain threshold than the other.

Our calculations show four lasing lines for structure C at 620, 624, 628 and 628 nm, again in good agreement with observation (636,639 and 644 nm, two peaks at the latter wavelength). The relative position of the peaks agree very well with measured wavelengths. We note that while the lasing modes in structures A and B are fundamental slab waveguide modes, in structure C they are second and third order modes with nodes in the direction perpendicular to the slab. They correspond to the sixth, seventh and ninth bands at M.

We also examined the effect of changing parameters on the lasing spectra. The results are in excellent agreement with theory. For instance, changing a_B to 660 nm shifts the entire lasing spectrum down by $\approx$ 10 nm. This is what we expect, since the wavelengths should be proportional to the lattice constant. Altering the radius of the holes affects both the wavelength of the peaks as well as their relative positions. For example, increasing r_C to 140 nm yields a shift in the spectrum: measured peaks are at 611,618 and 623 nm, whereas calculated peaks at 602, 607, 613 and 614 nm. While there is a small discrepancy between calculated and observed lasing wavelengths that is within error limits, the relative peak positions match very well.

In conclusion, we have fabricated a new photonic crystal slab laser with feedback in 2D. Experimental observations agree well with theoretical arguments and numerical calculations, showing that lasing occurs at saddle points of the band structure. We also observe spectra that cannot be obtained from traditional DFB lasers: these lasing lines originate from several saddle points that exist within a small frequency range.

Chapter 8

A photonic crystal defect laser with organic gain media

8.1 Introduction

Lasers comprise a resonant cavity, or some other feedback mechanism, that facilitates population inversion and coherent laser emission by enhancing spontaneous emission at the cavity mode frequencies. Photonic band gap (PBG) materials have been proposed to control spontaneous emission as early as they were first imagined [1, 44, 45]. They can be used to create cavities with high quality factors (Q) in which light is trapped for many cycles before escape. If the cavity contains a material with gain, then spontaneous emission is enhanced on or near resonance by the Purcell factor [46]

$$\eta = \frac{Q}{4\pi V}\left(\frac{c}{n\nu}\right)^2 \tag{8.1}$$

where V is the modal volume of the lasing mode, ν is the optical transition frequency, and n is the refractive index of the material inside the cavity. The enhancement factor will be large if the cavity Q is high and the modal volume is on the order of the wavelength, that is, for strong photon confinement.

Traditionally, mirrors or other reflecting surfaces have been used to create laser cavities. PBG materials offer novel ways of fabricating a high-Q cavity. In a photonic

crystal with a complete three-dimensional (3D) band gap, a defect inside the bulk crystal can support a defect mode that is confined within a volume on the order of the wavelength. According to equation (8.1), in the presence of material gain this high-Q mode would become a low-threshold lasing mode. Nevertheless, 3D photonic crystals are difficult to fabricate at optical wavelengths [47, 48]. One alternative amenable to fabrication is to use index guiding to confine light in two of the spatial directions and periodicity in the remaining direction. Examples of such structure are the strip-waveguide microcavity [42] and the air-bridge microcavity [49]. Since a defect mode in these structures is index-guided in two directions, it can couple to radiation modes, which limits its quality factor Q. Confining light by using PBG effects in two of the dimensions and index confinement in the remaining one reduces radiation coupling while we still retain ease of manufacturability. Such periodically patterned dielectric slab waveguides are termed photonic crystal slabs. They are similar to two-dimensional (2D) photonic crystals in that the refractive index variation is periodic in-plane, but they have a finite extent in the direction perpendicular to the plane of periodicity. In this chapter we discuss the feasibility of lasers based on defects in photonic crystal slabs.

The other basic component in a laser is a gain medium that supplies the photons necessary for laser emission. Semiconductor lasers in integrated optics usually rely on quantum wells as a source of optical gain. Because of the high dielectric constant of the materials used (InP, InGaAsP), quantum-well structures seem ideal candidates for fabricating photonic crystals with large band gaps. However, since non-radiative surface recombination of electrons and holes is an important loss mechanism in semiconductors lasers, PBG materials fabricated by etching air holes into such structures may have high thresholds due to large combined surface areas.

In contrast, in organic materials, like those used in dye lasers, surface recombination does not contribute to losses so they are better suited as gain media for PBG-based lasers. In a mixture of host and guest dyes with radiative Förster transfer [43], the absorption band is displaced away from the emission wavelength, which has the effect of further decreasing absorption losses. Furthermore, organic dyes are

inexpensive and they can be easily sublimed or deposited by spin-coating on an etched substrate. In this chapter, we propose the use of organic gain media to fabricate a PBG defect laser. One major disadvantage of these materials is the relatively low refractive index of organic dyes. The low index poses difficulties in creating a complete in-plane band gap for the PBG material, and overcoming this limitation is a main focus of this chapter.

In the following section we briefly discuss some properties of photonic crystal slabs. Next, in section 3, we design a photonic crystal slab with an organic gain medium that has an in-plane pseudo-gap and investigate the effects on the band gap of the different parameters involved. In section 4, we use numerical simulations to find the defect mode frequency and quality factor and discuss the mechanisms for power loss from the lasing mode.

8.2 Photonic crystal slabs

8.2.1 Band structure

Photonic crystal slabs are structures that are periodic in two dimensions, but do not extend indefinitely in the third dimension like 2D photonic crystals. The slabs have a finite thickness, usually on the order of the wavelength of the guided light. Fig.8-1 shows the band structure of a slab photonic crystal on an SiO_2 substrate. The slab consists of triangular lattice of posts of SiO_2 , spin-coated with chalcogenide (refractive index 2.3), as shown schematically in the inset.

The band structure can be understood physically by distinguishing features due to the 2D refractive index periodicity as well as features due to confinement in the vertical direction. There is index variation in the horizontal plane, so the bands are similar to 2D photonic crystal bands. The finite extent of the photonic crystal in the vertical direction means that in addition to the guided modes, there are also radiation modes present above the light cone, shown in gray in Fig.8-1. As guided mode bands cross over into the light cone, they becomes resonances because they can couple to

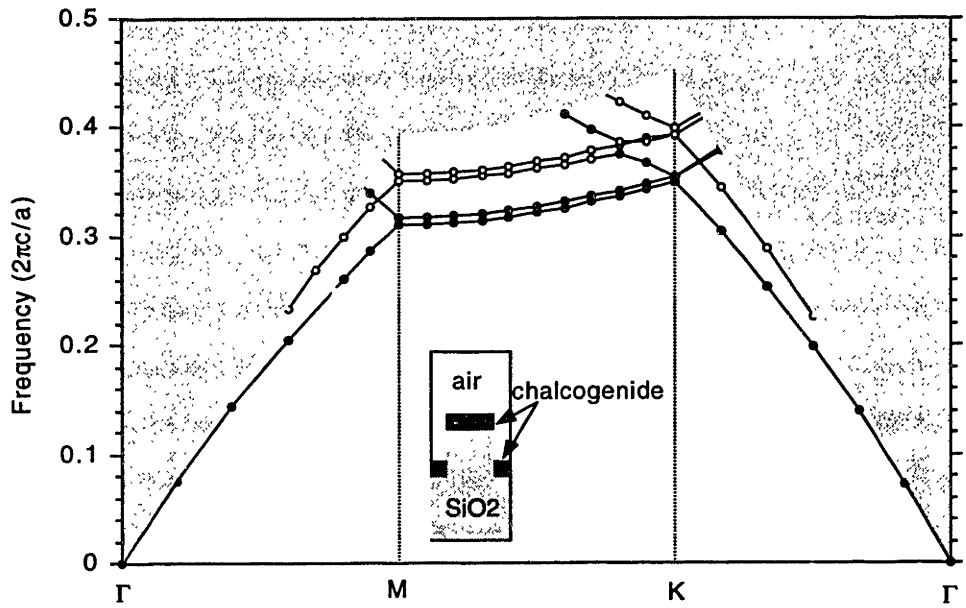

Figure 8-1: Band structure of a photonic crystal slab with lattice constant a. The radius of the holes is $0.35a$, the height of the posts $0.6a$ and the thickness of the chalcogenide is $0.2a$. The gray area stands for the radiation modes and TE/TM-like modes are indicated by filled/empty circles.

radiation modes. Some of the higher bands have no counterpart in the 2D photonic crystal band structure. These modes have nodal planes parallel to the slab surface, and their bands can be obtained by folding back bands of higher order guided modes of the uniform slab. For the particular structure on Fig.8-1, such modes are in the radiation cone.

8.2.2 Polarization and symmetry classification of the bands

In the case of the 2D photonic crystal and a uniform dielectric slab, the guided modes can be classified according to their polarization. As the terminology used is different in the two cases, we schematically show in Fig.8-2 the electric and magnetic fields for a TM-polarized mode in three different materials: a uniform medium, a 2D PBG material and a uniform slab. In a uniform medium both fields are perpendicular to the direction of propagation $\hat{y}$. In a 2D photonic crystal, the magnetic field has a component in the y-direction, and in the case of vertical confinement the electric field

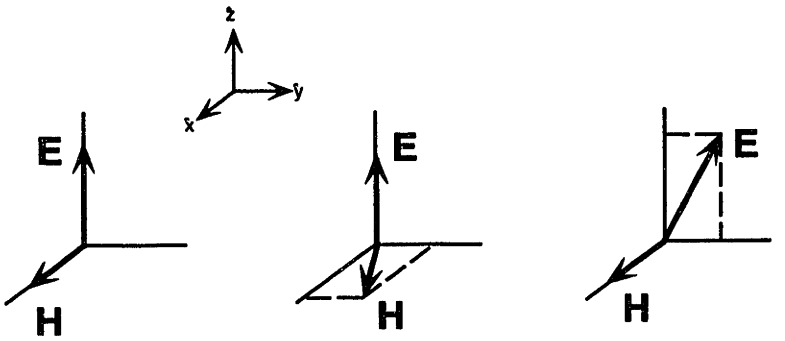

Figure 8-2: Schematic of electric and magnetic fields in a) a plane wave in a uniform medium b) TM mode in a 2D photonic crystal c) TM mode in a uniform slab. The waves are propagating in the $\hat{x}$ direction.

has an y-component, whereas the magnetic field remains perpendicular to $\hat{y}$. We note that in the 2D photonic crystal, the direction and magnitude of the magnetic field varies as a function of position.

For a photonic crystal slab, with both 2D periodicity and vertical confinement, we cannot exactly classify the modes according to their polarization. However, the lowest modes do retain their TE/TM polarized characteristics. The classification is based on the relative magnitude of the z-component of the electric/magnetic fields to their respective in-plane components. In a TE/TM-like mode most of the magnetic/electric field power is in the z-component. If the photonic crystal slab has a plane of symmetry parallel to the slab surface, then modes can be classified according to their even/odd symmetry with respect to the symmetry plane [50]. In this case even modes correspond to TE-like modes with an even number of nodes in the z-direction and to TM-like modes with an odd number of nodes in the z-direction. As an example, in Fig.8-1, filled/empty circles denote TE/TM-like modes. Since these modes have no nodes in the vertical direction, TE/TM-like modes also correspond to modes that are approximately even/odd. As the slab under consideration does not have reflection symmetry, bands change their character as the wavevector changes, as it is the case for the third band between M and K points. Away from band crossing the lowest bands do retain their TE/TM-like characteristics.

This polarization, or approximate symmetry, classification of the bands allows

us to create in-plane pseudo-gaps[1] even in photonic crystal slabs that do not have reflection symmetry in the vertical direction. In this chapter, we consider the lowest order band gap for even TE-like modes. If the slab we use has a plane of symmetry, a complete gap can be achieved. If there is no such exact but only approximate symmetry, then we have only a pseudo-gap. TE-like defect modes in this gap are able to couple to guided modes that are even TM-like or odd TE-like. However, as long as the symmetry is not strongly broken, coupling to these modes will not have a major effect on the defect mode Q. We quantify this claim in section 5.

8.3 Design and optimization of the band gap

We want to able to fabricate a photonic crystal slab by combining materials conventionally used in integrated circuits and organic dyes. Because the organic material is deposited on the top surface and it will consitute the thin waveguide in which light is confined, the substrate must have a lower index than the gain medium. In this section, we consider a structure that is fabricated using a thermally oxidized SiO_2 substrate on top of a silicon wafer. Since the SiO_2 has a lower refractive index than the organic material, if the latter is deposited on it, light will be mostly guided in the organic medium. Furthermore, the upper SiO_2 layer can be patterned using conventional lithographic methods to create periodicity in two dimensions.

8.3.1 General design considerations

The low refractive index of organic dyes used for gain ($n = 1.7$) poses several obstacles to designing a photonic crystal slab with a complete in-plane band gap. If the waveguide containing the organic material is patterned, for example, with air holes, to achieve a band gap, then the effective index of this waveguide is lowered. The drawback of this is that the resulting effective index quickly approaches the index of the SiO_2 substrate ($n = 1.46$) as the holes get large or deep, and the band gap disappears

[1] A frequency range in which the density of states is very low.

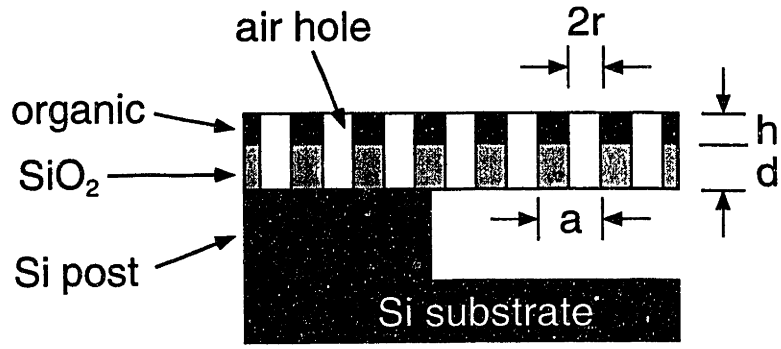

Figure 8-3: Vertical cross-section of the photonic crystal slab structure proposed. The parameters are the lattice constant a, the hole radius r, and the thicknesses of the SiO_2 and organic layers (d and h, respectively).

into the continuum of substrate modes. One way to overcome this limitation is to boost the effective index by placing the organic material on a high index waveguide. However, this would distort the mode profile resulting in a small confinement factor. Only a small portion of the mode power would be in the region with gain medium and overall gain would be reduced.

A more efficient solution is to eliminate the SiO_2 substrate altogether and replace it with air. In practice this can be done by selectively etching away the upper layer of the Si substrate after the holes are etched through a thin SiO_2 layer, leaving posts of Si to support the resulting tabletop-like structure. When the organic material is sublimed on the top of the structure, it covers the SiO_2 layer and falls through the holes. A cross-section of the resulting system is shown in Fig.8-2 in the vicinity of a Si post. It is a waveguide consisting of the SiO_2 and the gain medium, with air cladding layers on both sides. Our ultimate goal is the design of a defect laser, so the posts will not influence the lasing action as long as they are far away from the localized defect mode.

The index contrast between the patterned waveguide in Fig.8-2 and air is small, so only the first order gap is below the light cone. Since this lowest gap is between the dielectric and the air bands [3], the gap will be largest if the first Brillouin zone is close to circular. For this reason we use a triangular lattice. A range for the lattice constant is determined by the requirement that the wavelength of the radiation, which is in the

visible, be in the first gap. For a triangular lattice, the first gap is between the first band at K (at wavevector $k_K = 4\pi/3a$) and the second band at M ($k_M = 2\pi/\sqrt{3}a$). We can approximate the midgap frequency using the effective index of the mode n_{eff} as $\omega \approx c(k_M + k_K)/2n_{eff}$, which gives $a \approx 0.622\lambda/n_{eff}$. The value of n_{eff} can be estimated from a slab obtained by averaging the refractive index of the waveguide with holes. With hole radius $r = 0.35a$ and an average material index 1.6, we get an average index for the slab that is of 1.33. This yields an effective index of roughly $n_{eff} = 1.2$. Therefore for lasing wavelength in the red, one must use a lattice constant of about 350 nm, which is achievable with lithographic methods.

8.3.2 Effect of the parameters on the band gap

A triangular lattice consisting of air holes in a dielectric material permits a TE band gap in a 2D photonic crystal. Therefore we expect that we find a TE-like pseudogap in our configuration. The parameters that can be varied in our structure to tune the band gap are shown in Fig.8-3. They are the thickness of the organic layer h, the thickness of the supporting SiO_2 layer d, and the radius of the holes r. The thickness d is limited from below by the strength of the layer to hold up under its own weight; an about 250 nm thick SiO_2 layer is very stable. The thickness of the organic layer is limited from above, because during deposition an organic layer thicker than the hole diameter can fill up the air holes etched into the SiO_2 . The parameter h should be as large as possible in this range, for two reasons. On the one hand, a thicker organic layer increases the mode confinement factor, that is, the portion of the mode power in the gain medium. On the other hand, the higher the index of the material in the slab, the larger the index contrast between the air holes and the slab. Therefore more of a higher index material in the slab means a larger photonic band gap, giving us more flexibility to design the defect.

We discuss the effects of the parameters on the photonic pseudo-gap using two representative plots. Fig.8-4.a shows the gap as a function of the hole radius r for $d = 0.8a$ and $h = 0.2a$. The solid lines denote the top and bottom of the gap and the dashed line is the gap/midgap ratio in percentage. The largest gap is about 1.4%,

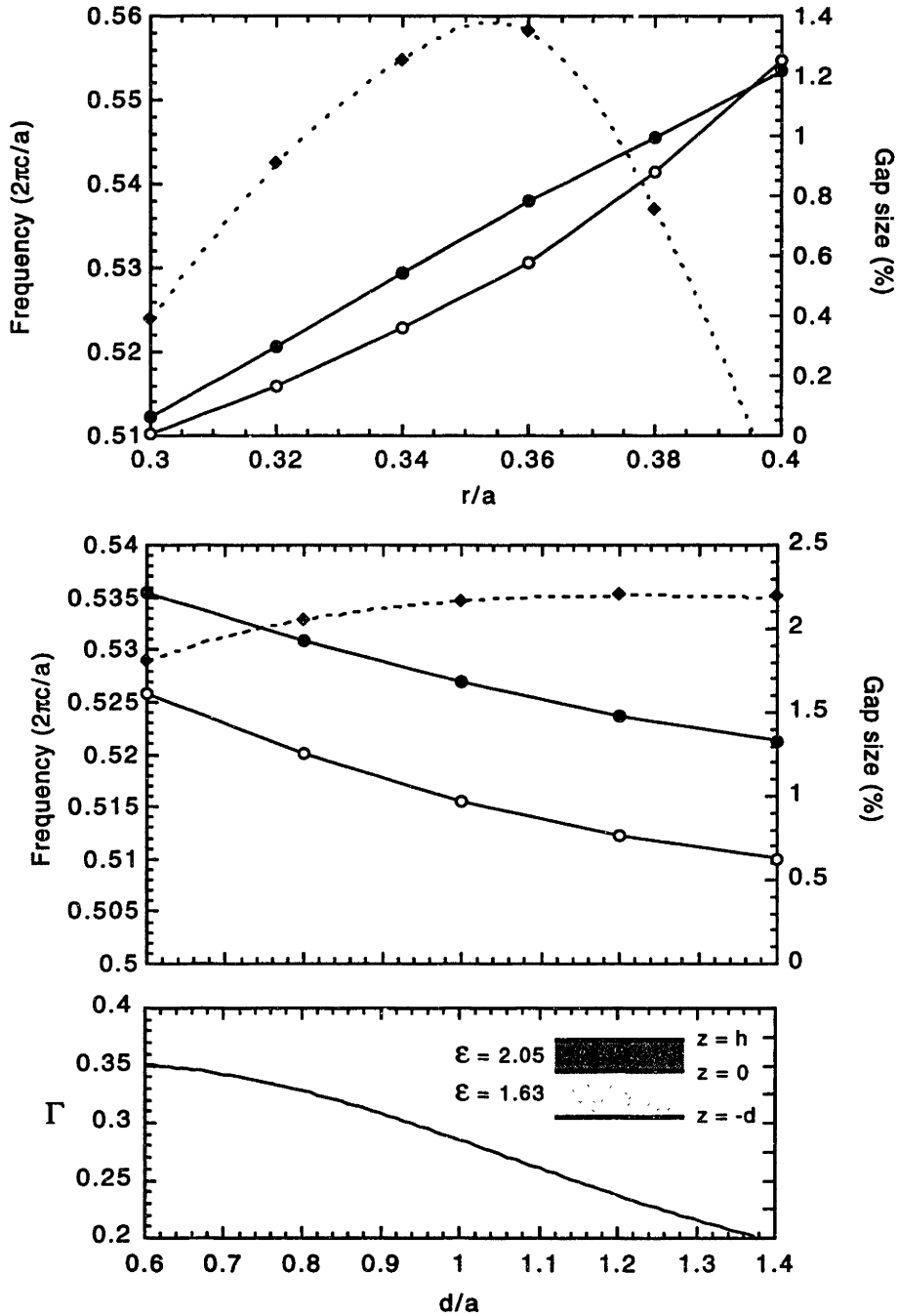

Figure 8-4: The TE-like pseudo-gap and the relative gap size as a function of a) the hole radius for $d = 0.8a$ and $h = 0.2a$ b) the thickness of the SiO_2 layer for $r = 0.36$ and $h = 0.3a$. Solid lines denote the extent of the in-plane gap; full circles stand for the air band at M and open circles for the dielectric band at K. The dashed line is an interpolated curve for the gap size (diamonds).

at $r = 0.355a$. Fig.8-4.b shows the gap as a function of the thickness of the SiO_2 layer d for $r = 0.36a$ and $h = 0.3a$. The notation is the same as on Fig.8-4.a. As d increases, the midgap frequency decreases as well (just like it would in the case of a uniform slab), and the gap size increases. In comparing the plots with different values of h, it is apparent that at $r = 0.36a$ and $d = 0.8a$, a 50% increase in h results in a similar increase in the size of the complete gap. As we expected, the thickness of the higher index organic is therefore a crucial parameter. In fact, without the organic material, the index contrast between air and SiO_2 is too small for a lager than marginal complete gap to open up.[2]

Finally, in Fig.8-4.c we plot an estimate for the confinement factor Γ vs. d for the structure with $r = 0.36a$ and $h = 0.3a$. We calculate the ratio

$$\Gamma = \frac{\int_0^h dz|\mathbf{E}(z)|^2}{\int_{-\infty}^{\infty} dz|\mathbf{E}(z)|^2} \tag{8.2}$$

for the two-layer slab with spatially averaged dielectric constants shown in the inset. Note that in this parameter range the gap/midgap ratio increases, whereas Γ decreases with increasing d. There is a tradeoff between choosing a larger gap size versus a larger confinement factor. We choose $d = 0.8a$ for our calculations of the defect mode.

In Fig.8-5 we show the lowest two TE-like and TM-like bands for the structure with $r = 0.36a$, $d = 0.8a$ and $h = 0.3a$. It is only below the light cone that the bands shown correspond to guided modes. Above the cone the bands denote resonances: modes weakly coupled to free-space modes. There is a $\approx 3\%$ complete gap for TE-like modes between $\omega = 0.517$ and $0.531\ 2\pi c/a$.

It is important to note that even though we deal with a three-dimensional system, the lowest bands retain the character of the two-dimensional photonic crystal bands. For comparison purposes, we computed the band gap for a two-dimensional lattice of air holes in a medium with dielectric constant $\epsilon = 2.3$[3]. The TE band gap is between

[2]The complete gap must be robust against inaccuracies introduced by the lithographical methods used in the fabrication.

[3]This dielectric constant is obtained from averaging the refractive indexes of the two layers in the slab.

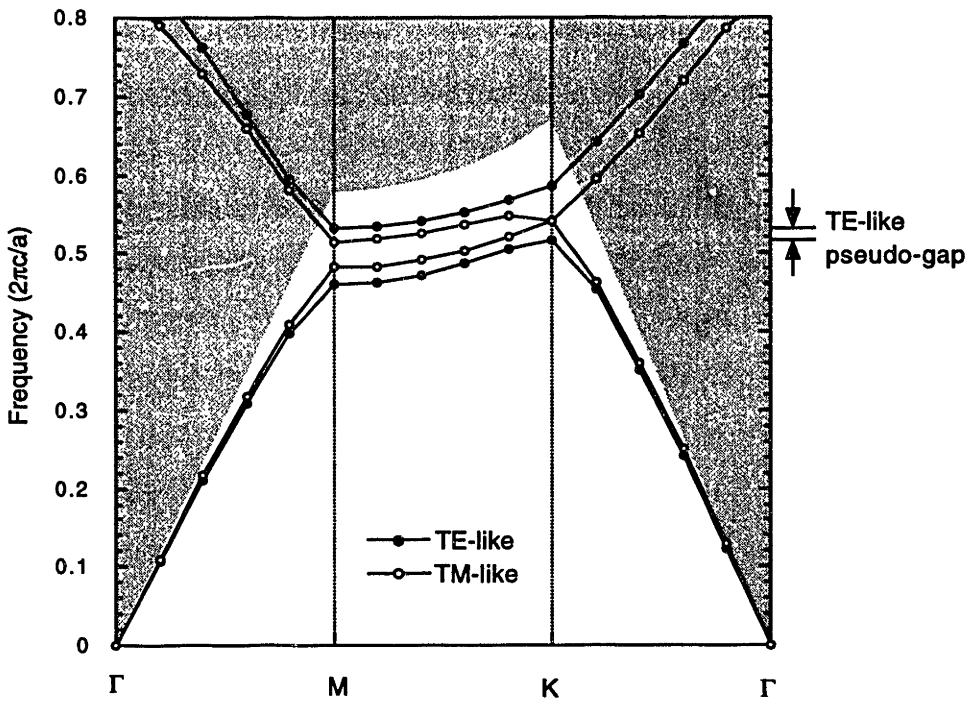

Figure 8-5: The lowest two TE- and TM-like bands (filled/open circles) for the structure with $r = 0.36a$, $d = 0.8a$ and $h = 0.3a$. The gray area stands for the radiation mdoes. The bands above the light cone denote only resonances, not true guided modes.

$\omega = 0.476$ and $0.497\ 2\pi c/a$, with a gap/midgap ratio of $\approx 4\%$. As we now turn our attention to defect modes in the photonic crystal slab, we first investigate the 2D crystal.

8.4 Defect modes in a 2D photonic crystal

A simple way to create a defect in the photonic crystal slab is to omit one hole from the lattice. We continue to investigate the resulting defect mode first in the analogous 2D photonic crystal described above. To obtain the defect mode frequencies and the field patterns, we solve Maxwell's equations in the time-domain employing a finite-difference scheme []. The computational cell has dimensions $40a \times 40a$ and the defect is in the cell center. At the cell boundaries we use perfectly matching layer absorbing boundary conditions []. We excite the defect mode by placing a dipole in the center of the cell. The dipole has frequency in the gap center and has a Gaussian time-profile. After the transient modes have decayed, we Fourier transform the field measured in the cell center to obtain the defect mode frequency, and we also record the field pattern.

There are two degenerate defect modes in the gap at frequency $\omega = 0.492\ 2\pi c/a$. Their magnetic fields are odd under reflection symmetry, one with respect to the x-axis, the other one with respect to the y-axis. In Fig.8-6 the magnitude of the magnetic field is shown for both modes, which can be studied individually by using different orientations for the dipole exciting the modes. In an ideal infinite 2D photonic crystal, the defect mode does not decay, since there are no other modes to which it can couple. However, since the field of the mode decays exponentially, the mode acquires an effective Q that depends on the computational cell used. In Fig.8-7 we plot the Q versus the cell size L for five different cell sizes (circles). The defect Q shows an exponential dependence on the cell size (solid line): $Q = 32e^{L/10a}$. The relatively slow dependence on L results from the large extent of the mode, which in turn is due to the small gap size.

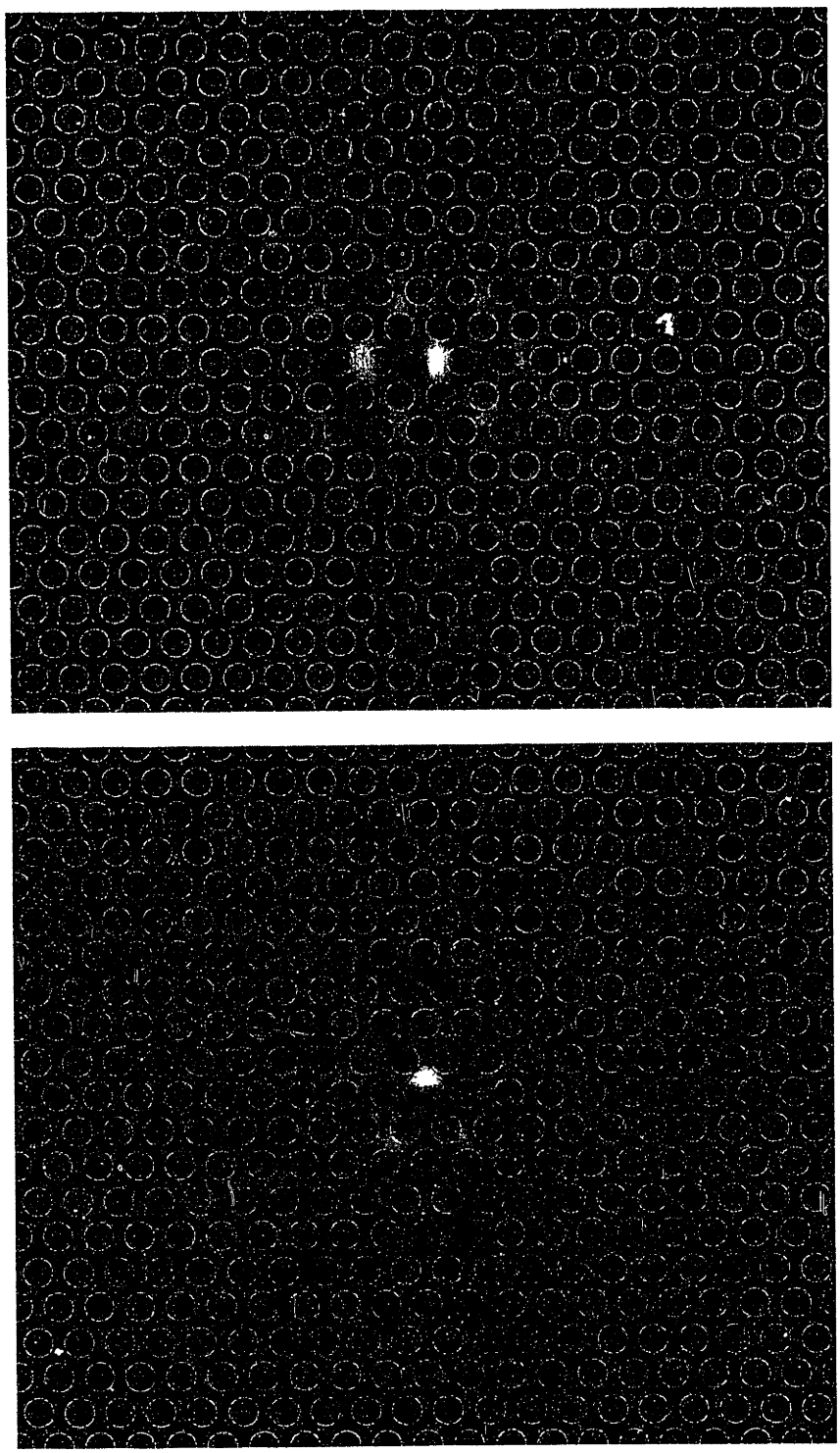

Figure 8-6: Magnitude of the magnetic field in a grayscale scheme for the two degenerate modes in a 2D photonic crystal. Only the $20a \times 10\sqrt{3}a$ central section of the computational cell is shown. White circles denote the holes.

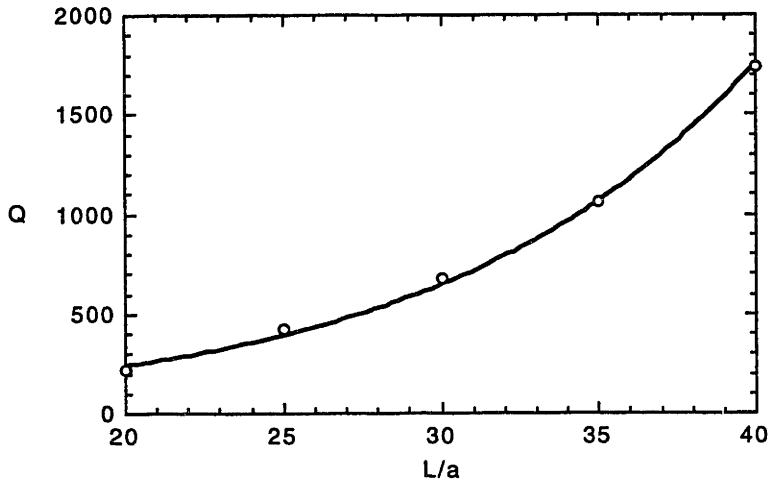

Figure 8-7: Q as a function of the cell size L.

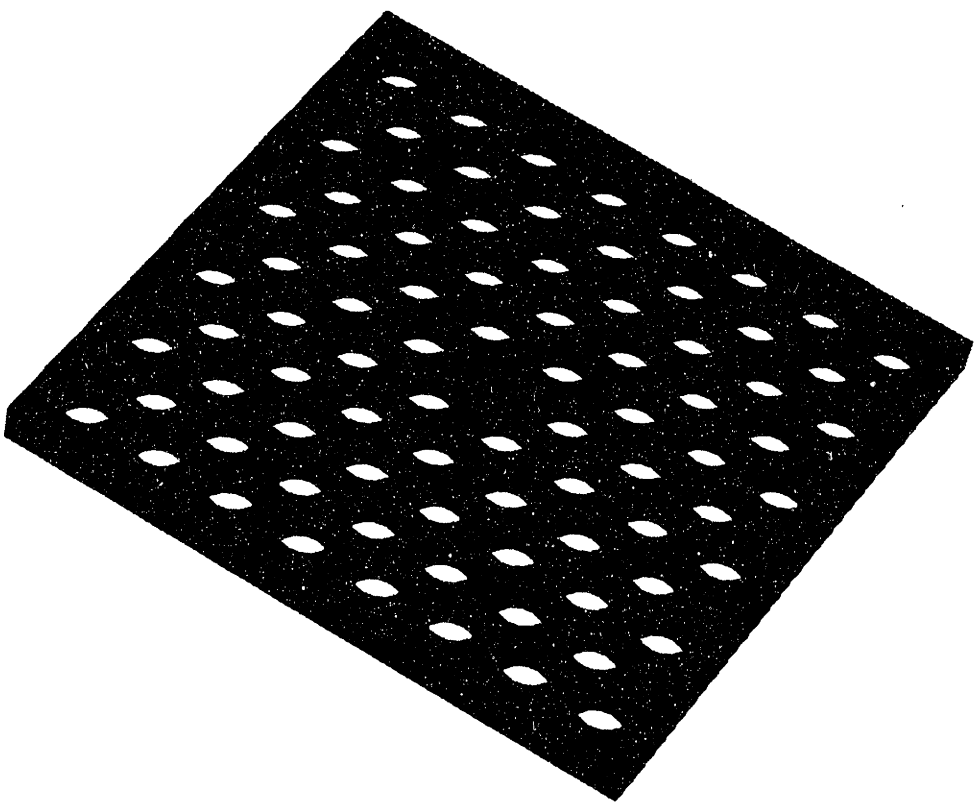

Figure 8-8: Defect in a photonic crystal slab.

8.5 Defect modes in a photonic crystal slab

Armed with information about the defect mode in the 2D photonic crystal, we go on to investigate defect modes in the photonic crystal slab. The defect in the slab is

schematically shown in Fig.8-8, obtained by omitting a hole from the photonic crystal slab for which the band structure is shown in Fig.8-5. We calculate the defect mode frequency and field distribution for the photonic crystal slab using a finite-difference scheme in a three-dimensional computational cell. The cell used for the time-domain simulation has dimensions $20a \times 10\sqrt{3}a$ in-plane and $5a$ in the z-direction. The mode with odd symmetry with respect to the y-axis is excited by a TE polarized dipole. We measure the frequency of the mode to be $\omega = 0.515\ 2\pi c/a$. The z-component of the magnetic field of the mode is shown in Fig.8-9 in a horizontal/vertical plane through the defect center on the top/bottom panels. The top panel shows a mode shape that is indeed very similar to the 2D defect mode in Fig.8-6.a. From the bottom panel it is evident that the defect mode is confined in the z-direction as well. the confinement is not due to photonic band gap effects but to index guiding.

In contrast to the case of the defect mode in the 2D photonic crystal, which has a theoretically infinite Q, there are decay channels open for this defect mode to lose power. The quality factor of the defect mode is calculated to be $Q_C = 224$ using this computational cell. We expect from the analysis done in the 2D case that the cell size significantly influences the value of Q and that the actual mode quality factor is underestimated by our result. Denoting the component in the quality factor that is due to the finite cell size by Q_F, the actual Q of the mode is obtained from:

$$\frac{1}{Q_C} = \frac{1}{Q} + \frac{1}{Q_F} \tag{8.3}$$

To quantify Q_F, we again calculate the defect mode Q for different cell sizes. We assume an exponential dependence of Q_F on the cell size in the horizontal direction, which is $L \times \sqrt{3}L/2$, and write $Q_F = Ae^{L/L_0}$, with unknowns A and L_0. We compute the Q for $L = 20$, 30, 40 to find the variables and obtain $A = 24.4$, $L_0 = 6.45$, and finally $Q = 376$ for the defect quality factor.

There are two ways the defect mode can lose power. One loss mechanism is coupling to free-space modes, and the other one is coupling to guided modes. Since the slab does not have reflection symmetry with respect to a plane parallel to the

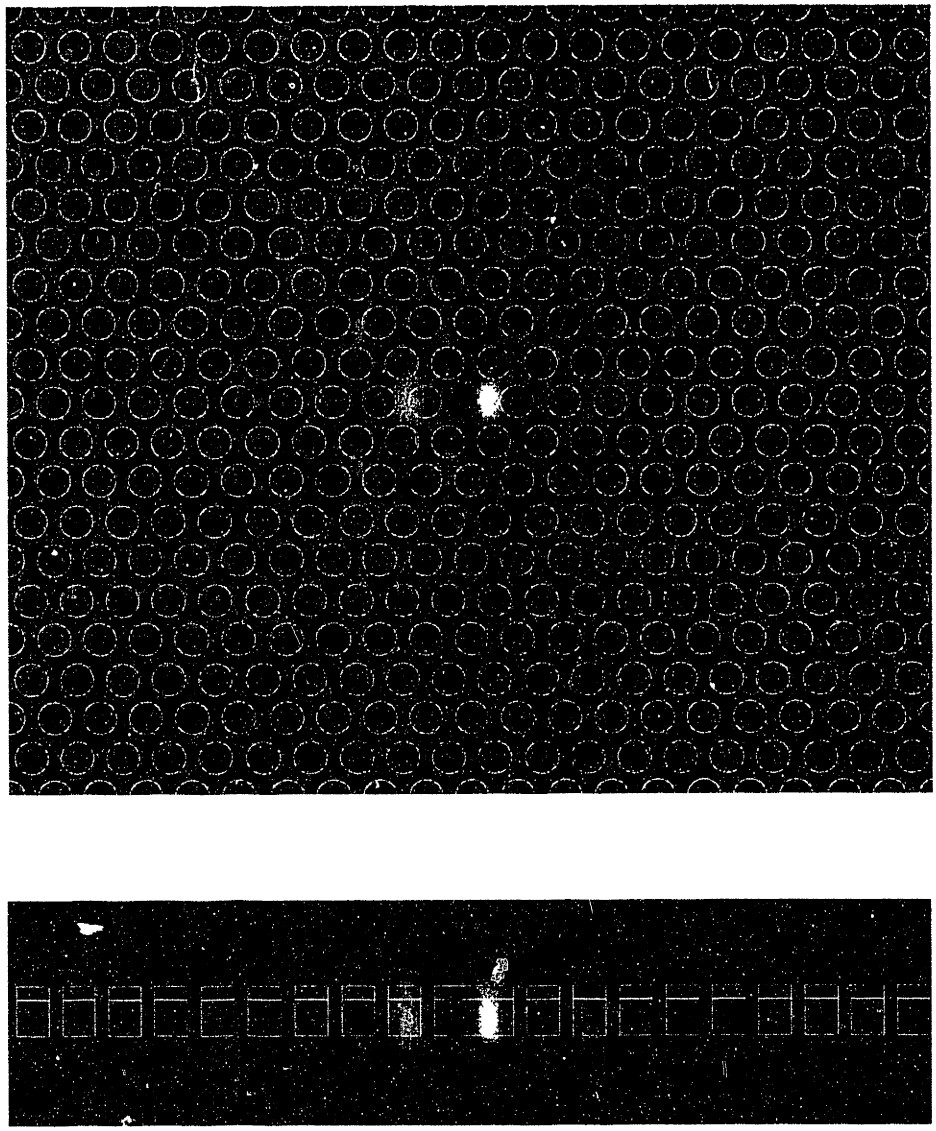

Figure 8-9: The magnitude of the z-component of the magnetic field for the defect mode in the photonic crystal slab in a grayscale scheme. Top panel: horizontal cross-section in the middle of the slab, white circles denote the holes. Bottom panel: vertical cross-section through the defect center, white lines define the slab, the holes and the SiO_2 /organic interface.

slab surface, the TE- and TM-like modes are coupled. To quantify the effect of this coupling and compare it to the effect of coupling to radiation modes, we calculate the Q of defect modes with different substrate refractive indexes n. If coupling to TM-like modes is a major loss mechanism, we would expect that the defect Q has a peak when the slab has a symmetry plane (at $n = 1.7$).

We plot our results in Fig.8-10 for cell size $L = 20$. Full circles/solid line stand for the calculated Q and the squares/dashed line for the frequency of the defect mode as a function of the substrate index. The frequency falls as n (along with the effective index of the slab) increases. With growing n, the calculated Q also falls monotonically in the range shown. The reason for this is that as n increases, the index contrast between the material and the holes becomes larger. The band gap size goes up and the defect mode in the gap becomes more and more localized. Strong localization in real space means that many k-components are involved to make up the defect mode, which increases coupling to radiation modes, spoiling the defect Q. This monotonical drop in the value of Q as a function of n and the absence of a notable peak at $n = 1.7$ also demonstrates that the main loss mechanism is coupling to radiation modes. In spite of the lack of a complete gap, the defect mode has a high quality factor for low index substrates. To investigate the effect of the cell size on the results of our calculations, we also plot in Fig.8-10 the Q calculated with a larger cell size $L = 30$ (open circles). For $n \geq 1.6$, the value of the quality factor is almost unchanged, because the mode volume is much smaller then in the case of the SiO_2 substrate. As the substrate index increases, so does the gap size, and the effective mode volume goes down. Therefore Q_F decreases and the mode Q approaches the real value more closely with increasing n.

This analysis points us towards the important parameters to consider when designing a high-Q defect mode. One way to achieve a high quality factor is a small band gap. This causes the defect mode to be spread out, which reduces radiation coupling. One can also increase the mode size in the case of the higher index substrates considered in this chapter. For larger gaps, we can vary the neighboring hole sizes close to the defect center to achieve relatively weak localization of the mode.

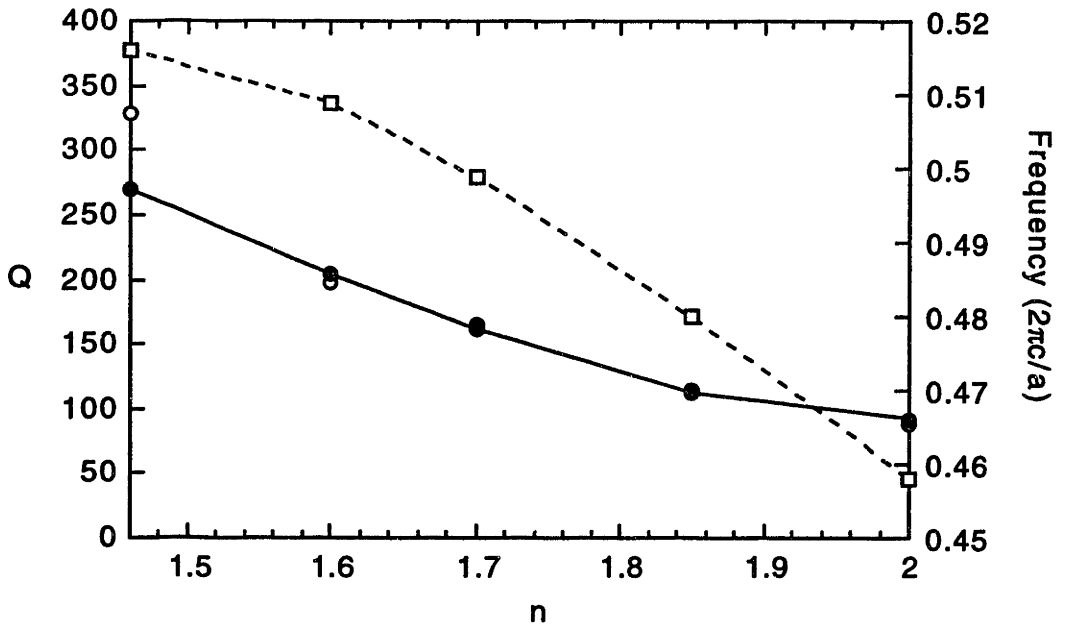

Figure 8-10: The frequency (dashed line) and the quality factor (solid line) of the defect mode as a function of the substrate index n. Full/open circles denote the quality factor calulated using a cell size $L = 20/L = 30$.

Naturally, there is a tradeoff between a large effective volume V (meaning larger Q) and high spontaneous emission enhancement η. Since from (8.1) we know that η is proportional to the ratio Q/V, there will be optimal designs that maximize η. Such designs are subject to further investigations.

8.6 Summary

We have designed a photonic crystal slab with a complete pseudogap for TE-like polarized modes. An analysis of the effect of the parameters on the band gap revealed the optimal parameters in the design of the system. We showed that a defect in this slab can support a high-Q defect mode with a quality factor estimated to be about 400. Even though the photonic crystal slab does not have reflection symmetry, the decay of the defect mode is mainly due to coupling to radiation modes and not to guided modes. This result and the relatively small pseudogap size explains the high quality factor of the defect mode observed and points us to a future directions in

high-Q defect mode design.

Chapter 9

Two-dimensional photonic crystal couplers for unidirectional light output

9.1 Introduction

Output couplers are important components in integrated photonic circuits. Traditionally, one-dimensional grating couplers (GCs) [51, 52] and focusing GCs [53, 55, 54] have been used to achieve coherent light scattering out of the waveguide plane. Both of these gratings have periodicity in a single spatial direction. One-dimensional GC's have straight grooves, whereas focusing GC's, also called grating lenses, have a curvelinear grating. Additionally, with tiny, high power DFB lasers as light sources of choice in many optical communications systems, coupling the laser light out of planar waveguides and possibly into fibers is a crucial technological issue.

The direction of light output from the couplers is determined by phase-matching the scattered wave to the guided wave. This yields the condition that the in-plane component of the scattered wavevector be equal to the difference between the guided mode wavevector and a reciprocal lattice vector of the grating. Because there is a single constraint for two angular directions (polar and azimuthal), the resulting output

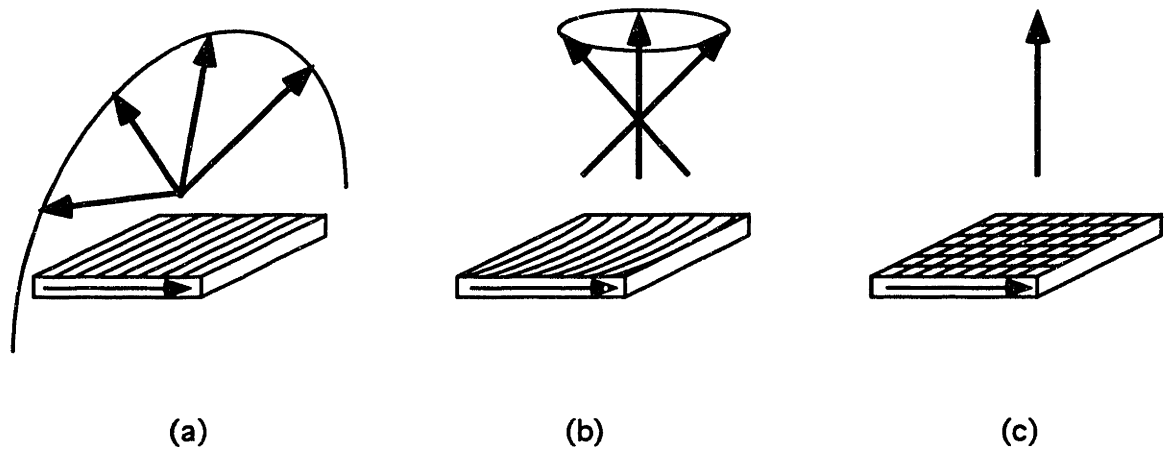

Figure 9-1: Schematic of light output from three types of grating couplers. The arrow within the guide shows the guided mode propagation direction and the arrows out of plane indicate light output directions. Only a small section of the grating is shown. a) A one-dimensional grating coupler. b) A grating lens. c) A two-dimensional photonic crystal coupler.

is not unidirectional. One-dimensional GC's couple light to a cylindrical wave, so only a part of the output can be picked up by a fiber, for instance (Fig.9-1.a). Grating lenses focus light to a point in space in the vicinity of the grating at a distance on the order of the grating size (Fig.9-1.b). This puts a restriction on the distance at which the receiver that the light is coupled to can be placed, and in the far-field, light is coupled to a spherical wave.

In this chapter, we propose the use of doubly periodic gratings, also known as two-dimensional photonic crystals (PCs), to achieve a dramatic improvement over traditional GCs in coupling directionality. As in one-dimensional GCs, it is the phase matching condition that determines the direction of output. However, in a two-dimensional PC coupler, the introduction of periodicity in an additional spatial direction increases the number of constraints on the output angles to two. This means that light can be coupled out into a single or a discrete number of directions, shown schematically in Fig.9-1.c. In the following, we first discuss the coupling mechanism in two-dimensional PC couplers, and then investigate the effect of the design parameters on the output directions. Finally we use numerical simulations to calculate the coupling constants for a PC coupler in specific waveguiding structure.

9.2 Coupling mechanism in two-dimensional photonic crystal coupler

For a general two-dimensional PC coupler, we consider a grating in a planar dielectric waveguide on top of a substrate. Let the wavevector of the waveguided mode incident on the grating section be $\mathbf{k}$, its free-space wavelegth λ, the in-plane component of the scattered radiation wavevector $\mathbf{K}$, and the polar angle of the output direction θ. If the number of periods in the grating is large, the field scattered by the grating will interfere constructively only in certain directions, just as in the one-dimensional case. The phase-matching condition is

$$\mathbf{k} = \mathbf{K} + \mathbf{G} \tag{9.1}$$

where $\mathbf{G}$ is a reciprocal lattice vector by which the lattice diffracts the propagating mode out of the guide. The azimuthal angle of the radiation direction is easily determined from (9.1) and the polar angle from the same equation as

$$\sin\theta = \frac{\lambda|\mathbf{k} - \mathbf{G}|}{2\pi n} \tag{9.2}$$

where n is the refractive index of the medium (air or substrate) into which the radiation is emitted.

In Fig.9-2 we show the phase-matching condition in a reciprocal lattice of a two-dimensional PC coupler for a certain guided mode wavevector. The emitted radiation is in two directions $\mathbf{K}$, $\mathbf{K}'$, so this grating acts as a two-way splitter. Light is emitted into one half-space into two directions, with different azimuthal and polar angles. This is not possible in a traditional GC. Since $\sin\theta \leq 1$, there are only a finite number of reciprocal lattice vectors that satisfy (9.2). To achieve coupling in the desired spatial directions, one must choose the lattice parameters correctly.

To demonstrate this on a particular structure, we design a GC that couples light only vertically out of a waveguide used in an organic distributed feedback (DFB) laser

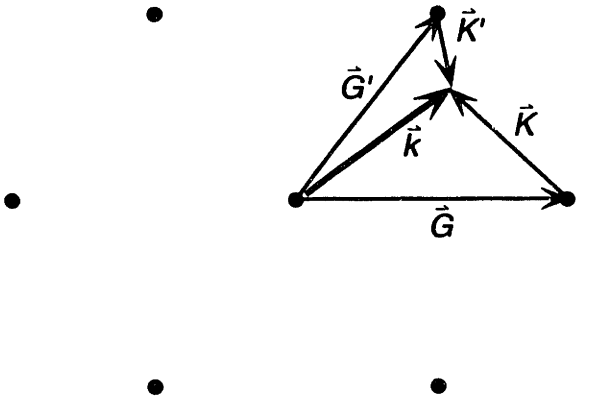

Figure 9-2: Reciprocal lattice for a two-dimensional grating. Shown are the guided mode wavevector, k, two possible reciprocal lattice vectors G, G′ satisfying the phase matching condition, and the in-plane components of the two corresponding radiation mode wavevectors K, K′.

[38]. The advantage of this design is that the coupler can be integrated on the same waveguide adjacent to the laser and can be fabricated together with the laser, making the DFB laser surface-emitting. The operation of semiconductor organic DFB lasers has been described in the literature [56, 34]. The waveguide we consider consists of two layers on top of a SiO_2 substrate (refractive index $n = 1.46$), a 100 nm thick Si_3N_4 layer ($n = 2.0$) on top of which a 50 nm organic layer is sublimed ($n = 1.7$). The PC coupler is etched into the Si_3N_4 layer before sublimation of the top layer so that the organic material fills the holes comprising the grating. The PC is selected to be a square lattice of holes with lattice constant a, hole radius $r = 0.375a$, and hole depth b, as shown in Fig.9-3. It is nevertheless also possible to achieve vertical coupling using other kind of lattices, such as triangular ones.

The lattice parameters are chosen as follows. To satisfy (9.2) for vertical emission ($\theta = 0$), k must be a reciprocal lattice vector. For *only* vertical emission for both into substrate and air, we must require that the right-hand-side be larger than 1 for $|\mathbf{k} - \mathbf{G}| > 0$. This is only possible if $a < \lambda/n$. In terms of the guide effective index n_e, this also implies that $ka/2\pi < n_e/n$ must hold for both substrate and air refractive indexes n. In our case $\lambda = 650$ nm, $n_e = 1.63$ and $n = 1.46$, so the only choice is $k = 2\pi/a$. This yields a lattice constant $a = 400$ nm, which is presently

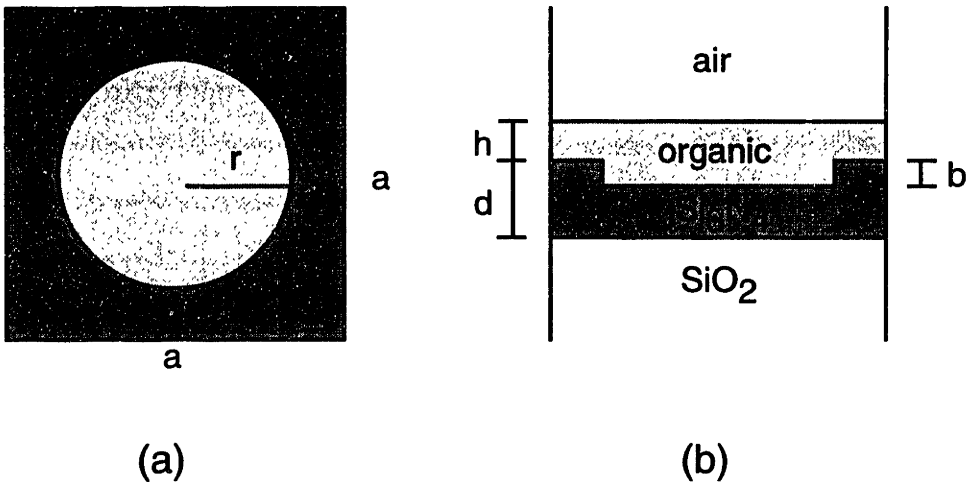

Figure 9-3: a) Horizontal cross-section of the unit cell of the grating in the grating region. b) Vertical view of the unit cell.

achievable with lithographical methods. If the index contrast between the guide and the substrate is larger and the ratio n_e/n is greater, it may be possible to choose from several feasible lattice constants.

9.3 Numerical calculation of the coupling constant

Next we calculate the coupling constant for this waveguide grating. For simplicity, let the guided mode propagation direction be x, and let the grating have length L_x in this direction. As the mode propagates, its intensity decays exponentially due to scattering losses. The *amplitude* coupling constant α is defined as one half of the fractional change in the power flux P along the guide. The power flux and the energy E per unit length are related to the group velocity v_g of the waveguide without the grating through [57]

$$P = v_g E / L_x \tag{9.3}$$

and the total radiated power scattered by the grating is $P_s = dE/dt$. Therefore we can express α in terms of E as

$$\alpha = -\frac{1}{2P}\frac{dP}{dx} = -\frac{1}{2P}\frac{P_s}{L_x} = \frac{1}{2v_g}\frac{d(\ln E)}{dt} \tag{9.4}$$

In our numerical simulations we solve Maxwell's equations in the time-domain using a finite-difference scheme on a three-dimensional rectangular grid [25]. The grid is periodic in the x- and y-directions, and contains one unit cell of the photonic crystal slab. In the z-direction, the cell is terminated by a second-order Mur's absorbing boundary condition [58]. A TE polarized dipole source with a Gaussian time-profile placed in the center of the slab excites a guided mode of the slab. We measure the energy in the cell and the flux through the top and bottom as a function of time. The cell is long enough in the z-direction so that the escaping flux due to the finite extent of the cell is negligible compared to the energy in the mode for a slab without the grating.

Since the excited mode is a superposition of two counter-propagating waves, one must be careful to interpret the results. The grating has a plane of symmetry perpendicular to the propagation direction x. The two propagating modes combine to give a mode that is symmetric and one that is asymmetric with respect to reflection through this plane. The asymmetric mode cannot couple to free-space plane waves, so no energy is lost from the slab when this mode is excited. The symmetric mode, however, loses energy at twice the rate of the propagating mode. In contrast to one-dimensional gratings, modes can combine in a more complicated fashion, four modes, or even six, for instance, in a triangular lattice, can mix.

We observe an exponential decay of the energy of the symmetric mode excited by the pulse, as expected. We use equation (9.4) to determine 2α from the decay constant. The unperturbed waveguide for which v_g is used in (9.4) is not simply the original waveguide with $b = 0$ but is defined by the zeroth order component in the Fourier decomposition of the dielectric constant. For fixed b, this is a waveguide with $b = 0$, effective organic thickness $h = h_e = 50$ nm $+ \pi r^2 b$ and $d = 150$nm -- h. The resulting group velocity found from the dispersion relation for this waveguide [57] fits very well the formula $v_g/c = 0.508 + (b + 0.125)^2$, where b is given in units of μm.

In Fig.9-4 we plot the resulting coupling constant and the ratio of the power coupled into air to the total scattered power, both as a function of the grating depth. For small b, the increase is quadratic, as in one-dimensional GCs. [66] At its maximum,

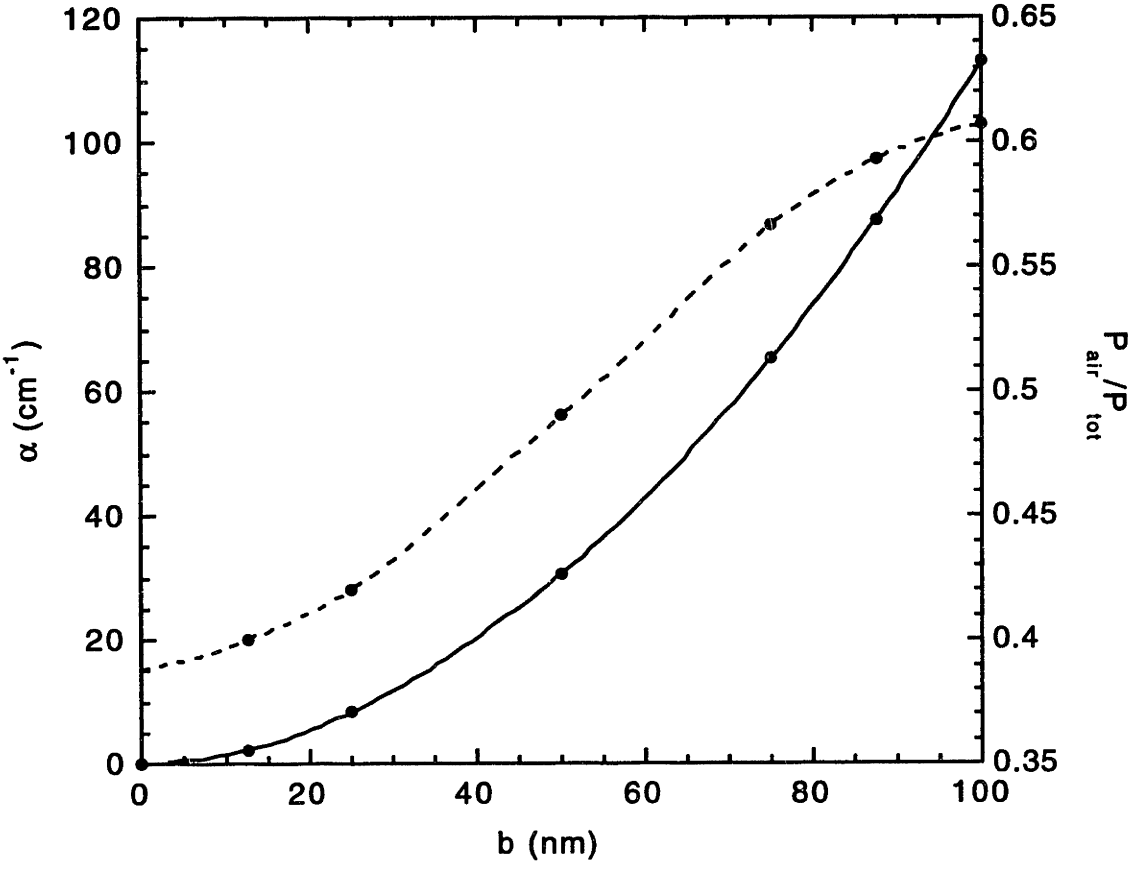

Figure 9-4: Solid line: the coupling constant for the structure in Fig.9-3 with lattice constant $a = 400$nm. Dashed line: ratio of power coupled into air to total power coupled out for the same structure. The circles are calculated values, and the lines are interpolated curves.

the coupling constant exceeds 110 cm^{-1}. Even though this coupling constant would still require a grating of length $\approx 100\mu$m, one can reduce the coupler size by using a one-dimensional grating with a photonic band gap at the PC coupler end to reflect light back into the coupler. The beam divergence of the emitted light beam is on the order of λ/nL, where L is the size of the grating in the direction the beam divergence is measured. For a 30 μm $\times$ 30 μm grating this is about 1° for radiation into air, making possible compact and very efficient PC couplers.

The coupling efficiency as shown in Fig.9-4 increases with b and exceeds 60% at the maximum depth considered. Since at $b = 0$ the ratio is undetermined, the efficiency for small b was obtained from interpolation using a structure with $b < 0$,

that is, a Si_3N_4 cylinder of height $-b$ protruding into the organic layer. The increase with b and the turnoff at large grating depth can be understood by considering the scattering due to the perturbation as a source of a plane wave in the Si_3N_4 layer. The coefficient of transmission into air through an organic layer of effective thickness h_e and index n has maxima at $h_e = N\pi c/2\omega n$, N an odd integer. From this simple picture we expect transmission to be approximately sinusoidal as h_e changes, with a maximum at $h_e = 96$ nm, or, $b = 103$ nm (from $N = 1$). This is in good qualitative agreement with the calculated coupling efficiency.

9.4 Summary

In conclusion, we have shown that two-dimensional PC couplers can couple light into a discrete number of directions in the far-field, an improvement over traditional GCs. A particularly useful form of 2D PC couplers has been described which causes unidirectional coupling. Compact PC couplers with short coupling lengths and small beam divergences are possible that can be fabricated together with planar DFB lasers. Because of the time-reversibility of Maxwell's equations, it is also possible to couple light into planar waveguides with the same type of PC couplers from vertically emitting sources, such as vertical cavity surface emitting lasers.

Chapter 10

Perturbation approach to two-dimensional photonic crystal slab couplers

10.1 Introduction

In the previous chapter, we proposed the use of doubly periodic gratings, also known as two-dimensional photonic crystals, to improve the directionality of output coupling from planar waveguides and distributed feedback lasers. In this chapter, we employ the volume current method (VCM) to determine the coupling constants and coupling efficiencies for TE polarized modes due to a two-dimensional (2D) grating in a dielectric slab. This method was first proposed by Snyder [59] and have been useful in determining radiation losses due to small perturbations in general dielectric waveguide structures, such as fibers [59], waveguide bends [60, 61] and couplers [62]. Recently, this method was applied to determine the amount of radiation due to imperfections on microdisk lasers [63] and also the radiation patterns for a concentric-circle-grating surface-emitting laser [64].

The VCM is a perturbation method appropriate for finding the amount of radiation coupling in dielectric structures with localized modes, such as waveguides with

guided modes. Let the structure be defined by a dielectric constant $\epsilon(\mathbf{r})$ and let us introduce a perturbation $\Delta\epsilon(\mathbf{r})$ to it. In this case, Maxwell's equations can be written for the electric field as

$$\nabla \times (\nabla \times \mathbf{E}(\mathbf{r})) - \frac{\omega^2}{c^2}\epsilon(\mathbf{r})\mathbf{E}(\mathbf{r}) = 4\pi i\frac{\omega}{c^2}\mathbf{J}(\mathbf{r}) \tag{10.1}$$

where we introduced the volume current

$$\mathbf{J}(\mathbf{r}) = -\frac{i\omega}{4\pi}\,\Delta\epsilon(\mathbf{r})\mathbf{E}(\mathbf{r}) \tag{10.2}$$

In general, this is a difficult problem to solve due to the arbitrariness of the dielectric perturbation, so we proceed in the approximation that $\Delta\epsilon$ is small. To calculate the scattered fields due to some field incident on the perturbed section (which can be either an extended or a localized mode), we assume that the perturbation does not considerably change the modes, so we can replace $\mathbf{E}(\mathbf{r})$ in (10.2) by the extended or localized mode already known. The scattered field solutions to (10.1) can be found in terms of the far-field form of the dyadic Green's function $\bar{G}(\mathbf{r},\mathbf{r}')$:

$$\mathbf{E}_s(\mathbf{r}) = \frac{i\omega}{c^2}\int d\mathbf{r}'\bar{G}(\mathbf{r},\mathbf{r}')\mathbf{J}(\mathbf{r}') \tag{10.3}$$

So far in VCM calculations of radiation from waveguides the free space dyadic Green's function has been used. This yields acceptable results as long as the waveguide is surrounded by a uniform medium on all sides. However, it is known from one-dimensional (1D) grating coupler analysis [66] that when the substrate underneath the waveguide is different from the medium above the waveguide, the radiation emitted into above or below the waveguide can be substantially different. The exact results can be only recovered by the VCM if the appropriate Green's function is used.

In this chapter, we calculate the far-field form of the dyadic Green's function for a dielectric slab waveguide, and then determine the output and in-plane coupling constants for TE polarized modes for a two-dimensional grating on a slab waveguide. The same results can naturally be used in an analysis of out of plane coupling from

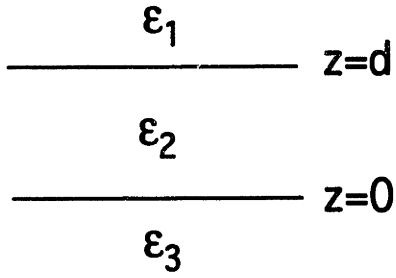

Figure 10-1: A uniform dielectric slab.

a 2D photonic crystal laser. The VCM yields equivalent results to coupled mode analysis, however, without the algebraic difficulties encountered due to mode normalization requirements in the latter method [65]. The advantage of the VCM as applied to radiation coupling in periodic systems over coupling mode theory stands in that the former yields the in-plane coupling constants very simply and directly.

10.2 The dyadic Green's functions

First we define the guided modes of the dielectric slab waveguide shown schematically in Fig.10-1. We assume $n_2 > n_3 \geq n_1$. Let the dielectric constant be $\epsilon_i = n_i^2$, and the free space propagation constant $k_0 = \omega/c$. Consider a TE-mode with wavevector $\mathbf{k}$ parallel to the waveguide. Let

$$\begin{aligned} k_1 &= \sqrt{k^2 - \epsilon_1 k_0^2} \\ k_2 &= \sqrt{\epsilon_2 k_0^2 - k^2} \\ k_3 &= \sqrt{k^2 - \epsilon_3 k_0^2} \end{aligned} \tag{10.4}$$

The electric field for TE guided modes can be written as $E_k(z)e^{i\mathbf{k}\cdot\mathbf{r}}\,\hat{\mathbf{k}} \times \hat{\mathbf{z}}$, where

$$\begin{aligned} E_k(z) &= \sqrt{\frac{\epsilon_2 - \epsilon_3}{\epsilon_2 - \epsilon_1}} e^{k_1(d-z)} && (z \geq d) \\ &= \cos k_2 z + k_3/k_2 \sin k_2 z && (0 \leq z < d) \\ &= e^{k_3 z} && (z < 0) \end{aligned} \tag{10.5}$$

The power per unit length in the $\hat{\mathbf{k}} \times \hat{\mathbf{z}}$-direction carried by the wave is

$$P_g = \frac{ck}{8\pi k_0} \int dz E_k(z)^2 = \frac{(\epsilon_2 - \epsilon_3) c k_0 k D}{16\pi k_2^2} \tag{10.6}$$

where D is the effective guide width: $D = d + 1/k_1 + 1/k_3$. The wavenumber k must satisfy the following equation that defines the dispersion relation [66]:

$$\tan k_2 d = \frac{k_2(k_1 + k_3)}{k_2^2 - k_1 k_3} \tag{10.7}$$

For TE to z plane waves in regions $j = 1, 3$, we use the following notations. Consider a plane wave that is incident on the waveguide with an angle of incidence θ. The wave has an electric field $e^{-in_j k_0 r} \hat{K} \times \hat{\mathbf{z}}$ from region j where $\mathbf{K}$ is the in-plane component of the wavector, $K = n_j k_0 \sin\theta$. We let $K_{j'}$ stand for the z-component of the propagation constant in region l:

$$K_{j'} = \sqrt{\epsilon_{j'} k_0^2 - K^2} \tag{10.8}$$

Notice that $K_j = n_j k_0 |\cos\theta|$. The power incident on a unit area of the waveguide is $P_r = cK_j/8\pi k_0$.

We proceed to calculate explicitly the far-field dyadic Green's functions for the asymmetric slab. We assume a source at $\mathbf{r}'$ in region 2 and the observation point $\mathbf{r}$ in region j. Defining $k_{jz} = \sqrt{\epsilon_j k_0^2 - k_\rho^2}$ and $\bar{\rho} = |\boldsymbol{\rho} - \boldsymbol{\rho}'|$, for $\mathbf{r} \neq \mathbf{r}'$ the Green's function for TE modes has the form [67]

$$\bar{G}_j(\mathbf{r}, \mathbf{r}') = \frac{i}{2\pi} \int_0^\infty dk_\rho \frac{k_\rho}{k_{2z}} F_j(z, z') \int_0^{2\pi} d\phi_\rho (\hat{\mathbf{k}}_\rho \times \hat{\mathbf{z}})(\hat{\mathbf{k}}_\rho \times \hat{\mathbf{z}}) e^{ik_\rho \bar{\rho} \cos(\phi_\rho - \phi)} \tag{10.9}$$

where

$$\begin{aligned}
F_1(z, z') &= 2W k_{2z} e^{ik_{1z}(z-d)} (k_{2z} \cos k_{2z} z' - ik_{3z} \sin k_{2z} z') \\
F_2(z, z') &= 2W (k_{2z} \cos k_{2z}(z_> - d) + ik_{1z} \sin k_{2z}(z_> - d))(k_{2z} \cos k_{2z} z_< - ik_{3z} \sin k_{2z} z_<) \\
F_3(z, z') &= 2W k_{2z} e^{-ik_{3z} z} (k_{2z} \cos k_{2z}(z' - d) + ik_{1z} \sin k_{2z}(z' - d))
\end{aligned} \tag{10.10}$$

and $W = k_{2z}(k_{1z} + k_{3z})\cos k_{2z}d - i(k_{1z}k_{3z} + k_{2z}^2)\sin k_{2z}d$. The variables $z_>$ and $z_<$ are respectively the larger and smaller of z and z'. If $\bar{\rho}$ is large, the angular integral is highly oscillatory, and it can be evaluated by saddle point integration. The two stationary phase points are at $\phi_\rho = \phi, \phi + \pi$, which yields after integration

$$\bar{G}_j(\mathbf{r},\mathbf{r}') = 2\sqrt{\frac{i}{2\pi\bar{\rho}}}(\hat{\boldsymbol{\rho}}\times\hat{\mathbf{z}})(\hat{\boldsymbol{\rho}}\times\hat{\mathbf{z}})\int_0^\infty dk_\rho \frac{\sqrt{k_\rho}}{k_{2z}} e^{ik_\rho\bar{\rho}}F_j(z,z') \tag{10.11}$$

We use $\hat{\boldsymbol{\rho}}$ as the unit vector in the direction of the projection of $\mathbf{r}$ onto the plane. The radial integral is also highly oscillatory. Contributions to this integral are made at stationary phase points, branch cuts and poles. The branch cut integrals give rise to lateral waves, which we ignore in the far-field approximation. For radiation into region 1, the main contribution comes from the stationary phase point at $k_{\rho s} = n_j k_0\bar{\rho}/|\mathbf{r}-\mathbf{r}'| \approx n_j k_0 \sin\theta$; here $k_{jz} = K_j$ as defined in (10.8). Expanding $\bar{\rho} \approx \rho - \hat{\boldsymbol{\rho}}\cdot\boldsymbol{\rho}'$, we obtain the Green's function by saddle point integration:

$$\begin{aligned}
\bar{G}_j(\mathbf{r},\mathbf{r}') &= (\hat{\boldsymbol{\rho}}\times\hat{\mathbf{z}})(\hat{\boldsymbol{\rho}}\times\hat{\mathbf{z}})e^{in_jk_0r}E_j(z',\theta)e^{-iK\hat{\boldsymbol{\rho}}\cdot\boldsymbol{\rho}'}/r \\
E_1(z',\theta) &= \frac{2K_1(K_2\cos K_2z' - iK_3\sin K_2z')}{K_2(K_1+K_3)\cos K_2d - i(K_1K_3+K_2^2)\sin K_2d} \\
E_3(z',\theta) &= \frac{2K_3(K_2\cos K_2(z'-d) + iK_1\sin K_2(z'-d))}{K_2(K_1+K_3)\cos K_2d - i(K_1K_3+K_2^2)\sin K_2d}
\end{aligned} \tag{10.12}$$

For radiation into region 2, the poles give the main contribution. They correspond to guided modes and occur at $k_\rho = k$, where k satisfies (10.7). At the poles, $k_{1z} = ik_1$, $k_{2z} = k_2$, and $k_{3z} = ik_3$, as defined in (10.4). The residue of $F_2(z,z')$ is $ick_2E_k(z_<)E_k(z_>)/k_0P_g$, with E_k given in (10.5), so by residue calculus, we get the following expansion of the far-field Green's function in guided modes:

$$\bar{G}_2(\mathbf{r},\mathbf{r}') = (\hat{\boldsymbol{\rho}}\times\hat{\mathbf{z}})(\hat{\boldsymbol{\rho}}\times\hat{\mathbf{z}})\sum_k \frac{c}{4k_0P_g}\sqrt{\frac{ik}{2\pi\rho}}E_k(z)e^{ik\rho}E_k(z')e^{-ik\hat{\boldsymbol{\rho}}\cdot\boldsymbol{\rho}'} \tag{10.13}$$

10.3 Output coupling

When calculating the output coupling constant, we wish to compare the power carried by a guided mode and the power scattered out of the waveguide by the grating. The *amplitude* coupling constant is defined as one half of the fractional change in the power flux P_p propagating in the guide in the propagation direction per unit length. Let this direction be x. If the total radiated power P and the power P_g carried by the guided mode per unit y are known, then

$$\alpha = -\frac{1}{2P_p}\frac{dP_p}{dx} = \frac{1}{2P_g L_y}\frac{P}{L_x} = \frac{P}{2A_g P_g} \tag{10.14}$$

where $A_g = L_x L_y$ is the area of the grating.

Let us now find the power scattered into regions $j = 1, 3$ by the grating from a wave with wavevector $\mathbf{k}$. Substituting the Green's function given in (10.12) into (10.3), and using the guided mode E-field in (10.2), the scattered field takes the form

$$\mathbf{E}_s(\mathbf{r}) = \frac{k_0^2 e^{in_j k_0 r}}{4\pi r}(\hat{\boldsymbol{\rho}} \times \hat{\mathbf{z}})(\hat{\boldsymbol{\rho}} \cdot \hat{\mathbf{k}}) \int d\mathbf{r}' \Delta\epsilon(\mathbf{r}') E_j(z', \theta) E_k(z') e^{i(\mathbf{k} - K\hat{\boldsymbol{\rho}})\cdot\boldsymbol{\rho}'} \tag{10.15}$$

K is the in-plane component of the wavevector of the radiation field. The power P scattered into an infinitesimal solid angle is

$$\frac{dP}{d\Omega} = \frac{c}{8\pi}(r^2\, \hat{r} \cdot \mathbf{E}_s \times \mathbf{B}_s^*) = \frac{c n_j k_0^4}{128\pi^3}(\hat{\boldsymbol{\rho}} \cdot \hat{\mathbf{k}})^2 \left| \int d\mathbf{r}' \Delta\epsilon(\mathbf{r}') E_j(z', \theta) E_k(z') e^{i(\mathbf{k} - K\hat{\boldsymbol{\rho}})\cdot\boldsymbol{\rho}'} \right|^2 \tag{10.16}$$

Now let the grating vary in a periodic fashion:

$$\Delta\epsilon(\mathbf{r}) = \sum_{\mathbf{R}} \delta\epsilon(\mathbf{r} - \mathbf{R}) \tag{10.17}$$

where the sum is over the lattice vectors $\mathbf{R}$. After a change of variables, the total power scattered into region j can be written as

$$P = \frac{c n_j k_0^4}{128\pi^3} \int d\theta \, \sin\theta \, d\phi (\hat{\boldsymbol{\rho}} \cdot \hat{\mathbf{k}})^2 \left| \sum_{\mathbf{R}} e^{i(\mathbf{k} - K\hat{\boldsymbol{\rho}})\cdot\mathbf{R}} \right|^2 \left| \int d\mathbf{r}' \delta\epsilon(\mathbf{r}') E_j(z', \theta) E_k(z') e^{i(\mathbf{k} - K\hat{\boldsymbol{\rho}})\cdot\boldsymbol{\rho}'} \right|^2 \tag{10.18}$$

The spatial integral is now taken over one unit cell. If the grating contains an infinite number of unit cells, the sum vanishes unless the phase matching condition is satisfied:

$$\mathbf{k} - K\hat{\boldsymbol{\rho}} = \mathbf{G} \tag{10.19}$$

where $\mathbf{G}$ is a reciprocal lattice vector. Consider a finite 2D lattice whose reciprocal space lattice vectors are $\mathbf{G} = 2\pi(n\hat{u} + m\hat{v})/a$ $(0 \leq n < N,\ 0 \leq m < M)$. Let also the vector between a vector $\hat{\gamma}$ and the x-axis be ϕ_γ, and the angle between the two reciprocal lattice vectors ϕ_0. Now,

$$\lim_{N\to\infty} \frac{1}{N} \left| \sum_{n=0}^{N-1} e^{ikan} \right|^2 = \lim_{N\to\infty} \frac{1}{N} \frac{\sin^2(Nka/2)}{\sin^2(ka/2)} = \frac{2\pi}{a} \sum_n \delta\left(k - \frac{2\pi n}{a}\right) \tag{10.20}$$

Therefore for large N, M, we can replace the square of the sum under the integral sign by the following expression:

$$\frac{4\pi^2}{a^2} NM \sum_{nm} \delta\left(k\cos(\phi_k - \phi_u) - K\cos(\phi - \phi_u) - \frac{2\pi}{n}\right) \cdot \\ \delta\left(k\cos(\phi_k - \phi_v) - K\cos(\phi - \phi_v) - \frac{2\pi}{m}\right) \tag{10.21}$$

The delta functions give condition (10.19). Thus the total scattered power is the sum over $P_{\mathbf{G}}$ belonging to different reciprocal lattice vectors $\mathbf{G}$ by which radiation is scattered out of the guide. Noting that $K = n_j k_0 \sin\theta$, we can evaluate the integrals to obtain

$$P_{\mathbf{G}} = \frac{cNMk_0^2}{32\pi(\epsilon_2 - \epsilon_3)a^2} \frac{\cos^2(\phi_K - \phi_k)}{n_j|\cos\theta_K||\sin\phi_0|} \left| \int d\mathbf{r}\, \delta\epsilon(\mathbf{r}) E_j(z, \theta_K) E_k(z) e^{i\mathbf{G}\cdot\boldsymbol{\rho}} \right|^2 \tag{10.22}$$

where θ_K, ϕ_K are the angles of the radiation mode wavevector $K\hat{\boldsymbol{\rho}}$ that satisfies (10.19) for the given $\mathbf{G}$. The area of the grating is $A_g = NMa^2|\sin\phi_0|$, so (10.14) yields a coupling constant α which is the sum over

$$\alpha_{\mathbf{G}} = \frac{k_2^2 k_0^2 \cos^2(\phi_K - \phi_k)}{4(\epsilon_2 - \epsilon_3) K_j k D a^4 \sin^2\phi_0} \left| \int d\mathbf{r}\, \delta\epsilon(\mathbf{r}) E_j(z, \theta_K) E_k(z) e^{i\mathbf{G}\cdot\boldsymbol{\rho}} \right|^2 \tag{10.23}$$

Let us assume now a shallow grating at $z \approx 0$ that has a varying depth $b(\boldsymbol{\rho}) \ll D$ in a unit cell. (10.23) becomes:

$$\alpha_{\mathbf{G}} = \frac{(\epsilon_2 - \epsilon_3)k_2^2 k_0^2 |B(\mathbf{G})|^2}{4ka^4 \sin^2\phi} \cos^2(\phi_K - \phi_k)\nu_j(\theta_K) \tag{10.24}$$

Here we defined a dimensionless form factor as

$$\nu_j(\theta) = |E_j(0,\theta)|^2 / DK_j \tag{10.25}$$

and the 2D Fourier transform of the grating depth

$$B(\mathbf{G}) = \int d\boldsymbol{\rho}\, b(\boldsymbol{\rho}) e^{i\mathbf{G}\cdot\boldsymbol{\rho}} \tag{10.26}$$

For the case of a constant depth b circular holes of radius r, B can be given in terms of a Bessel function:

$$B(\mathbf{G}) = 2\pi r b J_1(rG)/G \tag{10.27}$$

We can also easily calculate the output coupling coefficient for a 1D grating, with lattice vectors $\mathbf{R} = na\hat{x}$, $(0 \le n < N)$, $\phi_0 = \pi/2$, and a guided mode with $\mathbf{k} = k\hat{x}$. The phase matching condition yields $\phi = \phi_K = \phi_k = 0$. $\Delta\epsilon$ does not depend on y, so the y-integral in (10.23) just gives a. We obtain

$$\alpha_{\mathbf{G}} = \frac{k_0^2}{512\pi^2 a^2} \left| \int dx\, dz\, \delta\epsilon(x,z) E_{r1}(z,\theta_K) E_k(z) e^{iGx} \right|^2 \tag{10.28}$$

If we further assume a shallow grating with depth $b(x) \ll D$ at $z \approx 0$, then we obtain (10.24) with

$$B(\mathbf{G}) = a \int dx\, b(x) e^{iGx} \tag{10.29}$$

This reduces to the known result for sinusoidal deformation obtained by coupled-mode theory. [66] For a square grating of constant depth b and tooth width w

$$B(\mathbf{G}) = ab \sin(Gw/2)/G \tag{10.30}$$

Next we evaluate the form factors (10.25) for radiation diffracted by a reciprocal lattice vector **G**. From (10.19), the field scattered into region j is at angle

$$\theta_j = \arcsin \frac{|\mathbf{k} - \mathbf{G}|}{n_j k_0} \tag{10.31}$$

so the propagation constants K_j are the same for radiation into regions 1 and 3. Since $n_1 < n_3$, it is possible that the angle is such that radiation modes are evanescent in region 1. In this case K_1 is imaginary, and there can be radiation only into region 3. We get

$$\nu_3(\theta) = \frac{4K_3}{K_2^2 D}\left[1 + \left(\frac{K_3}{K_2}\,\frac{K_2 + (K_1/i)\tan K_2 d}{(K_1/i) - K_2 \tan K_2 d}\right)^2\right]^{-1} \tag{10.32}$$

However, if the angle is such that all K_i are real, radiation is emitted into both half-spaces. This yields for radiation into region 3:

$$\nu_3(\theta_3) = \frac{4K_3(K_2^2 \cos^2 K_2 d + K_1^2 \sin^2 K_2 d)D^{-1}}{K_2^2(K_1 + K_3)^2 \cos^2 K_2 d + (K_1 K_3 + K_2^2)^2 \sin^2 K_2 d} \tag{10.33}$$

and into region $n = 1$:

$$\nu_1(\theta_1) = \frac{4K_1 K_2^2 D^{-1}}{K_2^2(K_1 + K_3)^2 \cos^2 K_2 d + (K_1 K_3 + K_2^2)^2 \sin^2 K_2 d} \tag{10.34}$$

10.4 In-plane coupling

In this section we calculate in our formalism the field that is scattered inside the waveguide by the grating due to an incident guided mode with wavevector $\mathbf{k}'$. This yields the in-plane coupling constant between two guided modes. We use (10.2) with the guided mode E-field, and (10.3) with (10.13), but without expanding $\bar{\rho}$. We get, with $\cos\gamma \equiv \hat{\mathbf{k}} \cdot \hat{\mathbf{k}}'$,

$$\mathbf{E}_s(\mathbf{r}) = \sum_k \frac{ck_0}{16\pi P_g} E_k(z)(\hat{\boldsymbol{\rho}} \times \hat{\mathbf{z}}) \cos\gamma \sqrt{\frac{ik}{2\pi\rho}} \int d\mathbf{r}' \Delta\epsilon(\mathbf{r}') E_{k'}(z') E_k(z') e^{ik\bar{\rho}} \tag{10.35}$$

Let us calculate the far-field amplitude in a direction $\hat{\mathbf{k}}$, at $\mathbf{r} = \rho\hat{\mathbf{k}} + z\hat{\mathbf{z}}$. Expanding $\bar{\rho} \approx \rho - \hat{\mathbf{k}} \cdot \boldsymbol{\rho}' + |\hat{\mathbf{k}} \times \boldsymbol{\rho}'|^2/2\rho$,

$$\mathbf{E}_s(\mathbf{r}) = \sum_k \frac{ck_0}{16\pi P_g} E_k(z) e^{ik\rho}(\hat{\boldsymbol{\rho}} \times \hat{\mathbf{z}}) \cos\gamma \int dx' dz' E_k(z') E_{k'}(z') e^{i(k'\cos\gamma - k)x'} \sqrt{\frac{ik}{2\pi\rho}} \cdot \int dy' e^{iky'^2/2\rho} e^{ik'\sin\gamma y'} \Delta\epsilon(\mathbf{r}') \quad (10.36)$$

where the integration variables x' and y' are respectively along $\hat{\mathbf{k}}$ and $\hat{\mathbf{z}} \times \hat{\mathbf{k}}$. The y' integral consists of factors of which the last two are periodic in y. Since the first factor is varying much slower than the periodicity of the other parts of the integrand, we can write approximately

$$\sqrt{\frac{ik}{2\pi\rho}} \int dy' e^{iky'^2/2\rho} e^{ik'\sin\gamma y'} \Delta\epsilon(\mathbf{r}') = \int dy' e^{ik'\sin\gamma y'} \Delta\epsilon(\mathbf{r}') \quad (10.37)$$

This yields a scattered field inside the guide as a sum over guided mode fields:

$$\mathbf{E}_s(\mathbf{r}) = \sum_\kappa \kappa(\mathbf{k}, \mathbf{k}') E_k(z) e^{ik\rho}(\hat{\boldsymbol{\rho}} \times \hat{\mathbf{z}}) \quad (10.38)$$

where the amplitude coupling strength to waves with wavevectors $\mathbf{k}$ is given by

$$\kappa(\mathbf{k}, \mathbf{k}') = \frac{ck_0}{16\pi P_g}(\hat{\mathbf{k}} \cdot \hat{\mathbf{k}}') \int d\mathbf{r}\, E_k(z) E_{k'}(z) \Delta\epsilon(\mathbf{r}) e^{i(\mathbf{k}'-\mathbf{k})\cdot\boldsymbol{\rho}} \quad (10.39)$$

This is consistent with the less general formula given for the 1D DFB laser calculated by coupled-mode theory [37].

10.5 Summary

In this chapter, we showed that applying the volume curent method to two-dimensionally periodic photonic crystal slabs yields the radiation and in-plane coupling constants for guided modes in a transparent way. We found the far-field from of the TE Green's function for a uniform slab and applied perturbation theory to arrive at the results.

10.6 Appendix

In this section, we describe a method to calculate the Green's function for an arbitrary photonic crystal slab. The knowledge of the Green's function can be useful, for example, for the calculation of transmission through a slab photonic crystal. Again we consider the two-dimensional periodicity as a perturbation to a uniform slab, except this time the perturbation may be arbitrarily large. Let the uniform slab be defined by an dielectric constant $\epsilon_0(\mathbf{r})$. At a frequency $\omega = ck_0$, Maxwell's equations with a source $\mathbf{J}(\mathbf{r})$ can be written for the electric field as

$$\nabla \times (\nabla \times \mathbf{E}(\mathbf{r})) - k_0^2 \epsilon_0(\mathbf{r})\mathbf{E}(\mathbf{r}) = 4\pi i \frac{k_0}{c}\mathbf{J}(\mathbf{r}) \tag{10.40}$$

The field can be expressed in terms of the dyadic Green's function $\bar{G}^0$ of the unperturbed dielectric slab:

$$\mathbf{E}(\mathbf{r}) = \frac{ik_0}{c}\int d\mathbf{r}'\bar{G}^0(\mathbf{r},\mathbf{r}')\mathbf{J}(\mathbf{r}') \tag{10.41}$$

Now let us introduce a perturbation $\epsilon(\mathbf{r})$ to the slab. Replacing ϵ_0 by $\epsilon_0 + \epsilon$ in (10.40), the electric field is found in terms of the Green's function $\bar{G}(\mathbf{r},\mathbf{r}')$:

$$\mathbf{E}(\mathbf{r}) = \frac{ik_0}{c}\int d\mathbf{r}'\bar{G}(\mathbf{r},\mathbf{r}')\mathbf{J}(\mathbf{r}') \tag{10.42}$$

Writing the equation in the following form,

$$\nabla \times (\nabla \times \mathbf{E}(\mathbf{r})) - k_0^2\epsilon(\mathbf{r})\mathbf{E}(\mathbf{r}) = 4\pi i \frac{k_0}{c}\left[\mathbf{J}(\mathbf{r}) - \frac{ick_0}{4\pi}\mathbf{E}(\mathbf{r})\right] \tag{10.43}$$

we can also use $\bar{G}^0$ to express the field as in equation (10.41). Substituting (10.42) into the resulting equation and using the fact that the equation must hold for arbitrary $\mathbf{J}$, we obtain the analogue of the Dyson equation in condensed matter theory for the Green's function of the photonic crystal:

$$\bar{G}(\mathbf{r},\mathbf{r}') = \bar{G}^0(\mathbf{r},\mathbf{r}') + \frac{k_0^2}{4\pi}\int d\mathbf{r}''\bar{G}^0(\mathbf{r},\mathbf{r}'')\Delta\epsilon(\mathbf{r}')\bar{G}(\mathbf{r}'',\mathbf{r}') \tag{10.44}$$

Equation (10.1) is the first-order approximation to this equation.

From the form of the equation (10.44) it is clear that we need to solve an integral equation for $\bar{G}(\mathbf{r},\mathbf{r}')$ only if $\mathbf{r}$ in the region of the perturbation. Otherwise, once $\bar{G}$ is known for those values, (10.44) yields the Green's function easily for any $\mathbf{r}$. However, $\bar{G}^0$ is non-uniformly divergent around $\mathbf{r}=\mathbf{r}'$, and furthermore it has a delta function sigularity. To avoid possible difficulties in evaluating the integral in (10.44) like the dependence of the pricipal value of the integral on the exclusion volume used [68, 69], we take a different route to solving (10.44). We decompose the Green's function into its Fourier components and write up a system of equations for the components.

First we take the Fourier transform of equation (10.44). Since $\bar{G}^0$ is translationally invariant for in-plane translation, it can be written in terms of its transform as

$$\bar{G}^0(\mathbf{r},\mathbf{r}') = \int d\mathbf{k}\; e^{i\mathbf{k}\cdot(\boldsymbol{\rho}-\boldsymbol{\rho}')}\bar{G}^0(\mathbf{k},z,z') \tag{10.45}$$

and since $\bar{G}$ must be periodic in the plane,

$$\bar{G}(\mathbf{r},\mathbf{r}') = \sum_{\mathbf{G}}\int d\mathbf{k}\; e^{i(\mathbf{G}+\mathbf{k})\cdot\boldsymbol{\rho}}e^{-i\mathbf{k}\cdot\boldsymbol{\rho}'}\bar{G}_{\mathbf{G}}(\mathbf{k},z,z') \tag{10.46}$$

Finally, the perturbation can be expressed as

$$\epsilon(\mathbf{r}) = \sum_{\mathbf{G}}\epsilon_{\mathbf{G}}(z)e^{i\mathbf{G}\cdot\boldsymbol{\rho}} \tag{10.47}$$

If we operate on (10.44) with $\frac{1}{2\pi V}\int_C d\boldsymbol{\rho}\int d\boldsymbol{\rho}' e^{-i(\mathbf{G}+\mathbf{k})\cdot\boldsymbol{\rho}}e^{i\mathbf{k}\cdot\boldsymbol{\rho}'}$, where C is the unit cell of the photonic crystal and V is the volume of C, we obtain the master equation:

$$\bar{G}_{\mathbf{G}}(\mathbf{k},z,z') = \delta_{\mathbf{G}0}\,\bar{G}^0(\mathbf{k},z,z') + \frac{k_0^2}{2}\sum_{\mathbf{G}'}\int dz''\;\bar{G}^0(\mathbf{k}+\mathbf{G},z,z'')\,\epsilon_{\mathbf{G}-\mathbf{G}'}(z'')\,\bar{G}_{\mathbf{G}'}(\mathbf{k},z'',z') \tag{10.48}$$

As in the case of equation (10.44), once we find $\bar{G}(z,z')$ for z in the region of the perturbation, then the Green's function is easy to obtain for any z. As we shall see, the transform of $\bar{G}^0$ is no longer divergent, it only has a jump discontinuity at $z=z'$, so convergency the problems of equation (10.44) are circumvented. In the following

we assume that the perturbation is non-zero only in region 2. For $\mathbf{r} \in$ region μ and $\mathbf{r}' \in$ region ν, the Green's function for the perfect slab is a spectral integral [67]

$$\bar{G}^0_{\mu\nu}(\mathbf{r},\mathbf{r}') = \frac{i}{2\pi}\int \frac{d\mathbf{k}}{k_\nu}\left[\bar{D}^e(\mathbf{k})F^e(z,z') + \bar{D}^m(\mathbf{k})F^m_{\mu\nu}(z,z')\right] e^{i\mathbf{k}\cdot(\rho-\rho')} - \frac{4\pi}{\epsilon_\nu k_0^2}\delta(\mathbf{r}-\mathbf{r}')\,\hat{\mathbf{z}}\hat{\mathbf{z}} \tag{10.49}$$

In this equation, $k_j = \sqrt{\epsilon_j k_0^2 - k^2}$, $\bar{D}^e(\mathbf{k}) = (\nabla \times \hat{\mathbf{z}})(\nabla' \times \hat{\mathbf{z}})$, and $\bar{D}^m(\mathbf{k}) = (\nabla \times \nabla \times \hat{\mathbf{z}})(\nabla' \times \nabla' \times \hat{\mathbf{z}})/\epsilon_\mu k_0^2$. Thus the Fourier transform of the Green's function has the form

$$\bar{G}^0_{\mu\nu}(\mathbf{k},z,z') = \frac{i}{2\pi k_\nu}\left[\bar{D}^e_0(\mathbf{k})F^e(z,z') + \bar{D}^m_0(\mathbf{k})F^m(z,z')\right] - \frac{2}{\epsilon_\nu k_0^2}\,\hat{\mathbf{z}}\hat{\mathbf{z}} \tag{10.50}$$

where the $\bar{D}_0$ are constant dyads. Let $z \in$ region 2 and $z' \in$ region 1. Then

$$F_{22}(z,z') = M_2(e^{ik_2 z_>} + R_{21}e^{-ik_2(z_>-2d)})(e^{-ik_2 z_<} + R_{12}e^{-ik_2 z_<}) \tag{10.51}$$

where $M_2 = (1 - R_{21}R_{23}e^{2ik_2 d})^{-1}$, the $R_{\mu\nu}$ are reflection coefficients for TE/TM polarized waves for propagation from region ν into region μ, and finally $z_>$ and $z_<$ are respectively the larger and smaller of z and z'. Knowing the expression for $\bar{G}^0$, we can solve (10.48) for $\bar{G}$. Since we assumed that the perturbation is only in region 2, the integral in (10.48) covers only a small interval in z. Therefore the equation is well suited to be solved by quadrature methods.

Chapter 11

Conclusion

We have investigated novel photonic crystal devices that can be used as building blocks of all-optical circuits. Examples were presented in which we contrast the behavior of light in photonic crystal waveguides and in traditional waveguides. We showed that bends in photonic crystals can transmit light without radiation losses and with 100% efficiency for certain designs. Bound states in photonic crystal waveguides can exist in constrictions and above the cutoff frequency, in mode gaps.

We dealt with the reflections encountered when photonic crystal waveguides are terminated. In an experimental setup, light can be efficiently coupled into and out of a photonic crystal waveguides using a tapered dielectric waveguide. In a numerical simulation, spurious reflections from cell edges can be eliminated by terminating the waveguide with a Bragg reflector waveguide.

We demonstrated novel lasing action in two-dimensional photonic crystal slabs with gain media. Lasing occurs in a bulk two-dimensional crystal at saddle points, where spontaneous emission is enahanced, in contrast to one-dimensional photonic crystals, where lasing is at band maxima and minima. We also designed a photonic crystal slab with an organic gain medium that can support a high-Q defect mode, predicting in low threshold lasing.

Two-dimensional photonic crystal slabs can also be used as free-space couplers. Their coupling properties are more advantageous than their one-dimensional counterparts. We drafted methods to calculate the coupling constant both numerically and

analytically, using a finite-difference time-domain method and the volume current method with a Green's function approach, respectively.

Bibliography

[1] E. Yablonovitch, Phys. Rev. Lett. **58**, 2059 (1987).

[2] S. John, Phys. Rev. Lett. **58**, 2486 (1987).

[3] J. D. Joannopoulos, R. D. Meade, and J. N. Winn, *Photonic Crystals*, Princeton, New York (1995).

[4] E. A. J. Marcatili, The Bell Systems Tech. J. **48**, 2103 (1969).

[5] R. D. Meade, A. Devenyi, J. D. Joannopoulos, O. L. Alerhand, D. A. Smith, and K. Kash, J. Appl. Phys. **75**, 4753 (1994).

[6] J. C. Chen and K. Li, Microwave Opt. Tech. Lett. **10**, 319 (1995).

[7] R. D. Meade, A. M. Rappe, K. D. Brommer, and J. D. Joannopoulos, Phys. Rev. B **48**, 8434 (1993).

[8] J. Goldstone and R. L. Jaffe, Phys. Rev. B **45**, 100 (1992).

[9] K. Lin and R. L. Jaffe, Phys. Rev. B **54**, 5750 (1996).

[10] J.P. Carini, J.T. Londergan, K. Mullen, D.P. Murdock, Phys. Rev. B **46** 15538 (1992).

[11] J.P. Carini, J.T. Londergan, K. Mullen, D.P. Murdock, Phys Rev. B **48** 4503 (1993).

[12] J.P. Carini *et al.*, Phys Rev. B **55** 9842 (1997).

[13] Y.A. Klimenko, L.I. Malsheyeva, A.I. Onipko, Journ. Phys.: Cond. Mat. **5**, 5215 (1993).

[14] O.O. Vakhnenko, Phys. Rev. B **52** 17386 (1995).

[15] H. Wu, D.W.L. Sprung and J. Martorell, J. Appl. Phys. **72**, 151 (1992).

[16] J.D. Joannopoulos, P.R. Villeneuve and S. Fan, Nature **386**, 143 (1997).

[17] S. Fan, P.R. Villeneuve, J.D. Joannopoulos and E.F. Schubert, Phys. Rev. Lett. **78**, 3294 (1997).

[18] S. Fan, P.R. Villeneuve, J.D. Joannopoulos and H.A. Haus, Phys. Rev. Lett. **80**, 960 (1998).

[19] A. Mekis *et al.*, Phys. Rev. Lett. **77**, 3787 (1996).

[20] J. Berenger, J. of Comp. Phys. **114**, 185 (1994).

[21] P.R. Villeneuve, S. Fan and J.D. Joannopoulos, Phys. Rev. B, **54**, 7837 (1996).

[22] B. Temelkuran, E. Ozbay, Appl. Phys. Lett., **74**, 486 (1999).

[23] T. Baba, N. Fukaya, J. Yonekura, Elec. Lett., **35**, 654, (1999).

[24] Shawn-Yu Lin, E. Chow, V. Hietala, P.R. Villeneuve, J.D. Joannopoulos, Science, **282**, 274-6 (1998).

[25] K.S. Kunz and R.J. Luebbers, *The finite difference time domain method for electromagnetics*, CRC Press, Boca Raton, (1993).

[26] A. Mekis, S. Fan, J. D. Joannopoulos, Phys. rev. B, **58**, 4809 (1998).

[27] H. Kogelnik, C.V. Shank, Appl. Phys. Lett. **18**, 152 (1971).

[28] I. P. Kaminov, H. P. Weber, and E. A. Chandross, Appl. Phys. Lett. **18**, 497 (1971).

[29] S.-X. Qian, J. B. Snow, H. M. Tzeng, and R. K. Chang, Science 231, 486 (1986).

[30] M. Kuwata-Gonokami, R. H. Jordan, A. Dodabalapur, H. E. Katz, M. Schilling, R.E. Slusher, and S. Ozawa, Opt. Lett. **20**, 2093 (1995).

[31] F. De Martini, G. Innocenti, G. R. Jacobovitz, and P. Mataloni, Phys. Rev. Lett. **59**, 2955 (1987).

[32] M. Berggren, A. Dodabalapur, R. E. Slusher, Z. Bao, A. Timko, and O. Nalamasu, Elec. Lett. **34**, 90 (1998).

[33] M. Berggren, A. Dodabalapur, R. E. Slusher, and Z. Bao, Nature (London) **389**, 466 (1997).

[34] A. Dodabalapur, M. Berggren, R. E. Slusher, Z. Bao, A. Timko, P. Sciortino, E. Laskowski, H. E. Katz, and O. Nalamasu, IEEE J. Sel. Top. Quan. El. **4**, 67 (1998).

[35] P. Yeh, *Optical Waves in Layered Media*, Wiley, New York (1988).

[36] F.K. Kneubühl: *Theories on Distributed Feedback Lasers*, Langhorne, Harwood Academic Publishers (1993).

[37] H. Ghafouri-Shiraz, B.S.K. Lo: *Distributed Feedback Laser Diodes*, New York, Wiley (1996).

[38] M. Meier, A. Mekis, A. Dodabalapur, A. Timko, R.E. Slusher, J.D. Joannopoulos, O. Nalamasu: Appl. Phys. Lett. **74,** 7 (1999).

[39] K. Inoue, M. Sasada, J. Kawamata, K. Sakoda, J.W. Haus: Jpn. J. Appl. Phys. **38** L157 (1999).

[40] H.A. Haus: *Waves and Fields in Optoelectronics*, Engelwood Cliffs, NJ, Prentice-Hall (1984).

[41] H. Yokoyama, K. Ujihara: *Spontaneous Emission and Laser Oscillation in Microcavities*, Boca Raton, CRC Press (1995).

[42] P.R. Villeneuve, S. Fan, S.G. Johnson, and J.D. Joannopoulos, IEE Proc. Optoel. **145** (1998).

[43] M. Berggren, A. Dodabalapur and R.E. Slusher, Appl. Phys. Lett. **71,** 2230 (1997).

[44] E. Yablonovitch, T. J. Gmitter, Phys. Rev. Lett. **63,** 1950 (1989).

[45] S. John, J. Wang, Phys. Rev. B, **43,** 12772 (1991).

[46] H. Yokoyama, S. D. Brorson, Jour. Appl. Phys. **66,** 4801 (1989).

[47] J. G. Fleming, S. Lin, Opt. Lett. **24,** 49 (1999).

[48] S. Fan, P. R. Villeneuve, J. D. Joannopoulos, Jour. Appl. Phys. **78,** 1415 (1995).

[49] P.R. Villeneuve, S. Fan, J. D. Joannopoulos, K. Y. Lim, G. S. Petrich, L. A. Kolodziejski, R. Reif, Appl. Phys. Lett. **67,** 167 (1995).

[50] S. G. Johnon, S. Fan P. R. Villeneuve, J. D. Joannopoulos, Phys. Rev. B **60,** 5751 (1999).

[51] A. Katzir, A. C. Livanos, and A. Yariv, Appl. Phys. Lett. **30,** 225 (1977).

[52] E. G. Loewen and E. Popov, *Diffraction gratings and applications*, M. Dekker, New York (1997).

[53] D. Heitmann and R.V. Pole, Appl. Phys Lett. **37,** 585 (1980).

[54] P-P. Borsboom and H.J. Frankena, J. Opt. Soc. Am. A **12,** 1142 (1995).

[55] G. Hatakoshi, H. Fujima and K. Goto, Appl. Opt. **23,** 1749 (1984).

[56] M. Meier *et. al*, J. Appl. Phys. **86,** 3502 (1999).

[57] H. Kogelnik, *Theory of Optical Waveguides*, in T.Tamir, *Guided-Wave Optoelectronics*, Springer-Verlag, Berlin (1988).

[58] G. Mur, IEEE Trans. Electromag. Comput. **EMC-23,** 377 (1981).

[59] A. W. Snyder, IEEE Trans. Micr. Theo. **MTT-18**, 608 (1970).

[60] I. A. White, IEE Jour. Microw. **3**, 186 (1979).

[61] P. C. Kendall, P. N. Robson, J. E. Sitch, IEE Proc. Jour. Optoelec. **132**, 140 (1985).

[62] R. H. Jordan, D. G. Hall, Appl. Phys. Lett. **64**, 3077 (1994).

[63] B. E. Little, S. T. Chu, Opt. Lett. **21**, 1390, (1996).

[64] C. Olson, D. G. Hall, IEEE Jour. Quan. Elec. **34**, 2298, (1998).

[65] D. Marcuse, *Report on radiation emitted by a 2D refractive index grid*, unpublished (1999).

[66] D. Marcuse, *Theory of Dielectric Optical Waveguides*, Academic Press, Inc., San Diego (1974).

[67] W. C. Chew, *Waves and fields in inhomogeneous media*, IEEE Press, New York (1990).

[68] A. D. Yaghian, Proc. IEEE **68**, 248 (1980).

[69] W. C. Chew, IEEE Trans. Ant. Prop. **37**, 1322 (1989).

THESIS PROCESSING SLIP

FIXED FIELD: ill. _____ name _____

index _____ biblio _____

▶ COPIES: (Archives) Aero Dewey Eng Hum

Lindgren Music Rotch (Science)

TITLE VARIES: ▶ ☑ for degree BOOK

NAME VARIES: ▶ ☐ _____

IMPRINT: (COPYRIGHT) _____

▶ COLLATION: 143 P

▶ ADD: DEGREE: _____ ▶ DEPT.: _____

SUPERVISORS: _____

NOTES:

cat'r: date:

page: F64

▶ DEPT: Phy

▶ YEAR: 2000 ▶ DEGREE: Ph. D.

▶ NAME: MERIS, Hila